Characterization, Modelling, and Manufacturing of Morphing Shape Memory Alloy Hybrid Composites

Sanesh Iyer, Department of Mechanical Engineering, Faculty of Engineering

McGill University, Montreal

December 3, 2019

A thesis submitted to McGill University in partial fulfillment of the requirements of the degree of Master in Engineering (Thesis)

Table of Contents

List of Figures

List of Tables

List of Symbols & Acronyms

‘	Denotes ply local coordinate system
$\{\}^{C}$	Denotes compressed layup notation
$\{\}_{S}$	Denotes symmetric laminate notation
$\{\}_{T}$	Denotes Total Layup notation
a	First two cycles hysteresis energy difference ($\Delta HE_{2,1}$)
A	Area
A_e	Surface area of shell element
A_f	Austenite finish temperature
A_P	Austenite peak temperature
A_S	Austenite start temperature
AW	Area weighted
A_x	Cross sectional area
b	Functional Stabilization decay constant
C	Width of arc between end points
CBD	Calorimétrie/calorimètre à balayage différentiel
d	Depth of arc from peak to end point along radial direction
d_0	Initial diameter
DoF	Degrees of Freedom
DSC	Differential Scanning Calorimeter/Calorimetry
$\left(\frac{\delta\sigma}{\delta T}\right)_L$	Linear dependency of beginning of and end of transformation stresses upon loading
$\left(\frac{\delta\sigma}{\delta T}\right)_U$	Temperature dependency of unloading transformation stresses upon unloading
E	Young's Modulus
e	Element counting index
E_A	Young's Modulus of austenite
ECLT	Extended Classical Laminate Theory
EDM	Electrical discharge machining

E_M	Young's Modulus of martensite
E_{Mat}	Matrix stiffness
Subscript or superscript Exp	Denoting experimentally measured value[s]
F_{Snap}	Snap through force
G	Shear Modulus
K	Timoshenko Beam shear stiffness
k	Timoshenko Beam shear factor
K_{11}	Longitudinal structural stiffness
K_{22}	Transverse structural stiffness
K_{Mat}	Material stiffness matrix
L	Length
L_{Asm}	Assembly length
LCM	Liquid composite molding
L_{Elem}	Element length
L_0	Initial length
L_{Pre}	Preload length
M_{Elem}	Minimum elements
M_f	Martensite finish temperature
M_P	Martensite peak temperature
M_S	Martensite start temperature
MVT	Mean Value Theorem
n	Cycle counting index
N	Total Number of Cycles
PTP	SMA Phase Transformation Percentage
R	Resistance or Radius (contextual)
R^2	Coefficient of Determination
R_{Elem}	Element Ratio
R_o	Matrix outer radius
R_{SMA}	SMA outer radius
S_{Beam}	Beam element seed size

SHHC	Prestrained high temperature hybrid composite
SLHC	Prestrained low temperature hybrid composite
SMA (AMF)	Shape Memory Alloy (Alliages à mémoire de forme)
SMAHC (CHAMF)	Shape Memory Alloy Hybrid Composite (composites hybrides AMF)
SME	Shape Memory Effect
S_{Shell}	Shell Element Seed Size
Subscript and Superscript E	End of phase transformation on superelastic curve
Subscript and Superscript S	Start of phase transformation on the superelastic curve
Subscript L	On the superelastic loading curve
Subscript or Superscript Y	Denoting Yield point
Subscript U	On the superelastic unloading curve
Superscript or subscript A	Property belonging to the austenite phase
Superscript or subscript M	Property belonging to the martensite phase
Superscript Raw	Property belonging to un-stabilized SMA samples
Superscript Stab.	Property belonging to functionally stabilized SMA wire
S_x	Standard Deviation
T	Temperature (general) or Tensile Force (in **Section 3.2.4.1**)
t	Thickness
$T_{Bifurcation}$	The temperature at which bifurcation is observed
T_{Gel}	Gelation temperature of composite
T_{Glass}	Glass transition temperature
T_{Heat}	Temperature to which SMA is heated for actuation
T_0	Reference temperature for superelastic properties
T_{Proc}	Temperature at which stabilization process occurs
$T_{Relative}$	Temperature relative to room temperature
TRIP	Transformation induced plasticity
T_{Room}	Room temperature
UHC	Unstrained hybrid composite
v	Poisson's Ratio

υ_A	Poisson's Ratio of austenite
υ_{Mat}	Matrix Poisson's Ratio
υ_{SMA}	SMA Poisson's Ratio
α	Coefficient of Thermal Expansion
$\Delta HE_{n,n-1}$	Hysteresis energy difference between cycles
ε	Strain
ε_L	The projected zero stress elastic strain of martensite
ε_{Load}^{End}	End of loading transformation strain
ε_{Pre}	Prestrain value
ε_Y^M	Yield strain of martensite when T > A_f
κ	Curvature
κ^{AC}	As cured curvature
κ^{AW}	Area weighted curvature
ρ	Resistivity
σ	Stress
$\sigma_{11}^{Actuation}$, $\sigma_{11}^{Act.}$, & σ_{Act}	Actuation stress in the direction of the SMA wire
σ_{Int}	Interfacial Stress
σ_{tL}^E	Stress at which phase transformation ends upon loading
σ_{tU}^E	Stress at which phase transformation ends upon unloading
$\sigma_{tU}^E(T)$	Unloading transformation end stress as temperature function
$\sigma_{tU}^E\|T_0$	Unloading transformation end stress at reference temperature
$\sigma_{11}^{External\ Load}$ & $\sigma_{11}^{Ext.}$	Stresses induced by external load along longitudinal direction
$\sigma_{11}^{Net\ Actuation}$ & $\sigma_{11}^{Net\ Act.}$	Net actuation stress in the longitudinal direction
σ_{Pre}	Prestress
$\sigma_{11}^{Processing}$	Residual processing stresses along longitudinal direction
σ_{cL}^S	Compressive stress at which phase transformation begins
σ_{tL}^S & $\sigma_{Start\ Loading}^{Transformation}$	Stress at which phase transformation begins upon loading
σ_{tU}^S	Stress at which phase transformation begins upon unloading
θ	Ply Angle

Abstract

Integrated morphing structures could significantly impact many industries, from aerospace to automotive racing. By combining multiple materials, it is possible to develop load-bearing primary structures whose shape can be directly controlled, eschewing the use of complex mechanical, hydraulic, or electrical actuator assemblies. The approach to morphing composites developed in this thesis combines shape memory alloys (SMAs) co-cured into carbon fibre reinforced epoxy laminates. SMAs provide the actuation and control capability while the composite laminate enables the structure to bear load. The goal of this thesis is to take a coupled approach to developing the characterization, modelling, and manufacturing of morphing SMA hybrid composites (SMAHCs). The first issue tackled in this thesis is the characterization of the thermomechanical behaviour of SMAs. A new characterization process is developed as an extension of existing standard tests to includes the effects of functional stabilization and thermal behaviours required for actuation applications. This process is used to characterize a NiTiCu SMA using differential scanning calorimetry (DSC) and tensile testing. Functional stabilization is shown to effect mechanical properties by as much as 70 [%], demonstrating the importance of characterizing this phenomenon. A novel device which enables the coupled thermo-electro-mechanical fatigue characterization of shape memory alloys is developed. The device is demonstrated to be able to capture the change in resistivity associated with SMA phase transformations as well as the plasticity effects of functional stabilization. A finite element model for SMAHCs is developed using ABAQUS and the experimentally measured SMA material properties. The SMAHC finite element model is used to execute a parametric study to investigate the effects of various design and manufacturing parameters. It is observed that SMAHCs can be actuated by more than 18 [%] change in curvature, a significant and useful amount when considering applications in aerostructures and tooling design. The parametric study demonstrates the sensitivity of SMAHCs to the design variables, and thus the imperativeness of having a clear understanding of the loads in end-use applications prior to design and implementation of SMAHC structures. Lastly, a cutting-edge apparatus for the manufacturing of SMAHCs compatible with industry standard autoclave and out-of-autoclave composites manufacturing techniques is developed and built. The SMAHC panels manufactured using this fixture are used to validate the electrical isolation scheme, enabling further experimental testing to be performed.

Sommaire

Les structures adaptatives intégrées pourraient avoir un impact significatif sur de nombreuses industries, de l'aérospatiale à l'automobile. En combinant plusieurs matériaux, il est possible de développer des structures primaires dont la forme peut être contrôlée directement, en évitant d'utiliser des ensembles complexes d'actionneurs mécaniques, hydrauliques ou électriques. L'approche pour développer des composites adaptatifs dans cette thèse combine des alliages à mémoire de forme (AMF) moulées dans des laminés époxy renforcés de fibres de carbone. Les AMF procurent la capacité d'actionnement et de contrôle alors que les laminés composites permettent à la structure de supporter les charges. L'objectif de cette thèse est d'adopter une approche couplée pour la caractérisation, la modélisation et la fabrication de composites hybrides AMF (CHAMF) adaptatifs utilisant des technologies modernes. Le premier problème abordé dans cette thèse est la caractérisation du comportement thermomécanique des AMF. Un nouveau processus de caractérisation, basé sur des tests standards, est développé afin de combiner les effets de la stabilisation fonctionnelle et des comportements thermiques requis pour les applications d'actionnement. Ce processus est utilisé pour caractériser un NiTiCu AMF par calorimétrie à balayage différentiel (CBD) et avec un test de traction. Il a été démontré que la stabilisation fonctionnelle affectait les propriétés mécaniques jusqu'à 70 [%], illustrant l'importance de la caractérisation de ce phénomène. Un nouveau dispositif permettant la caractérisation couplée thermo-électro-mécanique de la fatigue AMF est développé. Il a été démontré que le dispositif est capable de capturer le changement de résistivité associé aux transformations de phase SMA ainsi que les effets de la stabilisation fonctionnelle sur la plasticité. Un modèle d'éléments finis pour les CHAMF est développé à l'aide d'ABAQUS et des propriétés du matériau AMF mesurées expérimentalement. Le modèle d'éléments finis CHAMF est utilisé pour exécuter une étude paramétrique afin d'étudier les effets de divers paramètres de conception et de fabrication. Il est observé que les CHAMF peuvent être activés avec plus de 18 [%] de changement de courbure, une quantité significative et utile pour les applications dans les structures aérospatiales et la conception d'outillages. L'étude paramétrique démontre la sensibilité des CHAMF aux variables de conception, et donc la nécessité de bien comprendre leurs charges dans les applications d'utilisation finale avant la conception et mise en œuvre. Enfin, un appareil pour la fabrication de CHAMF et construit. Les panneaux SMAHC fabriqués à l'aide de cet outillage servent à valider le schéma d'isolation électrique, ce qui permet de réaliser d'autres tests expérimentaux.

Acknowledgements

First, I'd like to thank my Supervisor Prof. Pascal Hubert (McGill) for the opportunity to study at McGill and abroad. Your guidance and inspiration were central in my ability to thrive during my Masters. Prof. Véronique Michaud (EPFL) and Prof. Simon Joncas (ÉTS), your support and the collaboration of your groups proved invaluable for my learning and this research. Prof. Fiona Zhao (McGill), thank you for all the teaching opportunities you opened for me. They were personally fulfilling, and I learned an incredible amount from those experiences.

The McGill Structures and Composite Materials Laboratory is an incredible place to work. It's warm, welcoming, and collaborative. Everyone is willing to help and excited to learn. A special thank you to Adam Smith, Lucie Riffard, and Derek Harvey for your training and guidance. Julieta, Caroline, Linus, & Louis, your efforts in your Masters' theses were inspirational at the beginning of mine. Thank you to all the other SCML family members who've supported me academically and been my friends here. EPFL's Laboratory for Processing of Advanced Composites (LPAC) and Dr. Amaël Cohades welcomed me with equally open arms, for which I am extremely grateful.

Gratitude is also expressed to our funding partners at the Natural Sciences and Engineering Research Council of Canada (NSERC), the Research Center for High Performance Polymer and Composite Systems (CREPEC), and the Werner Graupe Chair for their financial support.

Personal support came from too many people to name; family and friends, old and new, in Vancouver and Montreal who celebrated the highs and helped me through the lows. It couldn't have been done without you all.

This thesis is dedicated to Bonnie (RIP).

Contributions of the Authors

Section 2

The thermo-electro-mechanical measurements in **Section 2.5** are taken using a fixture developed and calibrated by Baptiste Guyon in his Master en Science des Materiaux (EPFL) project. This project was co-supervised by Prof. Pascal Hubert, Prof. Veronique Michaud, and Sanesh Iyer.

Related Works

Additional projects which were executed in parallel to this thesis whose results are not used directly or indirectly in this thesis are:

- *Development of Processing Models for Shape Memory Alloy Hybrid Composites*
  Jonathan Lesage, B. Eng. (McGill), SURE 2018 (NSERC USRA funded)
  Supervisors: Sanesh Iyer, Prof. Pascal Hubert
- *Shape Memory Alloy Clamp*
  Charles Turner, B. Eng (McGill), MECH 498 Interdisciplinary Design 1 (Fall 2017)
  Supervisors: Sanesh Iyer, Prof. Pascal Hubert, Prof. Rosaire Mongrain

A series of projects co-supervised by Sanesh Iyer and Prof. Pascal Hubert to develop an apparatus to perform the batch stabilization of Shape Memory Alloys has included the following projects:

- *Spooled SMA Wire Processing Device*
  Philip Roberge, B. Eng (McGill), MECH 498 Interdisciplinary Design 1 (Fall 2018)
  Supervisors: Sanesh Iyer, Prof. Pascal Hubert, Prof. Tim Lee
- *Validation of SMA Wire Processing Device*
  Siddharth Raghavan, SURE 2019 (Rubin Gruber Award funded)
  Supervisors: Sanesh Iyer, Prof. Pascal Hubert
- At the time of submission, Siddharth Raghavan is undertaking a MECH 498 project to develop automate the SMA processing device. Alexandre Belisle is continuing work on this project to further develop the SMA processing device for his M. Eng. (Non-Thesis) project.

A special thank you to the students involved in these works for their hard work and the learning opportunity they provided to their supervisors.

Awards Related to Thesis Work

- 1st Prof. Hoa Student Paper Award 11th Canadian International Conference on Composites (CANCOM 2019)
- 1er CREPEC Concours d'affiches scientifiques 2019

Administrative Involvement

Workshop Safety Committee – Dept. of Mech. Eng. – Graduate Student Rep.
Eng. Committee on Teaching and Learning – Fac. of Eng. – Graduate Student Rep.
Council of Graduate and Postdoctoral Studies – Senate Subcommittee – Graduate Student Rep.

Teaching & Learning

The following is a list of activities related to teaching and learning that the author of this thesis engaged in addition to their research studies.

- *MECH 290 Design Graphics* Course Development Assistant (Prof. F. Zhou)
  Development of new teaching content for manual drafting, Solidworks CAD, DFM/A, and GD&T. A learning-outcomes approach was used to develop course teaching material for tutorial sessions. Training Teaching Assistants in the delivery and grading of this work.
- *MECH 290 Design Graphics* Teaching Assistant (Prof. F. Zhou, 2 Semesters)
  Instruct tutorial sessions for and grade assignments from students in MECH 290.
- *MECH 360 Principles of Manufacturing* Course Development Assistant (Prof. F. Zhou)
  Benchmarking of national and international manufacturing curriculums in B. Eng. (Mech.) and similar programs to inform new curriculum development at McGill.
- *MECH 321 Principles of Manufacturing* Teaching Assistant (Prof. P. Hubert)
  Develop and deliver tutorials for finite element modelling and analysis in ABAQUS. Assist students in semester project to optimize a bracket using FEA and experimentally validate their results.
- *Matlab for Engineers* Instructor (McGill Institute for Aerospace Engineering)
  Develop and instruct a tutorial series on coding and the use of Matlab for B. Eng. Students. The course included code development theory and the use of various Matlab tools.

1. Introduction to Morphing Hybrid Composites

Morphing hybrid composites is a relatively young sub-field of the much-larger field of fibre reinforced polymer composites (herein referred to as *composites*). An extensive state-of-the-art in composites is presented by the U.S. Department of Energy [1], which summarizes that the major advantages of composite materials are their high mechanical performance, corrosion resistance, and tailorability for each application [1]. Applications of composite materials range from aerospace [2], to automotive [3], to energy [4]. Many notable applications use composite structures, such as the Boeing 787 fuselage [5] and modern wind-turbine blades [6]. Despite their performance advantages, cost is a major suppressor of their widespread application and focus is being placed on driving down manufacturing times and cost [1], [7]. Rather than reduce cost, morphing hybrid composites adds value to structures by leveraging tailorability.

While traditional composites typically involve two-materials – a reinforcement and a matrix, – hybrid composites utilize three or more materials. Hybrid composites may involve blends of standard reinforcement such as carbon or glass fibres to reduce cost or tailor mechanical properties [8], [9]. In more exotic applications, hybrid composites can integrate materials such as shape memory alloys [10], piezoelectrics [11], and fibre-optics [12] to provide sensing actuation functions. These *smart composites* add value by integrating functions which would typically be controlled by other component assemblies (i.e. strain gauges, motors, etc.) directly into the structure. While potential cost and mass effects are not immediately clear, morphing hybrid composites could enable these functions to be built into structures into which traditional actuation assemblies would not fit. Take for example, Boeing's Variable Geometry Chevron [13] which integrates a shape memory alloy actuator into a jet engine chevron. The tight volume of this application prevents a traditional actuator (i.e. electric or hydraulic actuator) from being used here. Other applications where hybrid composites can enable morphing where traditional actuators cannot fit include helicopter rotor blades [14] or racing sailboat hydrofoils – which are the inspiration for this project [15].

The morphing technology explored in this thesis is, specifically, are composites comprised of nickel titanium based SMAs, carbon fibre reinforcements, and epoxy matrices. SMAs can be heated using the Joule effect to generate actuation forces and can also be used as sensors in a feedback loop [16]. SMAs have also been investigated for use in damage tolerant [17] and self-healing [18] hybrid composites. As opposed to other mono- or bi- functional hybrid composites, shape memory alloy hybrid composites (SMAHCs) could be *multi*-functional by integrating actuation, sensing, healing, and primary-load bearing abilities into a structure.

A known limit of SMA actuators is their loading rate, which is orders of magnitude slower than traditional systems [19]. A high actuation speed is possible with composite tailoring being used to create multistable laminates [20], [21]. Multistable laminates, however, are not self-actuating, and require external loads to shift between states. Shape memory alloys could be combined with composite tailoring to create self-actuating non-linear structures with higher rates than bare SMAs and greater control than multistable laminates. Aspirationally, this technology could one day be used to realize NASA's vision of an integrated morphing wing [22].

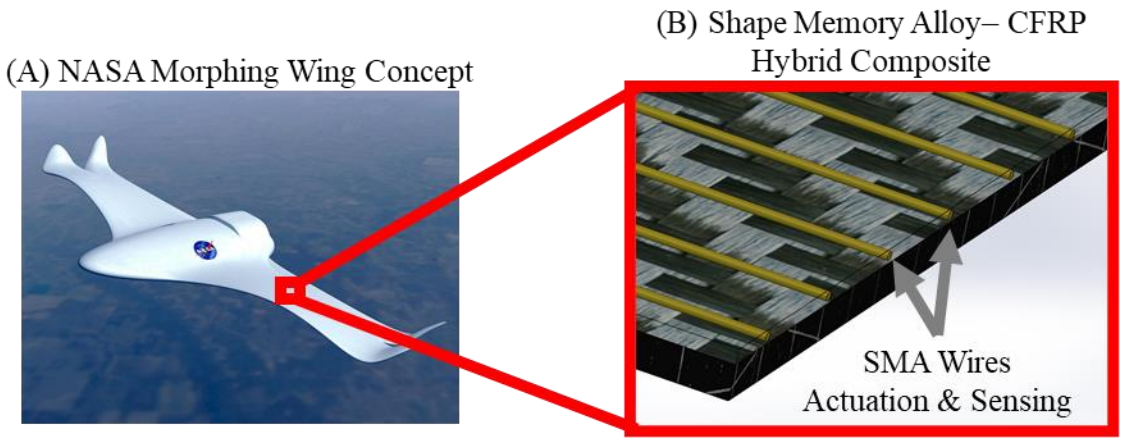

Figure 1.1 SMA Hybrid Composite (B) Used in NASA Morphing Wing Concept (A) NASA Morphing Wing available with open license [23] at [24]

1.2. Statement of Thesis Goal

Shape memory alloy hybrid composites, even ones which combine SMAs and multistable effects [25] have been previously studied to varying depths as is subsequently discussed in this work. Much of the work in this field occurred in the late 1990's to mid 2000's. Since that time, both computing and precision-manufacturing equipment have decreased in cost and increased in power by orders of magnitude. Armed with modern technology and 20 years of research, it's expected that several improvements can be made on this work in pursuit of maturing this technology. The goal of this thesis is to take a coupled approach to developing the characterization, modelling, and manufacturing of morphing SMAHCs using state-of-the-art technology and research. The research will be guided with an eye on improving the technology readiness level (TRL) of SMAHCs by focusing on the use of tools (physical and digital) which are widely commercially available.

1.3. Thesis Organization

This thesis is split into three sections which follows the process required to develop a morphing shape memory alloy hybrid composite. First, **Chapter 2. Shape Memory Alloys** focuses on SMAs, including their micro- and macro- mechanics, their modelling, the development and execution of a thermomechanical characterization process, and a brief electromechanical investigation. Following this is **Chapter 3. Finite Element Modelling of Hybrid Composites**, which includes the development of finite element model for SMAHCs. Lastly, a preliminary investigation into the manufacturing of SMAHCs is included in **Chapter 4. Preliminary Investigation into SMAHC Manufacturing.** A final summary and set of conclusions are made following these three sections. Given the disparate nature of these topics, backgrounds and reviews for each topic are presented in the relevant section for clarity.

2. Shape Memory Alloys

2.1. Introduction to Shape Memory Alloys

Shape memory alloys (*SMAs*) includes metals in a broader class of shape memory materials. A common SMA is Nitinol, which is an alloy composed of binary nickel and titanium and commonly used in medical applications such as heart stents [26], [27]. Due to it's established use in medical applications, many existing standards regarding SMAs focus on the chemistries and manufacturing of Nitinol SMAs for these uses (see [28], [29]). Ternary alloys of Nitinol exist, including NiTiCu, NiTiFe, and NiTiAl, which exhibit different mechanical behaviours. This discussion is limited to binary and ternary NiTi alloys. Included is a discussion of their unique micro-mechanical behaviour and the resulting macro-mechanical responses.

2.1.1. Phases and Crystal Structure

The underlying mechanism of shape memory alloy's macro-thermomechanical responses are solid-state, reversible, diffusion-less, phase changes which can be incited by either of mechanical loading (stress or strain) or thermal loading (heating). There are two main phases observed in nickel-titanium based shape memory alloys, *martensite* and *austenite*. The martensitic phase is stable at low temperature and stress, as well as at high temperature and high stress. The austenite phase is stable at high-temperature and low-stress as well as low-temperature and high stress. The phase transformation involves a monoclinic crystal structure change, as shown in Figure 2.1.

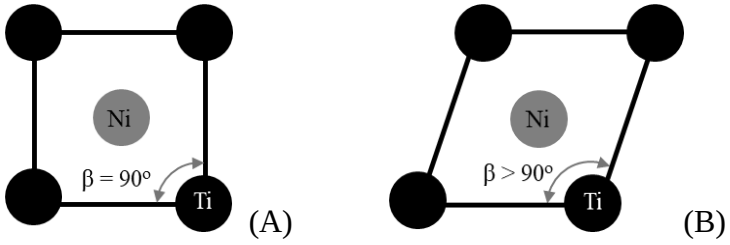

Figure 2.1 B2 Cubic Austenite (A) and B19' Monoclinic Martensite (B) Crystal Structures

Two other phases are possible, *R-Phase* for NiTiFe, NiTiAl, and aged or heat-treated NiTi alloys, as well as the B19 phase for NiTiCu alloys [30]. These phases are unstable and transitional, with their occurrence highly dependent on alloy chemistry and thermomechanical histories [31]. These phases are not discussed further in this thesis as they are not observed experimentally for the materials studied (see **Section 2.3**) and are not considered in existing numerical models (see **Section 2.1.5**).

The phase change is clearly observed when SMAs are studied using differential scanning calorimetry (DSC), where heat flow changes correspond to the transition temperatures, as shown in Figure 2.2. For austenite-martensite systems, two peaks which correspond with heating and cooling transformations are observed. The temperature above which unstressed austenite is stable, the *austenite finish temperature (A_f)* is measured on heating. On cooling, the temperature below which unstressed martensite is stable is measured as the *martensite finish temperature (M_f).* For both heating and cooling there are temperatures which correlate to the *start* (*A_s & M_s)* and energy *peak* (*A_p & M_p).* The most important temperatures in application are the finish temperatures, as these define the outer boundaries where phases are stable.

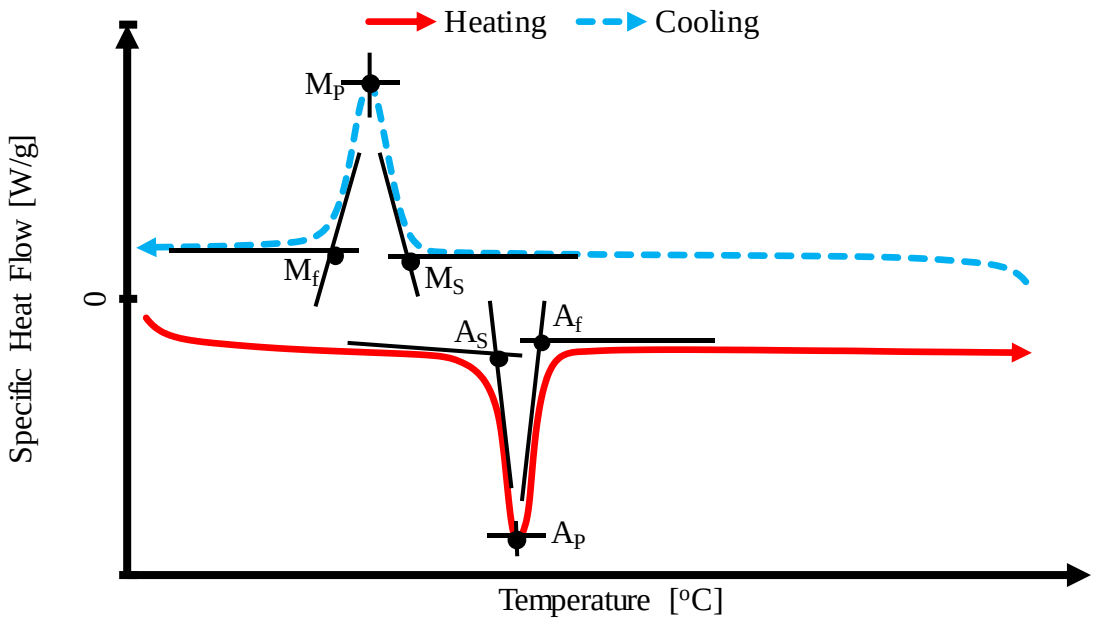

Figure 2.2 Example DSC Curve for Two-Phase Shape Memory Alloys

2.1.2. Mechanical Behaviours

The first mechanical behaviour of SMAs is their namesake, the *Shape Memory Effect* (*SME*), is shown in Figure 2.4. To exhibit this behaviour, SMAs are loaded and unloaded below their M_f. As it is stressed, the martensite is deformed from its *twinned* state to it's *detwinned* state (shown in Figure 2.3). Note that the loading curve in Figure 2.4 is like a plasticity curve, with a stiffening and return to linear elasticity at the end. On unloading, the material behaves linear elastically and exhibits a "*pseudo-plastic*" strain.

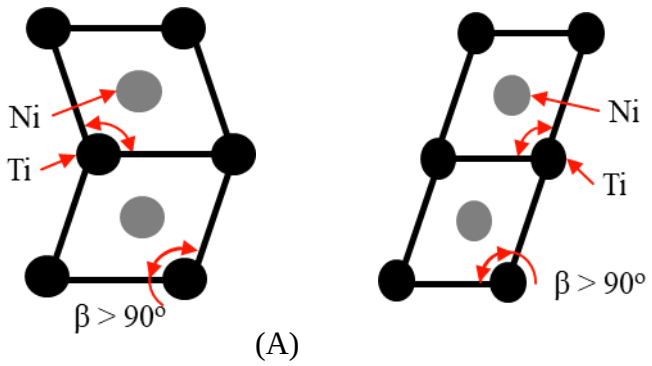

Figure 2.3 Twinned Martensite (A) and Detwinned Martensite (B)

When the strained and unloaded SMA is then heated above the A_f, one of three behaviours are observed. First is *unconstrained recovery* (also referred to as *free recovery*) where the SMA can deform freely and the "*pseudo-plastic*" strain is removed due to the martensite-to-austenite phase change. In this case, the initial shape is recovered (hence "shape memory effect") when heated. The second is *constrained recovery*, where strain is not allowed, the SMA will exert a stress as the martensite-to-austenite phase change is prevented. An *elastic recovery* case is also possible, where heating is performed on a wire which is supported by elastic supports and takes on the elastic behaviour of that material. These effects are useful in applications such as medical stents, where the stents are deformed to be quite small for insertion and then expand when placed and heated to body temperatures [32]. While the micro-mechanisms of the SME are well understood, the coupling of the thermal, elastic, and twinning phenomena create challenges for characterization and not commonly modelled in existing numerical software (see **Section 2.1.5)**. The SME is not useful for the proposed actuation application.

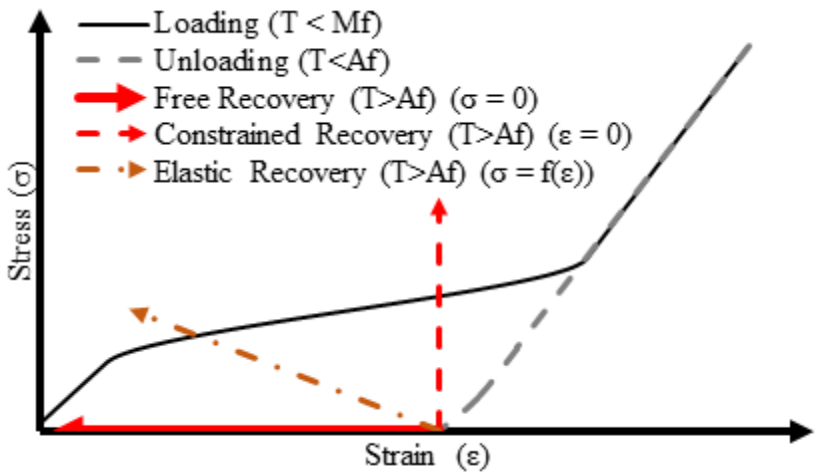

Figure 2.4 Shape Memory Effect

Superelasticity – the main mechanical behaviour of interest for actuation applications – is the hysteretic behaviour of SMAs when loaded and unloaded at temperatures above A_f, an example of which is shown in Figure 2.5. Only a martensite-austenite phase change occurs when loading and the reverse upon unloading in the superelastic regime, with no twinning effects. The mechanical property representation is discussed further in **Section 2.2**. For now, the main observation is that there are three discrete zones in the loading and unloading curves, the linear elastic, the low stiffness transformation plateau, and the second linear elastic. The useful region for actuation applications is within the transformation region, as this is where thermal excitation can be used to generate stresses.

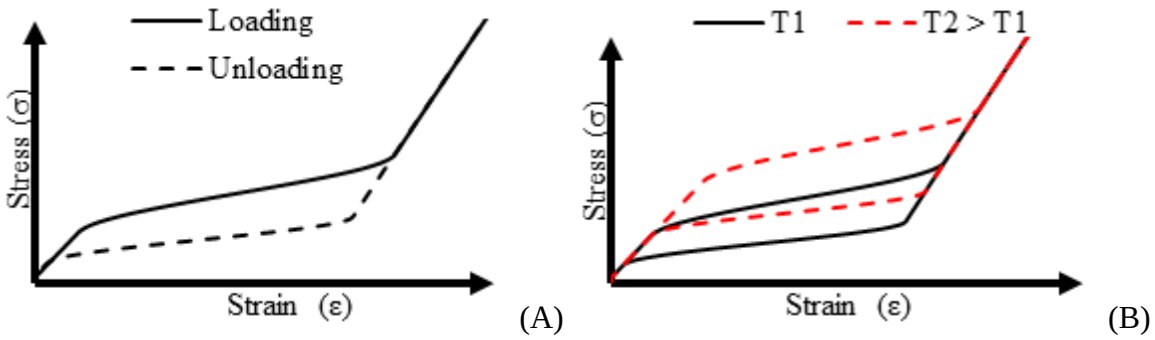

Figure 2.5 Example Superelastic Curve (A) & at Two Temperatures (B)

The reversible phase change exhibited by shape memory alloys under thermal and mechanical loads yields unique responses of the SME and superelasticity. Superelasticity is the only effect which is studied herein for its use in actuation applications.

2.1.3. Polycrystaline Superelasticity

Idealized superelasticity is assumed to be uniform throughout samples. In practice, however, polycrystalline samples are likely to be used. There are many complexities which are introduced by polycrystallinity in superelasticity which are outside of the scope of this discussion (for more detail see [33]). One aspect worth further discussing in a simplified manner is the micro-stress distribution within polycrystalline samples and the resultant phenomenon of ***tr****ansformation* ***i****nduced* ***p****lasticity (TRIP)* [34].

Since the phase change which causes superelasticity is monoclinic, it is expected that the loading and unloading curves are dependent on the crystal orientation. It has been shown experimentally that only a fraction of grains are observed to transform during loading [35], and that not all grains will transform when loaded to a given stress or strain. In order to transform, the grains must be loaded perpendicular to their transformation axis ("*on-axis"*) [36]. Load cases which do not have a component perpendicular to the transformation axis will be referred to as *"off-axis."*

To examine the effects of polycrystalline superelasticity, let us take a hypothetical SMA sample. In this perfect sample, there are three equally sized grains, each of whose transformation axis is oriented along one of the three coordinate directions (X, Y, and Z), as shown in Figure 2.6. In this case, the ends of all the grains are bound so they all undergo the same strain.

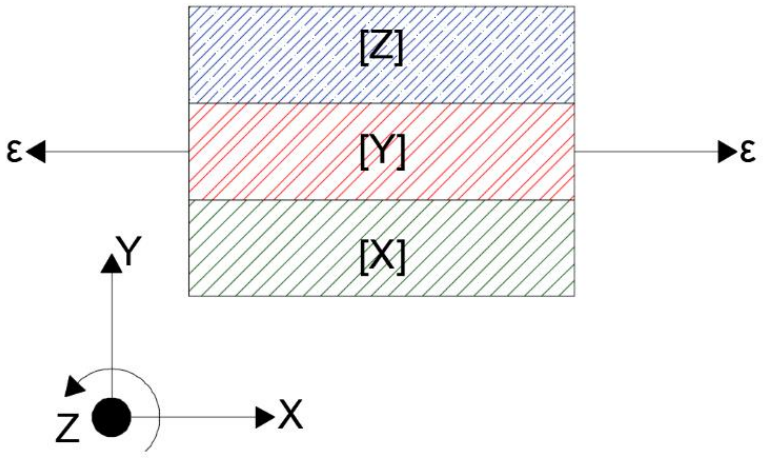

Figure 2.6 Sample with One Grain Oriented along each Coordinate Axis (X, Y, and Z)

When strained along the X axis, all grains initially all behave identically and support the same stress in the linear elastic region (see Figure 2.7). When the loading plateau start stress ($\sigma_{Start\ Loading}^{Transformation}$) is reached, the stress distribution will no longer become uniform. As the sample is strained, the off-axis grain (X) will tend to take more stress as it is stiffer and linear elastic. The on-axis grains (Z and Y) will undergo superelasticity. At a certain strain, the off-axis grain (X) will reach it's yield stress and begin to plastically deform. Upon unloading, the off-axis grain (X) will have undergone plastic deformations which are irrecoverable. The on-axis grains (Z and Y) can theoretically recover the entirety the strain they were loaded to, however because their ends are fixed to those of the plastically deformed off-axis grain (X), they will remain strained. Since on-axis grains (Z and Y) remain superelastically strained, they remain partially transformed to martensite which introduces micro-stress and phase distributions into the system.

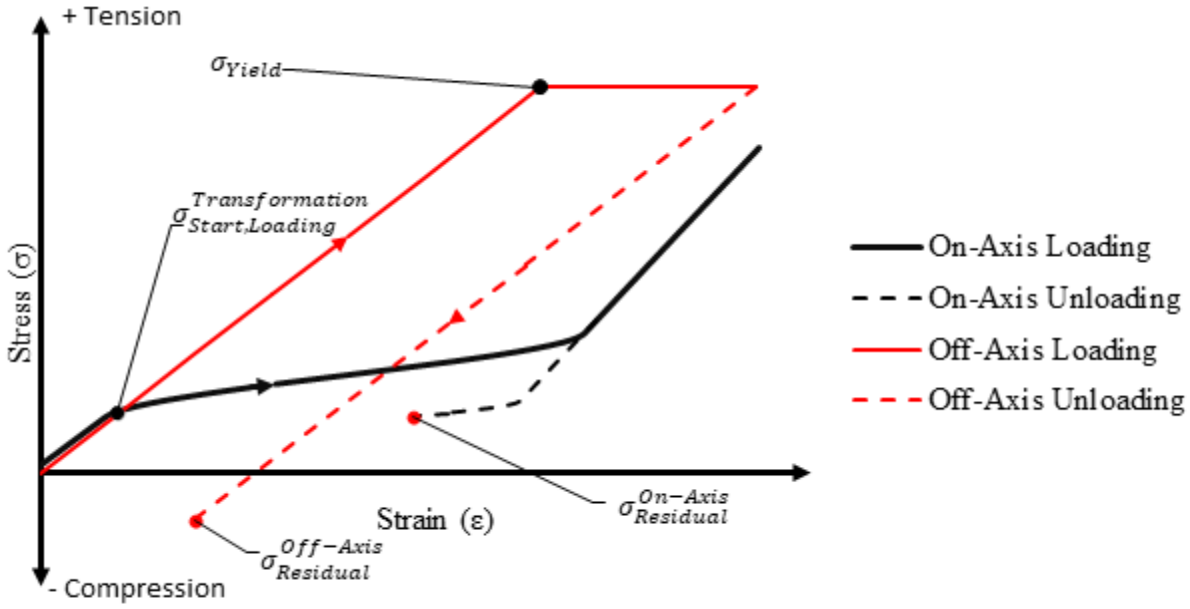

Figure 2.7 Example Stress-Strain Curves for On- & Off- Axis Loading

This illustrative example, though simplified for the sake of clarity, is interesting as it demonstrates that while the bulk-sample has undergone macro-stresses below the yield stress, the micro-stresses caused by transformation of certain grains may cause local yielding. This *TRIP* phenomenon is the underlying mechanism of *Functional Stabilization* (see **Section 2.1.4**).

2.1.4. Functional Stabilization

Functional stabilization[1] refers to the phenomenon that low-cycle mechanical loading – typically less than 100 cycles [37] – to as low as 10 [%] of the yield stress [38] stabilizes SMA thermal and mechanical behaviours [38]. A schematic of this behaviour adapted from work by [37], [39], [40] and an example stress-stain curve are shown in Figure 2.8 (A) and (B) respectively. During the first cycles, there are significant evolutions of all thermomechanical properties. Once stabilized properties may change at a reduced rate due to traditional fatigue [41]. The effect of cyclic loading on shape memory alloys is particularly challenging to measure due to the number of thermomechanical properties and variance in their stabilization rates [42].

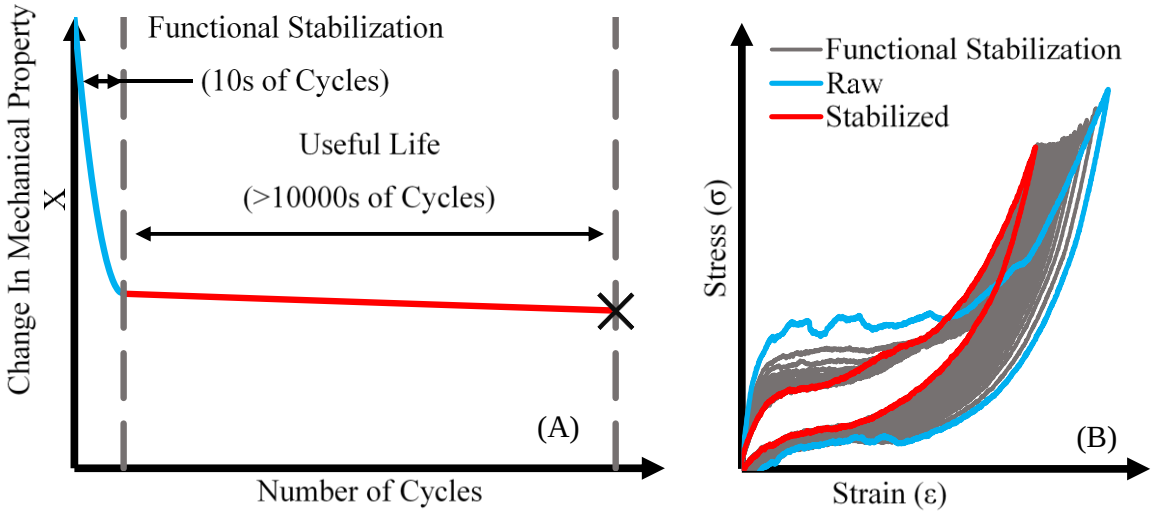

Figure 2.8 Schematic of Functional Stabilization adapted from [37], [39], [40] (A) and Example Functional Stabilization Stress Strain Curve (B)

As discussed by Filip & Mazanec, functional stabilization is caused by plastic dislocations which impart non-uniform local stresses at the microstructural level, thereby changing the phase distribution [43]. It is well established that functional stabilization effects both mechanical and thermal SMA properties [44]–[50]. Auricchio et. Al. describe the mechanical changes qualitatively, stating that the loading and unloading plateau start and end stresses decrease while plastic deformation increases [42]. Lagoudas et. Al. show that austenite and martensite peak

[1] The literature also refers to "functional stabilization" as "functional fatigue" and "training." Training has another meaning in the context of the Two Way Shape Memory Effect [37] and fatigue is often used in engineering to refer to high-cycle effects. The terms "functional stabilization" and "stabilization" are used in this work to refer to this phenomenon and prevent confusion with others.

temperatures increase after the wire has been stabilized [49]. Functional stabilization's effects on SMAs is clear in the literature, thus there is need for stabilization prior to thermomechanical characterization and integration into end-use applications.

Quantifying functional stabilization and the resultant thermomechanical behavior presents a unique challenge. Functional stabilization changes all thermomechanical properties by different amounts and at different rates. As a result, all properties must be measured if a traditional property based approach is used [37], [50]. Further confusing the study of functional stabilization is the constitutive model which one chooses defines the thermomechanical properties for the stabilization study. A lack of consensus on SMA constitutive models makes many stabilization studies incommensurate with one another. For example, the Auricchio & Taylor model [51] includes plateau start and end stresses while the Lagoudas & Boyd model [52] uses energy variables to describe superelasticity. Furthermore, both these models differ from the ASTM standard properties for SMAs [53]. The number of properties and differences between constitutive models are both challenges that need to be overcome to study SMA functional stabilization.

A hysteresis energy method of studying functional stabilization which solves these problems was adapted by Moumni [54] from metal plasticity (see Halford [55]) and further studied by Morin [56]. To summarize this method, the hysteresis energy – effectively the area between the loading and unloading curves shown in Figure 2.9 (A) – is evaluated at each cycle. When the area stops changing the sample is said to have stabilized. Change in hysteresis energy – shown in Figure 2.9 (B) – approaches zero when mechanical properties have stabilized. Note that true stress and true strain are used to evaluate hysteresis energy, and thus is what is shown on relevant stress-strain curves in this document.

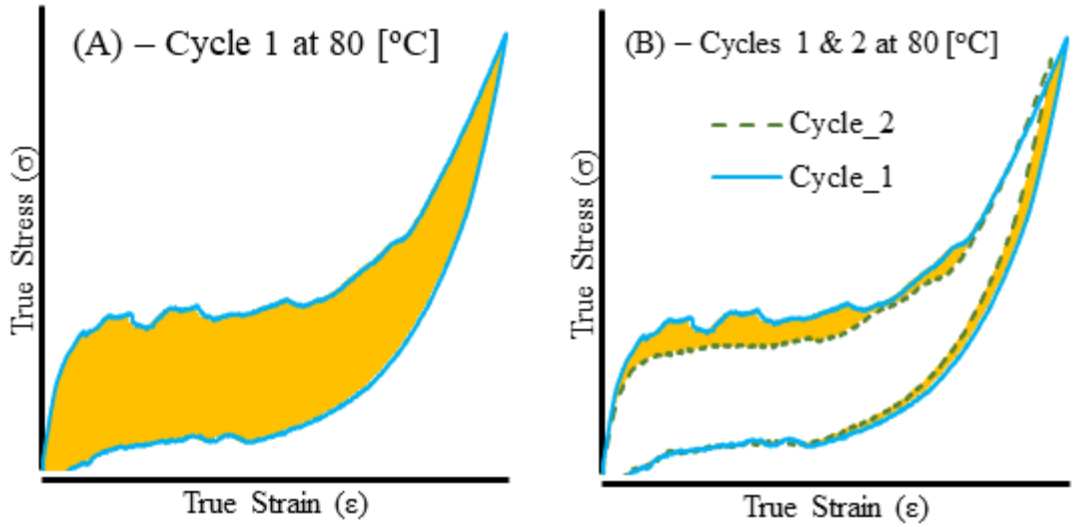

Figure 2.9 True Stress-Strain Curve Area Shaded for (A) Hysteresis Energy and (B) Change in Hysteresis Energy

There are two key benefits to using a hysteresis energy approach to study SMA functional stabilization. Firstly, it's constitutive model agnostic and solely reliant on experimental data, solving incommensurability issues. Secondly, it's numerically evaluable from raw data, thus removing uncertainty introduced when mechanical properties are measured. Change in hysteresis energy will approach zero to when mechanical properties stabilize for all chemistries of this material family, making change-in hysteresis energy more suitable for comparison of functional stabilization behaviors than hysteresis energy itself. For these reasons, change in hysteresis energy will be used as the parameter for evaluating functional stabilization in this study. Moumni [54] and Morin [56] show that an exponential function can be used to describe functional stabilization. Their expression used in this study, adapted to fit the change hysteresis energy between cycles, is shown in Eqn. 2.1.

Eqn. 2.1. Change in hysteresis energy for functional stabilization

$$\underset{2\leq n\leq N}{\boldsymbol{\Delta HE_{n,n-1}}} = \boldsymbol{a} * (\boldsymbol{n}-\boldsymbol{1})^{\boldsymbol{b}}$$

$$n = \ Current\ Cycle\ Number$$

$$N = Total\ Number\ of\ Cycles$$

$$a = \Delta HE_{2,1} \rightarrow Hysteresis\ Energy\ Difference\ Between\ the\ First\ Two\ Cycles$$

$$b = Stabilization\ Constant$$

2.1.5. Electrical Behaviour of SMAs

Central to the use of SMAs in control and sensing applications is their electrical response, which is especially useful if thermal, electrical, and mechanical phenomena are coupled together. The specific property of interest is electrical resistivity (ρ, [ohm mm]) which is a function of crystal lattice structure, chemical composition, and grain-scale defects [57]. For SMAs, this poses the opportunity to infer information about crystal structure – and thus phase – using electrical signal for in-situ samples (i.e. those embedded in SMAHCs). Electrical resistivity is an established method for measuring SMA phase (see [58]).

Thermo-electro-mechanical experiments have been performed on SMAs before, including by Antonucci et. Al. [59]

2.2. Finite Element Analysis of Superelastic SMAs

There are a number of phenomenological models for superelasticity – (see references [38], [52], [60]–[63]). Commercialization of finite element models for shape memory alloys is recent at the time of writing, with 2018 being the first year a superelasticity model was integrated into ABAQUS\CAE. ABAQUS [64] and MSC Marc [65] use the Auricchio & Taylor Model for two-phase SMAs. While it is possible to integrate a proprietary material model in many finite element softwares, it is beneficial to use an integrated model which is already validated, as one can be confident unforeseen issues arise from other model components.

The ABAQUS implementation of Auricchio & Taylor's model is used for this finite element model (FEM). The details of this model are presented in [51]. Of note is that the Auricchio & Taylor model does not include R-Phase effects, so care must be taken when using it to model ternary NiTi(X) alloys. Presented in Figure 2.10 are example isothermal-stress-strain and plateau stress-temperature curves. Table 2.1 includes mechanical properties and brief descriptions required for implementing this model. There are twelve mechanical properties required for characterizing tensile behavior of an SMA using the Auricchio & Taylor model with a thirteenth term for compressive behavior.

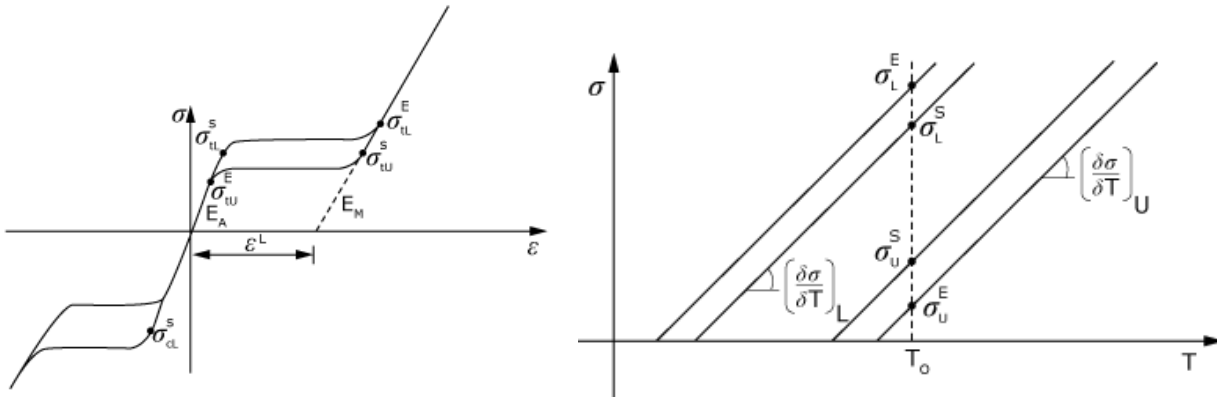

(A) (B)

Figure 2.10 Stress-Strain (A) and Stress-Temperature (B) Behavior of Auricchio-Taylor Model SMAs [64]

Table 2.1 Thermomechanical Properties for Auricchio & Taylor Model SMAs [64]

E_A	Young's Modulus of austenite	υ_A	Poisson's Ratio of austenite
E_M	Young's Modulus of martensite	υ_M	Poisson's Ratio of martensite
σ_{tL}^S	Stress at which phase transformation begins upon loading	σ_{tU}^S	Stress at which phase transformation begins upon unloading
σ_{tL}^E	Stress at which phase transformation ends upon unloading	σ_{tU}^E	Stress at which phase transformation ends upon unloading
ε^L	The projected elastic strain of the martensite phase	σ_{cL}^S	Stress at which phase transformation begins upon compressive loading.
$\left(\frac{\delta\sigma}{\delta T}\right)_L$	Linear dependency of beginning of and end of transformation stresses upon loading	$\left(\frac{\delta\sigma}{\delta T}\right)_U$	Linear dependency of beginning of and end of transformation stresses upon unloading
T_o	Reference temperature for superelastic properties		

There are a few key comments which to be made about using the Auricchio-Taylor model [64], as implemented in ABAQUS, for this study:

1. True shape memory is not accounted for as the martensitic twinning and detwinning processes are omitted, and the initial Young's modulus is always that of austenite.
2. Isotropy is assumed for this model.
3. This model only accounts for one phase transition. Therefore, it may not be suitable for alloys which have intermediary phases.
4. There are 12 thermoelastic properties required for characterizing superelastic behavior under tensile loading, presenting a challenge in terms of material characterization.
5. This model does not directly integrate prestrain or prestress values.
6. T_0 is the reference temperature at which material properties are inputted into ABAQUS, which is not related to the phase transformation temperatures.

Care must be taken when specifying the reference temperature (T_0), which is not a material property but rather a user selected value. The selection of this value will affect convergence, especially as it has the potential to cause zero stiffness in the model if not correctly specified. Unloading transformation end stress (σ_{tU}^{E}) is the first to approach zero when heating into superelastic and cooling into SME regimes (see Figure 2.10(B)). Therefore, unloading transformation end stress is of interest when selecting a T_0 to ensure convergence.

Based on the Auricchio & Taylor Model (see Figure 2.10 and Table 2.1), unloading transformation end stress is calculated as in Eqn. 2.2.

Eqn. 2.2. Unloading Transformation End Stress: $\sigma_{tU}^{E}(T) = \sigma_{tU}^{E}|_{T_0} + \int_{T_0}^{T} \left(\frac{\delta\sigma}{\delta T}\right)_U dT$

Where:

$\sigma_{tU}^{E}|_{T_0} = Unloading$ transformation $end\ stress\ at\ refererence\ temperature\ (T_0)$

$\sigma_{tU}^{E}(T) = Unloading$ transformation $end\ Ssress\ as\ a\ function\ of\ temperature\ (T)$

$\left(\frac{\delta\sigma}{\delta T}\right)_U = The\ slope\ of\ the\ linear\ Unloading\ Stress\ vs. Temperature\ curve$

From Figure 2.10(B), the unloading transformation end stress can be represented as a piecewise linear function to represent the superelastic and shape memory regimes:

Eqn. 2.3. Piecewise function representing the calculation of unloading transformation end stress as a function of temperature in Superelastic and Shape Memory Regimes

$$\sigma_{tU}^{E}(T) = \begin{cases} 0 & , \ T \leq A_f \ , \ (Shape\ Memory) \\ \sigma_{tU}^{E}|_{T_o} + (T - T_o)\left(\frac{\delta\sigma}{\delta T}\right)_U & , \ T > A_f \ , \ (Superelastic) \end{cases}$$

Evaluating this expression in the limit where the reference temperature (T_0) approaches the austenite finish temperature (A_f) yields:

$$\lim_{\boldsymbol{T_0 \to A_f}} \left(\sigma_{tU}^{E}(T)\right) = \begin{cases} 0 & , \ T \leq A_f \ , \ (Shape\ Memory) \\ \sigma_{tU}^{E}|_{\boldsymbol{A_f}} + (T - \boldsymbol{A_f})\left(\frac{\delta\sigma}{\delta T}\right)_U & , \ T > A_f \ , \ (Superelastic) \end{cases}$$

Evaluating the superelastic regime constant term, which is now in the SME regime:

$$\sigma_{tU}^{E}|_{\boldsymbol{A_f}} = \sigma_{tU}^{E}(A_f) = 0$$

Therefore:

$$\lim_{T_0 \to A_f} \left(\sigma_{tU}^{E}(T)\right) = \begin{cases} 0 & , \ T \leq A_f \ , \ (Shape\ Memory) \\ (\boldsymbol{T - A_f})\left(\frac{\boldsymbol{\delta\sigma}}{\boldsymbol{\delta T}}\right)_{\boldsymbol{U}} & , \ T > A_f \ , \ (Superelastic) \end{cases}$$

In the case where simulations are being performed at temperatures near to the A_f, which will occur when moving between superelastic and SME regimes:

$$(T - A_f) \to 0$$

Therefore:

$$\lim_{\boldsymbol{T}, T_0 \to A_f} \left(\sigma_{tU}^{E}(T)\right) = \begin{cases} 0 & , \ T \leq A_f \ , \ (Shape\ Memory) \\ 0 & , \ T > A_f \ , \ (Superelastic) \end{cases}$$

Eqn. 2.4. Limit of unloading transformation end stress as reference temperature approaches A_f

$$\lim_{T, T_0 \to A_f} \left(\sigma_{tU}^{E}(T)\right) = 0$$

The transformation end stress approaching zero may introduce errors in its computation and thus the convergence of the finite element problem. Therefore, in the interest of computational efficiency, two conditions (Eqn. 2.5 and Eqn. 2.6) can be recommended for selecting a reference temperature (T_0).

Eqn. 2.5. Temperature bounds to ensure differentiability between SME and superelastic regimes, thereby preventing non-convergence when simulating near A_f.

$$T_0 \gg A_f$$

Eqn. 2.6. Reference unloading transformation end stress to guide the selection of T_o to minimize truncation error

$$\sigma_{tU}^{E}|_{T_o} \approx (T - T_o)\left(\frac{\delta\sigma}{\delta T}\right)_U$$

To conclude, the phenomenological finite-element representation of SMAs thermomechanical behavior must be done with care. Firstly, it must be checked that the model – in this case the Auricchio-Taylor – is suitable for the material. Secondly, several properties must be measured experimentally, and must be inputted into finite element software in a way which supports convergence.

2.3. Thermomechanical Characterization of Shape Memory Alloys

2.3.1. SMA Thermomechanical Characterization Outline

SMA thermomechanical characterization is an active field of research and development as discussed by Hartl et. Al. [66], with methodologies as abundant as modelling approaches. The two-step basic approach is clear and often performed as in [67]–[70]. First, differential scanning calorimetry (DSC) is used to measure thermal behaviour, for which the relevant standard is ASTM F2004-17 [71]. Second, some form of mechanical loading at varied temperatures to measure thermally dependent mechanical behaviour. Complicating characterization is the well documented change in thermomechanical behaviour due to cyclic loading [44]–[50], the phenomenon referred to as "*functional stabilization*" (see **Section 2.1.4**), whose effects must be accounted for.

This section begins with a brief introduction to standards for SMA characterization. With this information, an experimental process for thermomechanical characterizing SMAs – which includes functional stabilization – is proposed. Following this, experimental results are presented and discussed to demonstrate the usefulness of the proposed approach and extract data for simulation.

2.3.2. Standards for SMA Thermomechanical Characterization

Given the nascency of this field, there are limited standards available for SMA characterization. ASTM F2516-14 [72] is the relevant standard for tensile testing, but is limited as it studies behaviour at one temperature and makes no mention of functional stabilization. Since it omits thermal and stabilization effects, ASTM F2516-14 is insufficient for the complete characterization of SMAs for actuation applications or simulation using the Auricchio & Taylor model. ASTM recently addressed the thermomechanical response of SMAs in the E3098-17 [73] and E3097-17 [74] standards. Neither of these methods directly measure responses relevant to characterization for the Auricchio & Taylor model and do not provide any insight into functional stabilization. Clearly, there is work to be done to develop characterization practices which characterize stable SMA behaviours and are compatible with commercial finite element models.

2.3.3. Proposed Thermomechanical Characterization Method

To fully characterize SMA thermomechanical tensile behaviour, a method which studies the thermomechanical properties as well as functional stabilization is required. The proposed methodology is designed for tensile tests but is adaptable to other loading modes (i.e. torsion). Steps one through three are used to characterize functional stabilization while steps four through six are used to characterize the end-use SMA behaviour. Outlined in Figure 2.11 is the proposed methodology, with details of each step following. Where possible, ASTM methods are adapted.

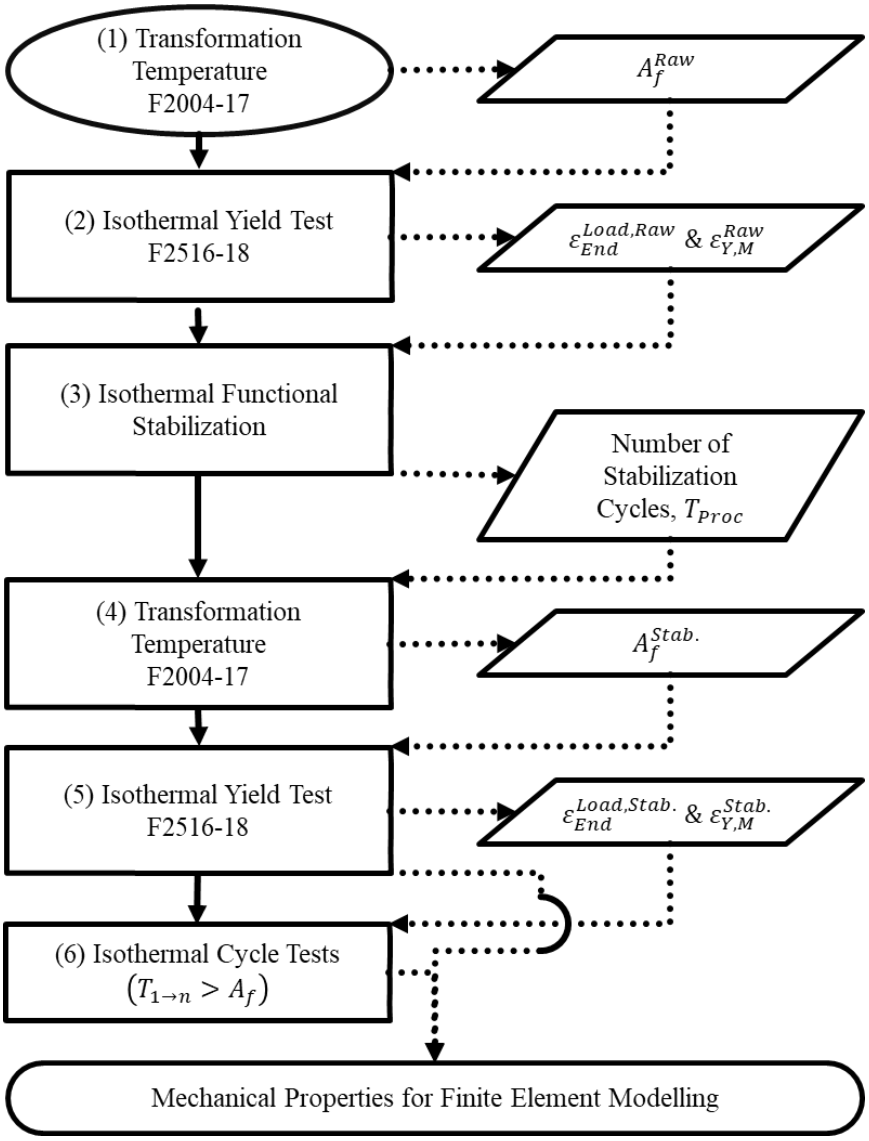

Figure 2.11 SMA Thermomechanical Characterization Flow Chart

Step 1. Differential Scanning Calorimetry (Raw Stock) → $A_{f,Raw}$

DSC is performed on raw SMA wire according to ASTM F2004-17 [71]. The transition temperatures of raw samples are measured, and the raw austenite finish temperature ($A_{f,Raw}$) is used to define temperatures for tensile testing.

Step 2. Isothermal Tensile Yield Tests → $\varepsilon_{Y,Raw}^{M}$ & $\varepsilon_{L,E,\,Raw}^{T}$

Tensile tests are performed according to ASTM F2516-14 [72] with one modification, which is that the first load cycle is not performed as this information is not used. Tests are conducted at three or more temperatures above the $A_{f,Raw}$. These tests are used to measure the raw stock yield ($\varepsilon_{Y,Raw}^{M}$) and at the end-of-loading-transformation ($\varepsilon_{L,E,\,Raw}^{T}$) strains. This test is used to define a suitable strain range for functional stabilization testing.

Step 3. Isothermal Functional Stabilization Tests → T_{Proc} & Number of Cycles

Functional stabilization tests are performed by cyclically loading raw samples in a range of zero to some max strain ($0 \leq \varepsilon \leq \varepsilon_{max}$) where the maximum strain is between the end of transformation and yield strains defined in the prior tests ($\varepsilon_{L,E,\,Raw}^{T} < \varepsilon_{max} < \varepsilon_{Y,Raw}^{M}$). The use of displacement control is important, as functional stabilization has significant effects on stress plateaus [42] and displacement rate can be controlled directly without any concern for stress nonlinearity. Ideally the sample is strained to halfway between the aforementioned strain limits, allowing for changes due to plastic deformation and of end-of-loading strain during stabilization. Ensuring that the sample is loaded past the end-of-loading-transformation strain every cycle ensures that the sample's transformation is complete and potential TRIP is realized. These tests should be similar to those used in Step 2, except with many cycles run below yield. These tests should be performed at the same temperature intervals as the previous Isothermal Tensile Yield Tests to define the optimal processing temperature (T_{Proc}). Given that the austenite finish temperature will increase [49], the lowest temperature interval measured should be above $A_{f,Raw}$ – ASTM recommends 5 [^{o}C] [72] – to ensure that the sample is superelastic. Using this information and a suitable functional stabilization analysis technique, the number of cycles required to stabilize properties can be measured.

Step 4. Differential Scanning Calorimetry → A_f (Stabilized Samples)

DSC tests from Step 1 are repeated on stabilized samples to measure the transition temperatures of stabilized material. This is used to define the true transition temperatures for end-use applications, as well as the A_f for subsequent testing.

Step 5. Isothermal Tensile Yield Tests → ε_Y^M & $\varepsilon_{L,E}^T$

Isothermal tensile yield tests from Step 2 are repeated on stabilized samples to measure the true yield (ε_Y^M) and at the end-of-loading-transformation ($\varepsilon_{L,E}^T$) strains for end use applications and subsequent testing.

Step 6. Isothermal Tensile Cyclic Tests

Isothermal tensile cyclic tests are performed to measure superelastic material properties. This is done on functionally stabilized samples using a similar process, except only one load-unload cycle is required for each stabilized sample at each isotherm.

2.3.4. Experimental Setups & Procedures

In this section experimental setups and procedures for both DSC and tensile tests are described, including the relevant standards and modifications.

All tests are performed using a 0.150 ± 0.008 [mm] wire composed of 44.86 Ni – Ti 10.06 Cu [wt%]. The wire is supplied by Furukawa Electric Europe LTD. [75] with a thin oxide surface layer and is straight annealed. It is referred to herein as NiTiCu1.

2.3.4.1. DSC Experimental Setups & Procedures

DSC is performed according to ASTM F2004-17 [71] on a TA Instruments Q200 DSC. All samples are between 5-10 [mg] and prepared in hermetically sealed aluminum pans, with an additional similar pan used as the reference. Four heating and cooling cycles, from 20→120 → 20 [^oC] are performed with a ramp rate of 10 [$\frac{^oC}{min}$].

Wires are cut into short lengths and placed inside the pans, which imparts some stress and thus a phase change. The first cycle is used to induce the SME through unconstrained recovery and allow samples to recover their unstressed and unstrained phase distribution. The differences between the first cycle and the second through fourth cycles is always apparent but inconsistent, as shown in Figure 2.12. Due to the sample preparation effects on phase distribution, transition temperatures can only be measured from the second cycle onwards.

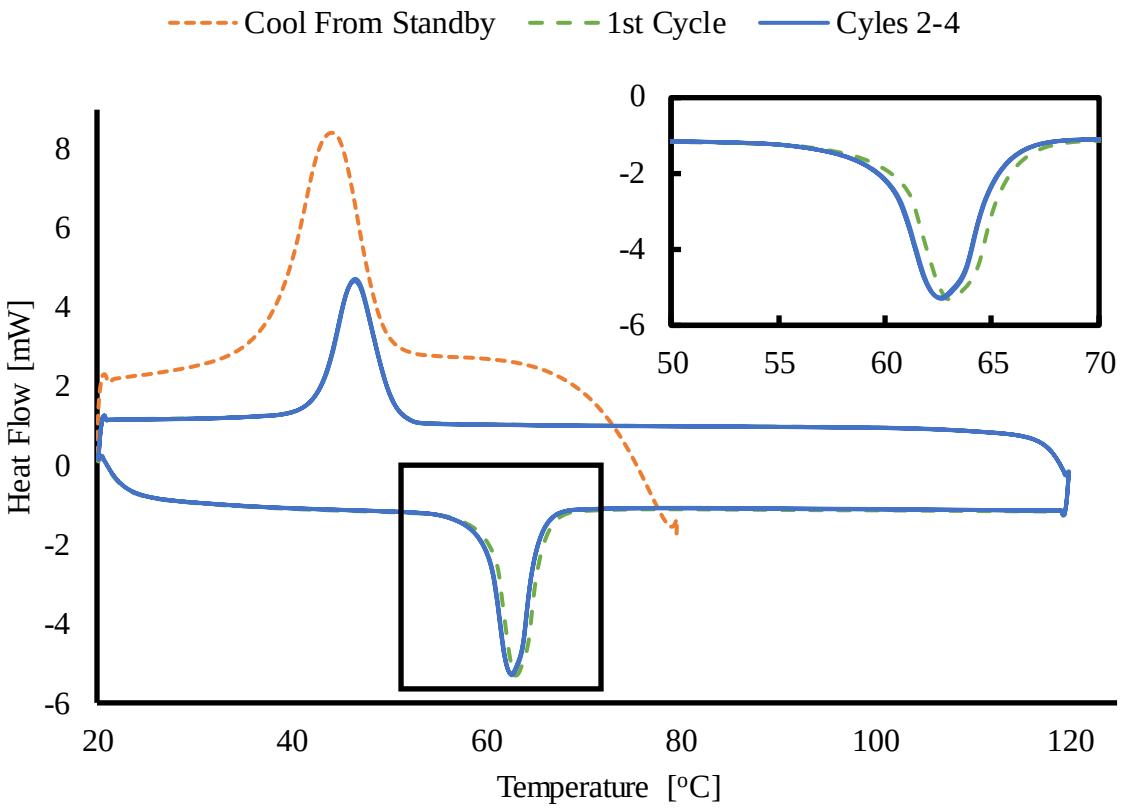

Figure 2.12 First through Fourth Cycle DSC Results for NiTiCu1

2.3.4.2. Tensile Test Experimental Setup & Procedure

Two types of tensile tests – cyclic and yield – are performed for this study, both of which are adapted from ASTM F2516-14 [72]. All tensile tests are performed on a Walter+Bai AG LFM electromechanical testing machine with a Class 0.5 GTM KS 2.5kN load cell inside a Noske-Kaeser environmental chamber. Due to the use of a wire and environmental chamber, displacements are measured using the UTM instead of an extensometer. Shown in Figure 2.13 is an image and diagram of the test apparatus, including the custom pulley fixture for testing wires.

(A)

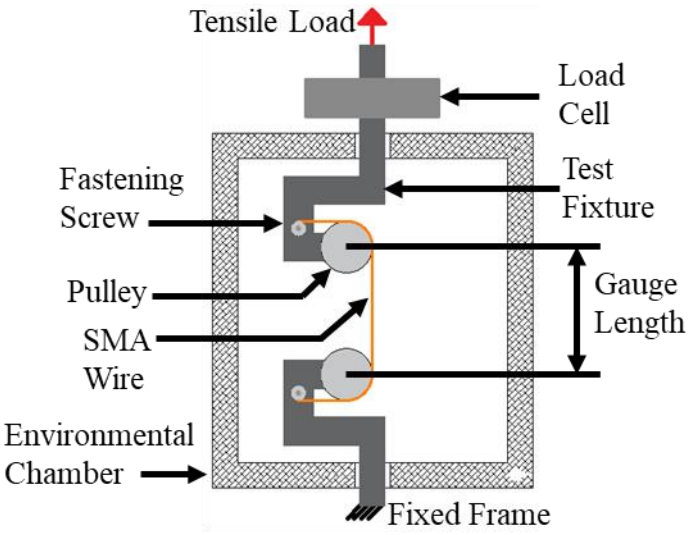

(B)

Figure 2.13 Tensile Test Setup Image (A) and Diagram (B)

All tensile tests are performed at a displacement rate of 0.30 [$\frac{mm}{s}$], below the ASTM specified maximum strain rate of 80 [$\frac{m\varepsilon}{min}$] [72] for nominal sample gauge length of 250 [mm] between pulley centres. The pulleys are assumed to be frictionless and not effect the SMA response. Cyclically tested samples are strained to 60 [mε] as per ASTM F2516-14 or in the range ($\varepsilon_{L,E}^{T} < \varepsilon_{Y}^{M}$).

Prior to installing the samples, the load cell force is zeroed. To install the samples, wires are wrapped around the pulleys and clamped with the fastening screws. The environmental chamber is then stabilized at the desired temperature. At this point, the distance between pulley centres is reduced until the load reaches zero, indicating no stress on the wire. The length at zero load is the true initial length used for strain calculations. All samples have an initial length greater than 225 [mm] to ensure compliance with the ASTM specified strain rate. The displacement is zeroed, and the test is conducted.

2.3.5. Experimental Results

In this section experimental results are presented and discussed in the context of the proposed SMA characterization method and simulation using the Auricchio & Taylor model.

2.3.5.1. Raw SMA DSC Results

Raw SMA samples' transition temperatures are measured using the DSC. Transformation temperatures are measured as per [71]. Of interest is the austenite finish temperature (A_f), above which superelasticity is observed. DSC results are presented in Table 2.2 with Figure 2.2 showing where the temperatures are measured.

Table 2.2 Raw Sample DSC Results

	Mean (S_x)
Austenite Start (A_S) [ºC]	59.7 (0.266)
Austenite Peak (A_P) [ºC]	62.9 (0.224)
Austenite Finish (A_F) [ºC]	65.6 (0.297)
Martensite Start (M_S) [ºC]	50.7 (0.172)
Martensite Peak (M_P) [ºC]	46.3 (0.260)
Martensite Finish (M_F) [ºC]	42.4 (0.411)
Heating Endotherm [J/g]	17.8 (0.740)
Cooling Exotherm [J/g]	17.5 (0.660)

Importantly, these tests show only one each of endothermic and exothermic peaks, indicating that there is no intermediary phase[s] (see Figure 2.19). This means that the Auricchio & Taylor model can be used to accurately represent the response of this material.

2.3.5.2. Raw Sample Isothermal Tensile Yield Tests

The second step of the recommended characterization process is the isothermal tensile yield test performed on raw samples. The tensile procedure is used with samples loaded until break. A total of six successful tests were performed, with two at each of three isotherms (70, 80, & 90 [ºC]). Since the values of these tests only serve to guide subsequent test setups, the low repetition count suffices. Sample stress strain curves for each isotherm are shown in Figure 2.14 with results presented in Table 2.3.

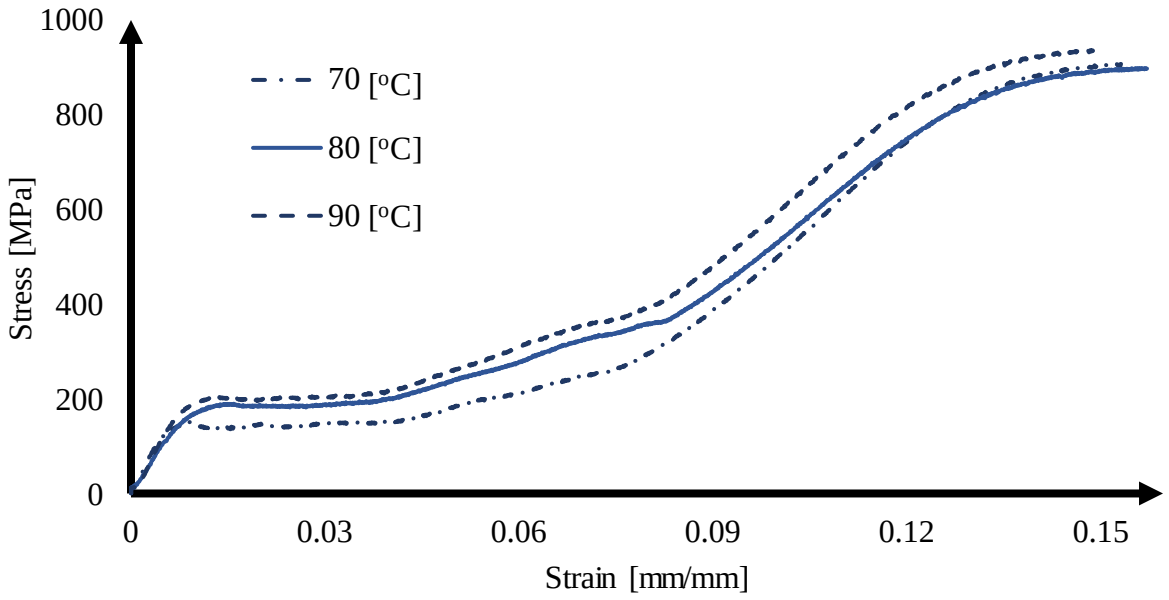

Figure 2.14 Isothermal Tensile Yield Test Results for Raw Samples

Table 2.3 Isothermal Tensile Yield Test Raw Sample Results

	Mean (Range) [mε]		
	70 [ºC]	**80 [ºC]**	**90 [ºC]**
End-of-Loading-Transformation Strain $\left(\varepsilon_{L,E,\,Raw}^{T}\right)$	81.8 (±0.176)	86.9 (±0.828)	85.9 (±0.681)
Yield Strain $\left(\varepsilon_{Y,Raw}^{M}\right)$	122 (±1.69)	121 (±1.92)	116 (±3.07)

With this data, the recommended maximum loading strain for the functional stabilization tests is in the range of $\mathbf{90 < \varepsilon_{max} < 116}$ $[\boldsymbol{m\varepsilon}]$**.** ASTM recommends loading to 60 [mε] [72], which would not complete the phase transformation, potentially causing inaccuracies in the measurement of properties. The ≥50 [%] difference in the ASTM recommended and measured results shows the importance of performing these isothermal tensile yield tests to ensure that subsequent cyclic tests are performed in a way that maximizes information which can be extracted.

2.3.5.3. Isothermal Functional stabilization Results

Isothermal functional stabilization tests are performed by cyclically loading the samples under the tensile conditions previously described. The maximum displacement is 15 [mm], or 60 [mε] of the nominal sample length of 250 [mm], as per the ASTM standard [72]. Two tests are run at each of three isotherms. Results for fifty cycles at each isotherm are shown in Figure 2.15.

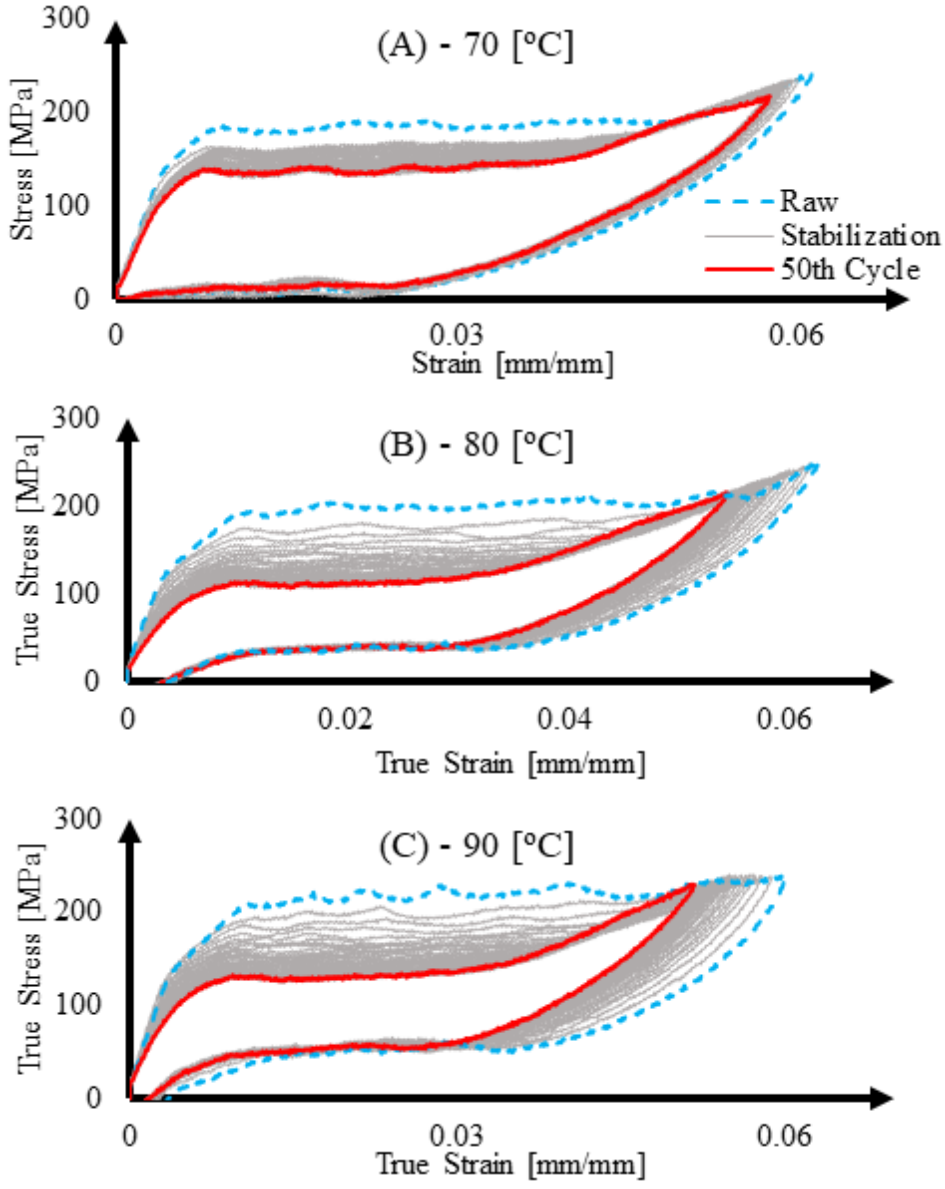

Figure 2.15 Stress-Strain Curves for Stabilization at 70 (A), 80 (B), and 90 (B) [°C]

The 70 [^{o}C] sample (in Figure 2.15. (A)) has an unstable lower plateau stress around 10 [MPa], which indicates that this temperature potentially too close to the A_f and not enabling superelasticity. At this temperature, 35.5 (±3.5) [mε] of plastic deformation occurs after 50 cycles.

Both the 80 and 90 [^{o}C] samples exhibit expected superelastic behaviours, indicating that these are more suitable temperatures for property stabilization. These samples exhibit 93 (±4.0) [mε] and 88.5 (±0.5) [mε] of plastic deformation respectively. For these temperatures, full transformation does not occur in the first few cycles. After five cycles, a clear loading plateau end develops. While sample length increases with cyclic loading due to plastic deformation, the strain at the end of the transformation decreases. This indicates that the martensite fraction is increasing as the sample is stabilized through TRIP.

At 70 [^{o}C] the lower plateau stress is unstable, indicating a greater margin above DSC measured A_f temperature is required to allow for functional stabilization. The reduction in strain required for transformation indicates an increased martensite volume fraction in stabilized samples, which is expected to have thermal effects. From these two observations, it is indicated that thermal behaviour will change and that the DSC tests should be repeated after functional stabilization is studied.

Qualitatively, it is observable that the area between loading and unloading curves (hysteresis energy) is much larger in the 70 [^{o}C] test than both the 80 and 90 [^{o}C] tests. As described by Morin [56] the hysteresis energy is expected to be the same for all loadings above the A_f, simply shifted on the stress-strain curve according to temperature. This gives another indication that a greater A_f margin is required to allow for changes when samples are stabilized. Shown in Figure 2.16 is the change in hysteresis energy each isotherm, with fits performed using Eqn. 2.1.

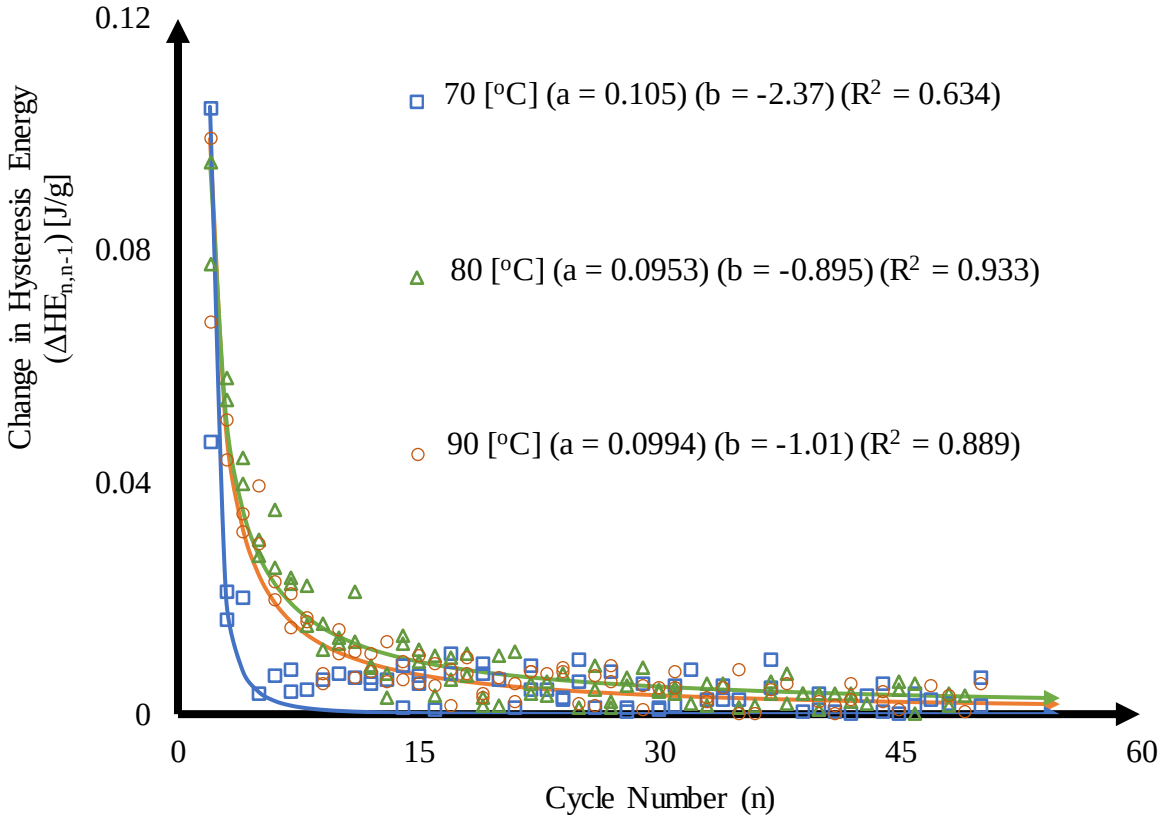

Figure 2.16 Hysteresis Energy vs. Number of Cycles at 70, 80, & 90 [°C]

Looking only at the hysteresis energy results, it appears that properties stabilize most quickly at 70 [°C]. However, when looking at the stress strain curves, it becomes clear that the mechanical behaviour at 70 [°C] is not characteristic of superelasticity despite being above the initially measured A_f. A word of caution when using the hysteresis energy method is then, that one must validate the superelastic response visually on the stress-strain curve even when the temperature is above A_f as it too changes with functional stabilization.

There is no significant difference in the hysteresis energy change trends between 80 and 90 [°C], results. This is consistent with Morin's observation that temperature simply should shift the hysteresis area on the stress-strain curve without changing the hysteresis energy value [56]. With this knowledge, 80 [°C] is selected for further study as the lower stress levels to reduce the opportunity for sample slippage or break while the temperature is high enough to ensure superelasticity during functional stabilizing.

A second set of functional stabilization tests is run at 80 [°C], this time loading the samples to 25 [mm], or 100 [mε] of the 250 [mm] nominal initial length. This strain is selected as it is within the window defined in the isothermal tensile yield tests. Three repeats are performed. A sample true stress-strain curve which includes the 1st and 50th cycles is shown in Figure 2.17 with the hysteresis energy change results plotted in Figure 2.18.

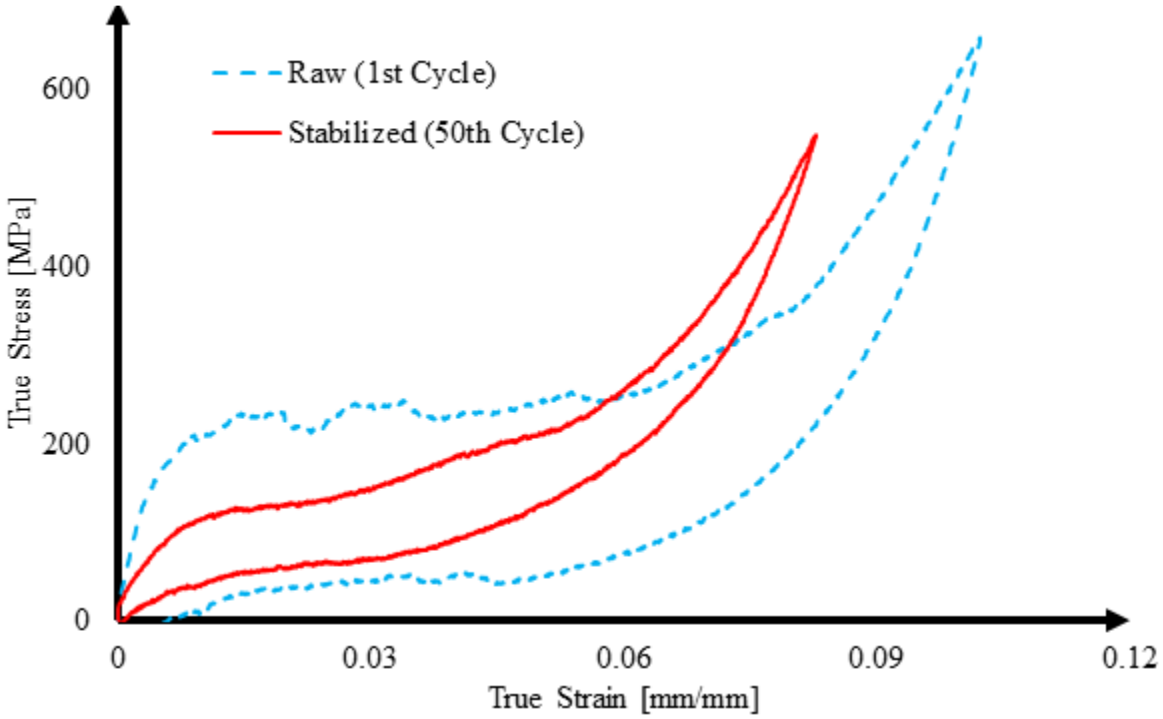

Figure 2.17 True Stress-Strain Curve for 50 Cycles at 80 [°C] and 25 [mm] Displacement

It is observed in the true stress-strain curves (Figure 2.17) that complete transformation occurs for the 50th cycle (and thus all subsequent cycles). Here again, the trend that the end-of-loading plateau strain reduces as the plastic strain increases is seen. To study this quantitatively, the hysteresis energy change study is repeated, shown in Figure 2.18.

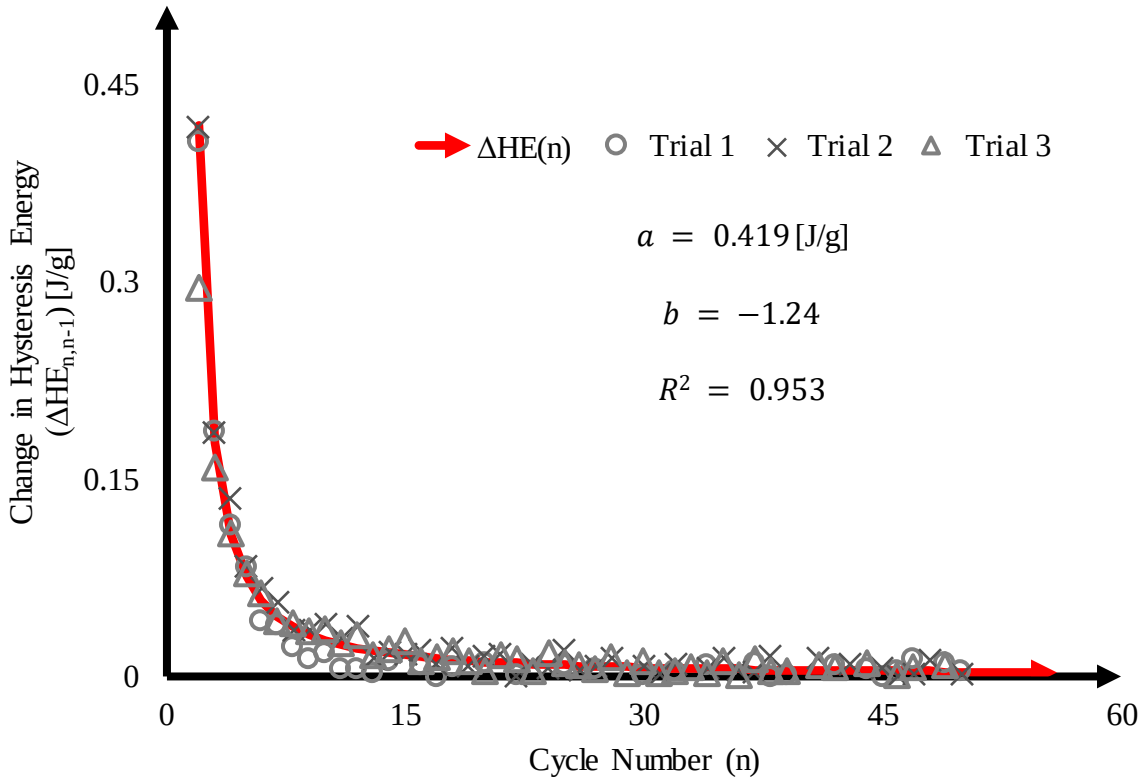

Figure 2.18 Stress-Strain Curve for 50 Cycles at 80 [°C] and 25 [mm] Displacement

The functional stabilization decay constant (b) is of greater magnitude when compared to samples strained to 60 [me], indicating that functional stabilization occurs more quickly when the samples are subjected to strains which complete transformation. This is expected, as the underlying mechanism of functional stabilization is TRIP, which can only completely occur when transformation is completed every cycle.

The fitted model shows that the samples follow the expected trend, with behaviour stabilizing rapidly after the first ten cycles. These results show that the hysteresis energy change reduces by two orders of magnitude over the first 43 cycles. Therefore, for this sample, 50 loading cycles provides sufficient property stabilization.

It's worth noting at this point that the chemistry as well as thermal and processing histories of the SMA being studied will vary the functional stabilization results. This approach is entirely phenomenological, and the numerical results are only applicable to the material studied.

Two sets of functional stabilization tests were performed, one set with 15 [mm] of displacement at three isotherms and one set with 25 [mm] of displacement at 80 [°C]. The first set of tests indicate

that functional stabilization effects phase distribution which must be considered when selecting a training temperature. It is also observed that above the A_f, hysteresis energy change appears independent of temperature which is consistent with prior work. The second set of tests show that a material-specific strain improves the functional stabilization response as complete transformation is ensured. These tests show that property stabilization is best performed at 80 [^oC] and 50 cycles for this material.

2.3.5.4. Stabilized Sample DSC Results

The functional stabilization results indicate a change in phase distribution due to TRIP and the resultant micro-stress distribution. To further investigate this, six samples of stabilized material are tested in the DSC to compare transition temperatures and transformation energy. Shown in Figure 2.19 are both stabilized and raw sample DSC results plot, with stabilized sample results in Table 2.4. Qualitatively, it's clear that the stabilized samples increase transformation temperatures and decrease the transformation energy.

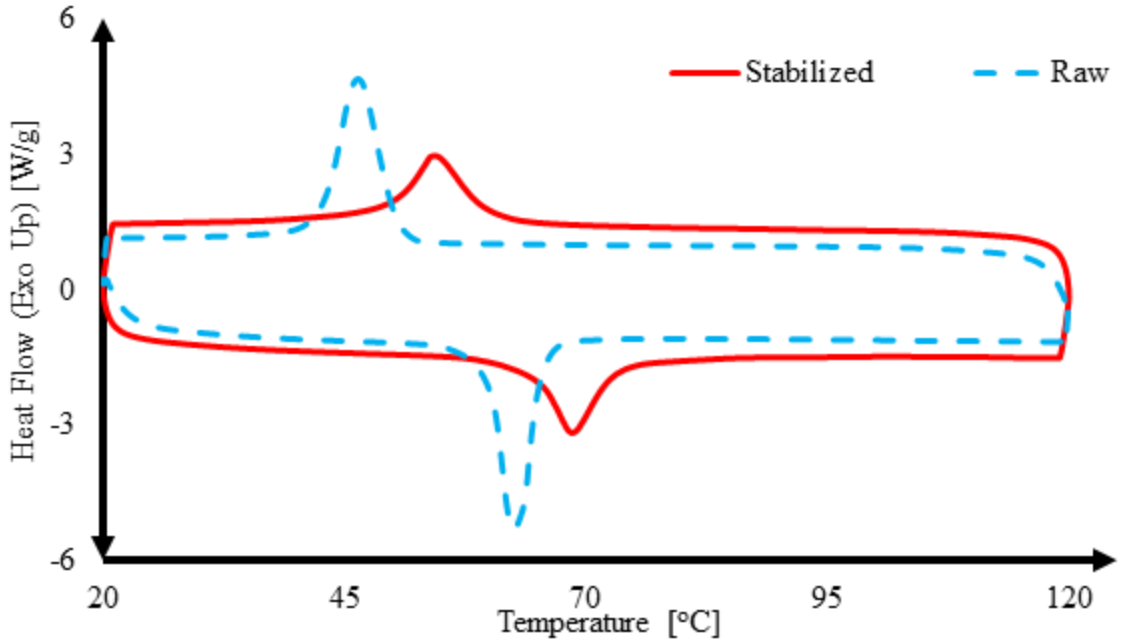

Figure 2.19 Stabilized vs. Raw DSC

Table 2.4 Stabilized Sample DSC Results

	Mean (S_x)
Austenite Start (A_S) [ºC]	63.4 (0.713)
Austenite Peak (A_P) [ºC]	68.3 (0.623)
Austenite Finish (A_F) [ºC]	73.5 (0.929)
Martensite Start (M_S) [ºC]	60.2 (0.374)
Martensite Peak (M_P) [ºC]	54.4 (0.357)
Martensite Finish (M_F) [ºC]	48.7 (0.476)
Heating Endotherm [J/g]	12.8 (0.457)
Cooling Exotherm [J/g]	12.4 (0.495)

To quantitatively study changes in thermal behaviour caused by functional stabilization, min-max-mean plots are created for transformation temperatures and energies, shown in Figure 2.20. The transformation temperatures all increase, but not by the same percentage. The specific energy of transformation is reduced by ~25 [%].

These observations indicate a change in phase distribution. Firstly, lower specific energies indicate less austenite is available for transformation (i.e. there is more martensite due to internal stresses). The increase in transformation temperatures can be explained by a change in micro-stress distribution. Grains which have been permanently transformed to martensite will be, locally, in tension. The increase in transformation temperatures indicates a greater minimum thermal energy is required for the phase change. This suggests that the grains available for transformation are in compression, as they require a greater excitation energy to cause phase change. The change in stress distribution is the result of TRIP. Given that the macro-stress in samples is still zero, the localized tensile and compressive micro-scale stresses must be in equilibrium. Taken together, the reduction of specific energies of transformation and increases in transition temperatures indicate a change in phase distribution because of functional stabilization.

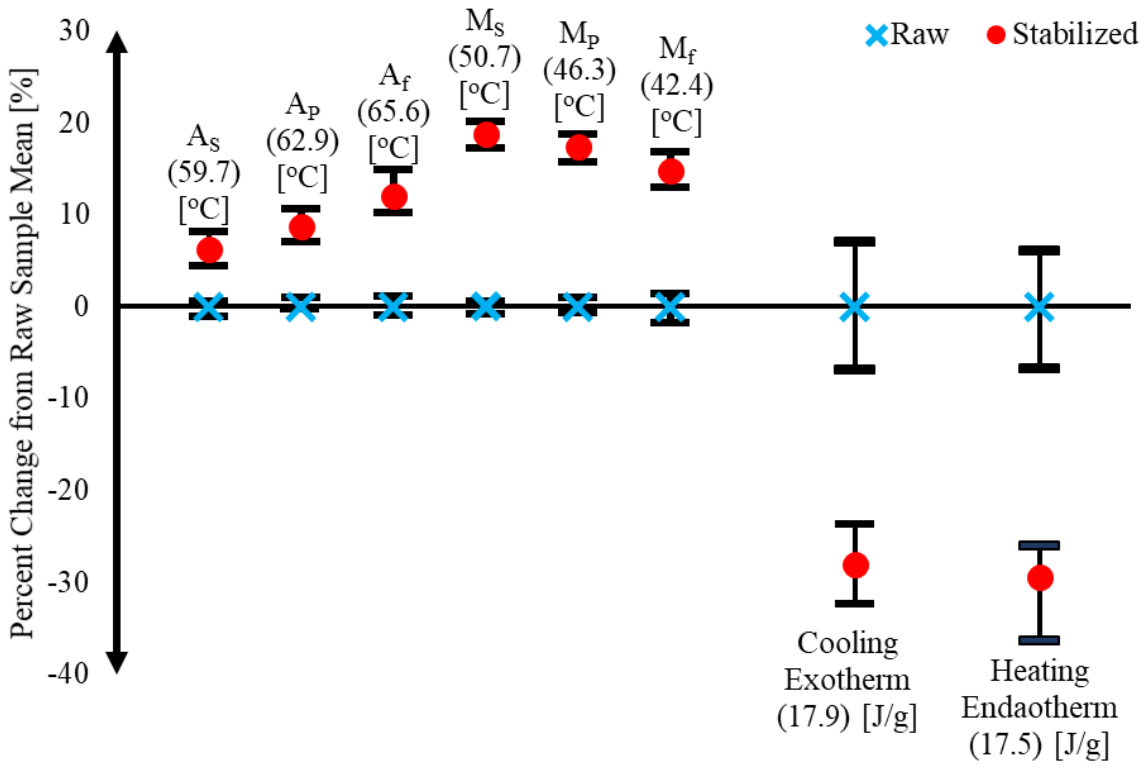

Figure 2.20 Transition Temperatures & Specific Transformation Energies for Raw and Stabilized Samples

The DSC tests performed on stabilized SMA samples show that there is a significant change in transformation temperature because of functional stabilization. This confirms the importance of studying functional stabilization when characterizing and designing with SMAs. A secondary practical benefit of stabilization in actuation applications is that the specific energy of transformation is reduced, which will increase cycle rate for a given power, as less heat will be absorbed or released.

2.3.5.5. Stabilized Sample Isothermal Tensile Yield Tests

To study the mechanical behaviour of stabilized samples, six yield tests are performed at 80 [°C]. Two stress strain curves are shown in Figure 2.21, one each of raw and stabilized samples. The mechanical behaviours, as expected, are entirely changed by the stabilization process.

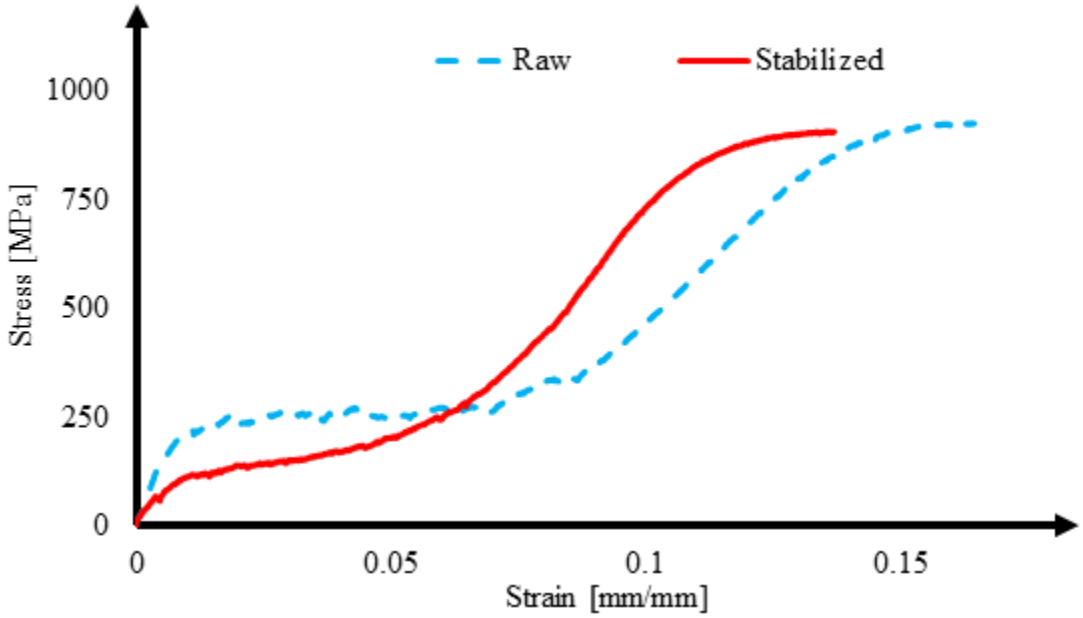

Figure 2.21 Raw and Stabilized Tensile Yield Test Results at 80 [°C]

Firstly, the acceptable range for maximum strain to ensure full transformation during cyclic loading is found to be $\mathbf{74 < \varepsilon_{max} < 104}$ [$\boldsymbol{m\varepsilon}$], which is a similar range to that of the raw samples, with outer bounds reduced by ~15 [mε] due to functional stabilization. The shift of this range indicates that less strain energy is required for transformation, independently confirming prior observations that less austenite is available for transformation. The measured mechanical properties of interest for simulation and subsequent tests are presented in Table 2.5.

Table 2.5 Tensile Yield Test Stabilized Samples Results at 80 [°C]

	Mean (S_x)
End-of-Loading-Transformation Strain ($\varepsilon_{L,E}^{T}$) [mε]	71.3 (2.37)
Yield Strain (ε_{Y}^{M}) [mε]	103.7 (3.37)
Austenite Young's Modulus (E_A) [GPa]	10.1 (0.495)
Martensite Young's Modulus (E_M) [GPa]	15.6 (0.545)

A quantitative study into the mechanical behaviour changes caused by functional stabilization is presented in Figure 2.22, where percent changes from the raw-sample-mean value are used for comparison. The strain energy is measured from zero stress to the end-of-loading transformation stress using true stress and true strain data.

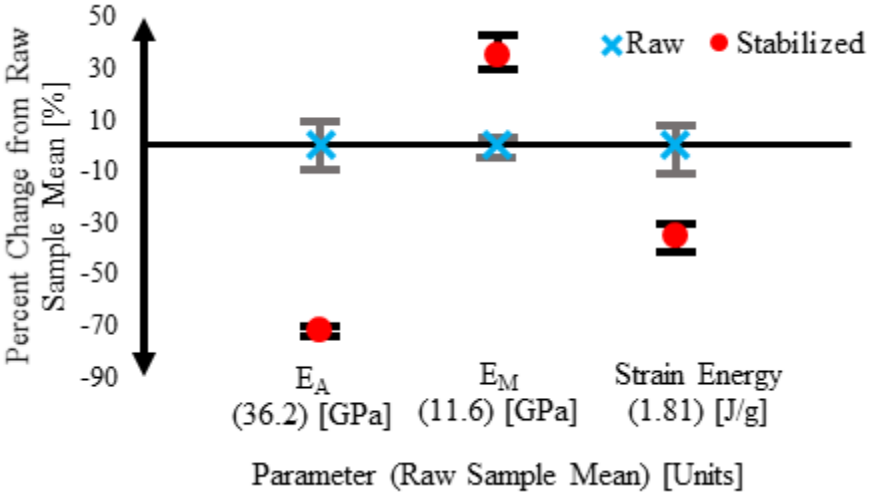

Figure 2.22 Comparison of Raw & Stabilized Mechanical Properties

After 50 cycles, the Young's Modulus of austenite is reduced while that of martensite is increased. The loading plateau appears to stiffen – as the starting stress is lesser and the ending stress is greater – after stabilization. The strain energy required for transformation is also reduced. Cumulatively, these changes further support the observation that less austenite is available for transformation due to functional stabilization. However, attempting to explain these results in terms of a volume fraction of martensite and austenite is insufficient as the percent change is not consistent across parameters. This is expected as other factors, such as change in micro-stress distribution, also contribute to the change in these properties.

It is interesting to look at strain energy for transformation, which reduces by a mean of 35.4 [%]. This indicates that there is less austenite available for transformation in the stabilized wire, consistent with the DSC results. Thermal energy for the same transformation path (martensite to austenite on tensile loading and cooling) reduces by a mean of 29.6 [%], which is close enough to indicate a correlation worthy of future investigation.

2.3.5.6. Stabilized Sample Isothermal Cyclic Tensile Tests

The final set of tests required for characterization are isothermal cyclic tensile tests. Three samples are tested at four isotherms with three cycles at each. In every case, samples are loaded within the strain range defined by the isothermal tensile yield tests to cause complete transformation without yield, which is $\mathbf{74} < \boldsymbol{\varepsilon_{max}} < \mathbf{104}$ $[\boldsymbol{m\varepsilon}]$**.** An example of these results is shown in Figure 2.23. Results from these tests are shown in Table 2.6.

Firstly, the expected relationships of transformation stresses increasing with temperature is observed. For the Auricchio & Taylor model, these relationships are assumed to be linear [64]. It is also observed that the loading and unloading transformation stresses change at difference rates, something a variance which is allowed for in the Auricchio & Taylor model.

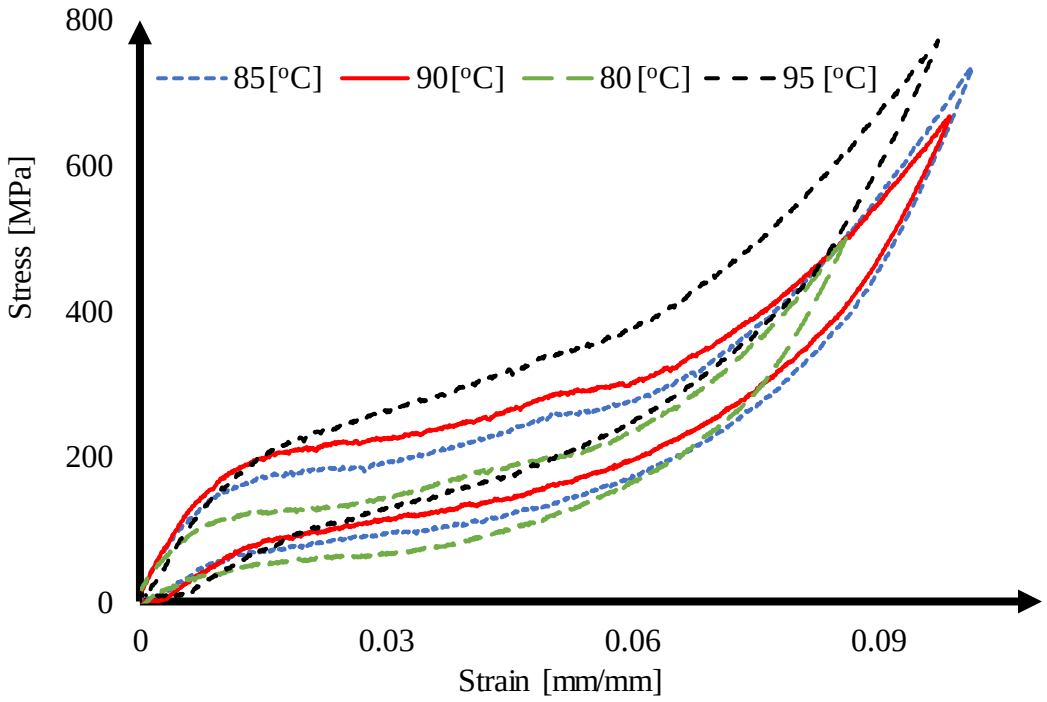

Figure 2.23 Isothermal Cyclic Tensile Test Stress-Strain Curve

Table 2.6 Isothermal Cyclic Tensile Test Results

	Mean Value
Loading Start of Transformation Stress (σ_{tL}^{S}) [MPa]	92.8
Loading End of Transformation Stress (σ_{tL}^{E}) [MPa]	240.
Unloading Start of Transformation Stress (σ_{tU}^{S}) [MPa]	120.
Unloading End of Transformation Stress (σ_{tU}^{E}) [MPa]	32.7
Projected Martensite Strain (ε^{L}) [mε]	53.5
Loading Stress-Temperature Slope $\left(\frac{\delta\sigma}{\delta T}\right)_{L}$ $[\frac{MPa}{^{o}C}]$	10.8
Unloading Stress-Temperature Slope $\left(\frac{\delta\sigma}{\delta T}\right)_{U}$ $[\frac{MPa}{^{o}C}]$	6.10

2.3.5.7. Summary of Experimental Results

A process for the thermomechanical characterization of SMAs which includes a quantitative investigation into functional stabilization is proposed in Figure 2.11 and used to characterize a NiTiCu SMA for the Aurrichio & Taylor model. Firstly, the DSC tests performed on raw samples show no R-Phase transition, confirming the applicability of the Auricchio & Taylor model to this material. After tensile yield tests, functional stabilization tests are performed at various isotherms. These functional stabilization tests show that the A_f changes due to functional stabilization and thus care must be taken to ensure superelasticity is observed. It is then shown that material-specific strains for functional stabilizing improves thermomechanical property stabilization rate. Tensile yield tests performed show the inconsistency with which mechanical properties change between raw and stabilized states as a percent. This indicates that it is not only a phase volume fraction change, but also a local stress change, which occurs during functional stabilization. Lastly cyclic tests are performed to measure the relationship between temperature and transformation stresses.

These results show the importance of characterizing functional stabilization when designing SMA actuators, and thus the significance of the proposed method. With these tests, the stable thermomechanical behaviour of a NiTiCu SMA is characterized, with final thermomechanical constants for the Auricchio & Taylor model presented in Table 2.7.

Table 2.7 Summary of Auricchio & Taylor Model Constants

	Mean Value
Austenite Young's Modulus (E_A) [GPa]	10.1
Martensite Young's Modulus (E_M) [GPa]	15.6
Loading Start of Transformation Stress (σ_{tL}^{S}) [MPa]	92.8
Loading End of Transformation Stress (σ_{tL}^{E}) [MPa]	240.
Unloading Start of Transformation Stress (σ_{tU}^{S}) [MPa]	120.
Unloading End of Transformation Stress (σ_{tU}^{E}) [MPa]	32.7
Projected Martensite Strain (ε^{L}) [mε]	53.5
Loading Stress-Temperature Slope $\left(\frac{\delta\sigma}{\delta T}\right)_L$ $[\frac{MPa}{^oC}]$	10.8
Unloading Stress-Temperature Slope $\left(\frac{\delta\sigma}{\delta T}\right)_U$ $[\frac{MPa}{^oC}]$	6.10
Reference Temperature (T_0) [°C]	80

2.4. Comparison of Finite Element & Experimental

A finite element model which simulates the experimental isothermal tensile loading tests is created using ABAQUS\Standard to compare finite element and experimental results. The model consists of a single SMA wire of 100 [mm] in length meshed with 10 B31 beam elements. On one end, the node is fixed in all degrees-of-freedom (DoF). On the other, the DoF along the wire axis is free. A tensile load is applied along this axis. A diagram of this model is shown in Figure 2.24.

Figure 2.24 SMA FEA Tensile Test Diagram

The finite element and experimental results for each of four isotherms is shown in Figure 2.25, from which two main observations can be made. Firstly, that the transition between linear and non-linear elastic regions is much "sharper" in the finite element simulations. Secondly, there is greater discrepancy between the FE and experimental results at elevated temperatures, indicating a non-linear stress-temperature relationship.

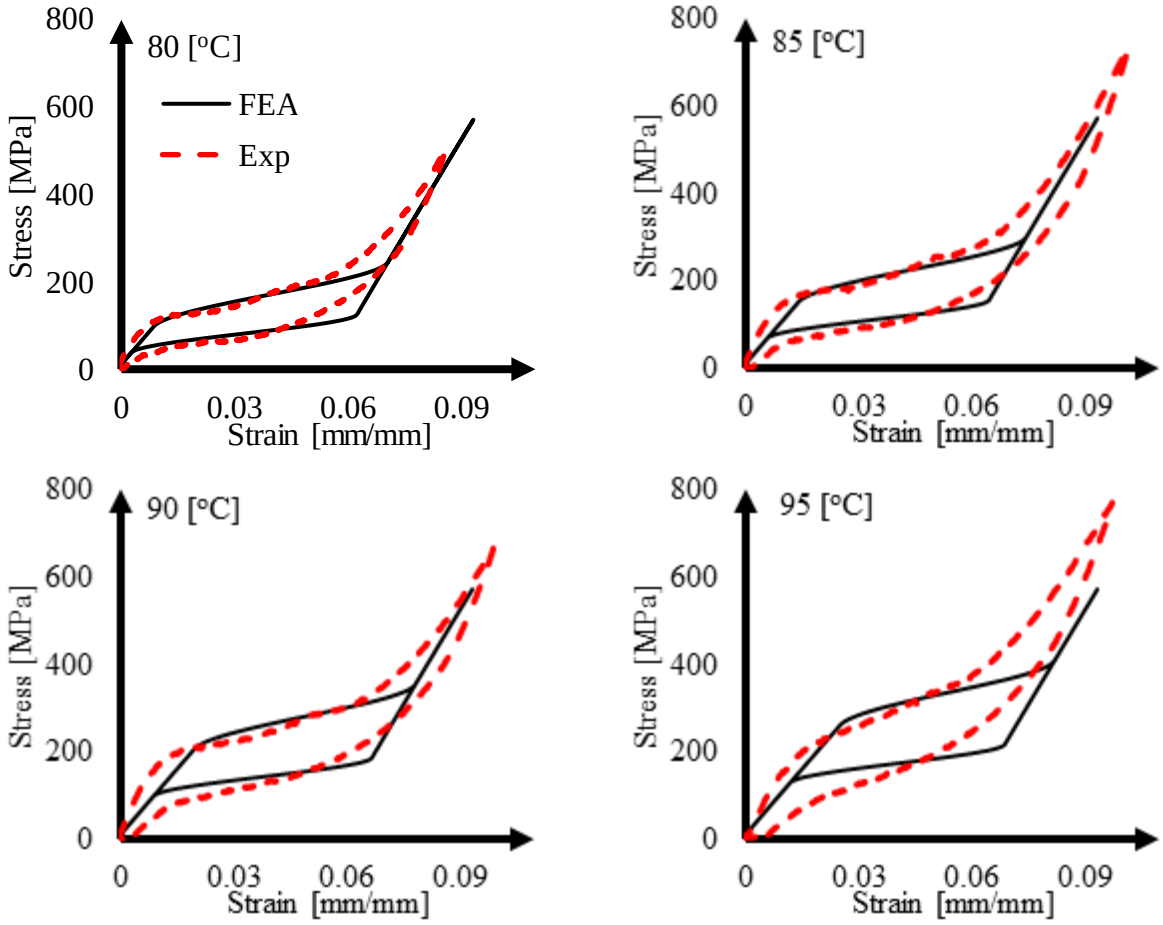

Figure 2.25 Finite Element & Experimental Isothermal Tensile Loading Results

Dealing with the first observation, the "sharpness" of the transition between linear and non-linear elastic regions, it's useful to first benchmark against Auricchio & Taylor's initial results when developing the model, shown in Figure 2.26. A similar discrepancy is clearly observed, particularly during unloading, with the linear FE model (which is used in ABAQUS) and the experimental data.

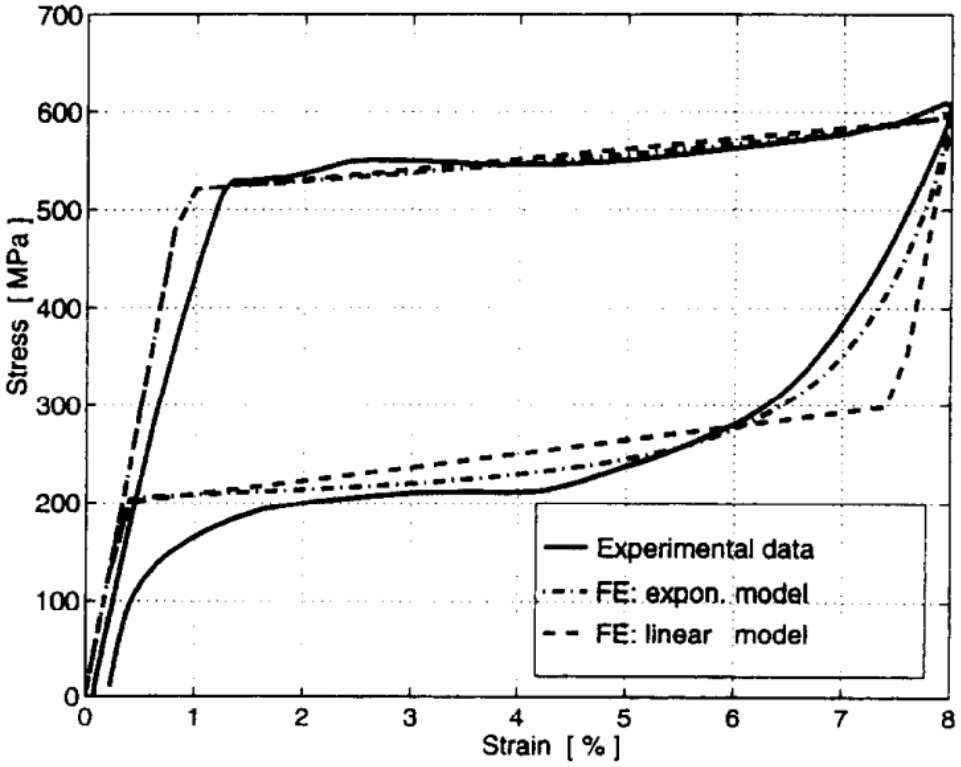

Figure 2.26 Auricchio & Taylor FE Models & Experimental Data [51]
Reprinted with permission from Elsevier

The Drucker-Praeger criterion used to model the transition between linear and non-linear regions [51] is expected to be the cause of this discrepancy. Auricchio & Taylor justify the use of the Drucker-Praeger criterion by citing the experimental work of Kakeshita et. Al. [76], which shows that the R→B19' phase transformation is hydrostatic pressure dependent. They also observe that the other phase transformations do not exhibit hydrostatic pressure dependence [76]. The hydrostatic pressure dependence of the R→B19' phase transformation and independence of others are also observed experimentally by Tartar & Yildirim [77] and predicted numerically by Wan et. Al. [78] and Bakhtiari et. Al. [79]. Clearly then, the assumption that hydrostatic pressure can be used to model all phase changes, when it demonstrably does not, introduces inaccuracy into this model. Secondly, the Auricchio & Taylor model is designed to model two-phase SMAs [51] which exhibit reversible path-independent phase changes. The ternary hydrostatic pressure dependent phase is path-dependent and not accounted for in the Auricchio & Taylor model, so this is a significant simplification in the context of this model.

The Auricchio & Taylor model also represents a mono-crystal and assumes transformation happens uniformly throughout the sample. In reality, due to the monoclinic nature of the phase transformation, the grain orientations in polycrystalline samples will affect the global transformation stresses.

Molecular dynamics simulations by Ko et. Al. [80] and Chowdhury et. Al. [81] show results which, qualitatively, are more similar to the experimental results, as shown in Figure 2.27. Notable similarities between MDS and experiments which are not observed in the Auricchio & Taylor FE model are:

1) Different loading and unloading behaviours
2) More gradual transitions between linear and non-linear regions
3) Irrecoverable strain

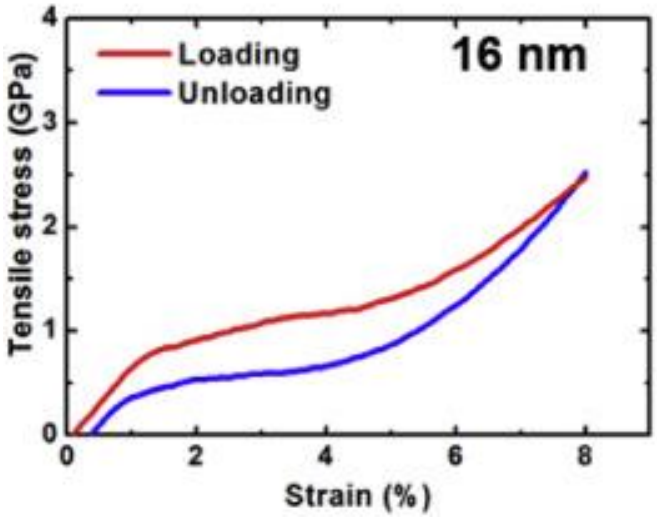

Figure 2.27 Molecular Dynamics Simulation Stress-Strain Results by Ko et. Al. [80]
Reprinted with permissions under Creative Commons CC BY NC ND

Figure 2.28 presents a close-up look of the plateau region – which is the region of interest for actuated composite structures – for both finite element and experimental results. Within the window of $25 \leq \varepsilon \leq 60$ $[m\varepsilon]$ there is better agreement between finite element and experimental results. This is because this excludes the transformation start and end where the mono-crystal and Drucker-Praeger assumptions break down significantly.

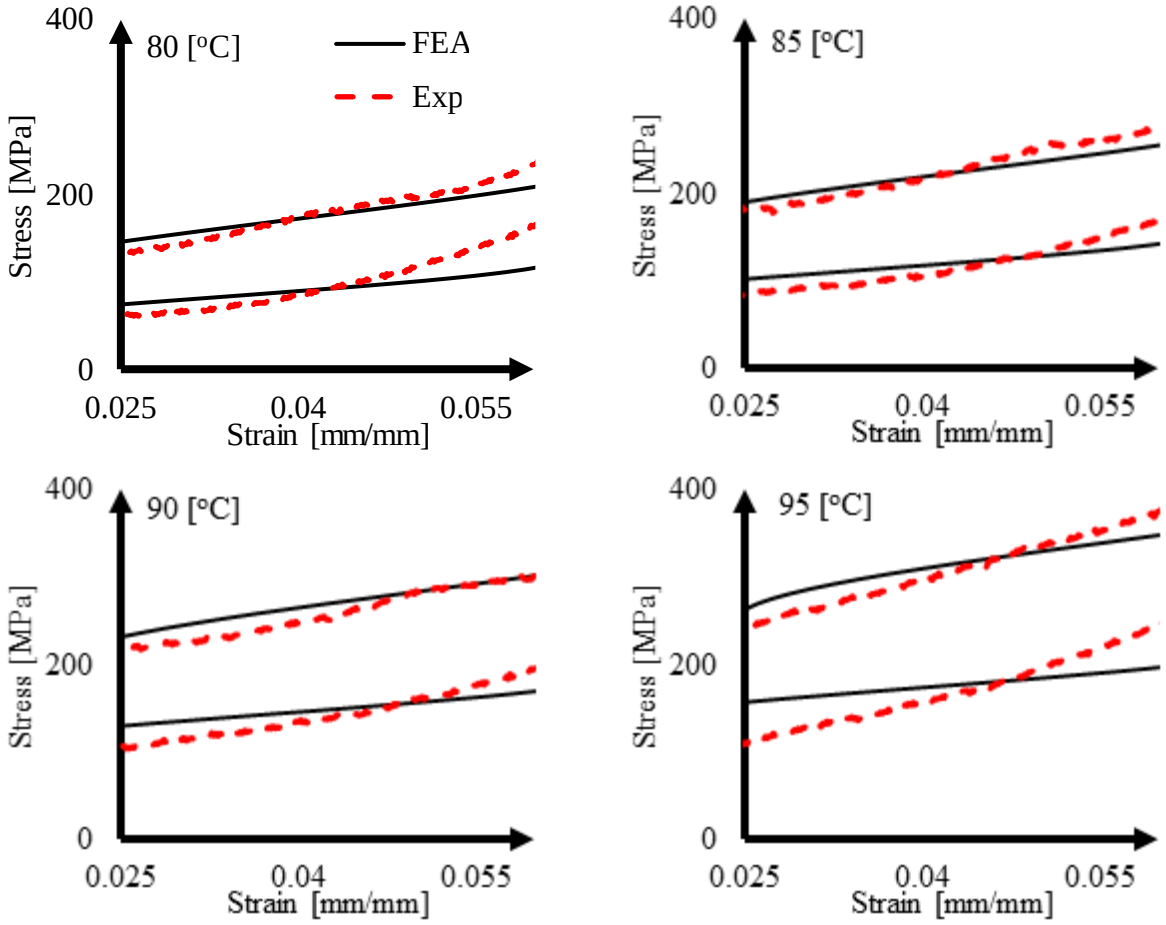

Figure 2.28 Finite Element & Experimental Isothermal Tensile Loading Results

To summarize the discussion, the Auricchio & Taylor finite element model for superelasticity is limited in accuracy due to the assumptions that phase transformations are hydrostatic pressure dependent, follow the Drucker-Praeger yield criterion, and that samples are mono-crystalline. Prior experimental and theoretical work demonstrates that these assumptions are invalid, particularly for two-phase SMAs. However, enough agreement is found for the Auricchio & Taylor model to be used as a model for proof-of-concept purposes, especially in the plateau region. Future work certainly includes investigating other models, and potentially using multi-scale modelling techniques to combine molecular dynamics and structural simulations.

2.5. Electrical Characterization of Shape Memory Alloys

In order to realize the goal of morphing SMAHC structures, consideration must be given to how these structures will be actuated and controlled. Given that SMAs undergo a crystal structure change and non-linear geometry changes, their electrical response to stress, strain, and temperature loads can be measured to provide insight to their current state. A brief investigation into the electrical characterization of shape memory alloys is conducted to develop an introductory familiarity of this topic and recommend avenues of future work. In the Master's thesis of Baptiste Guyon (EPFL) [82] – co-supervised by Sanesh Iyer & Prof. Pascal Hubert – a fixture was developed to enable the coupled thermo-electro-mechanical characterization of shape memory alloys (see Figure 2.29). The fixture allows SMA wires to be tested in tension inside the DMA environmental chamber, while simultaneously recording resistance measurements using an NI 9174 DAQ with a 9219 universal analog input cartridge.

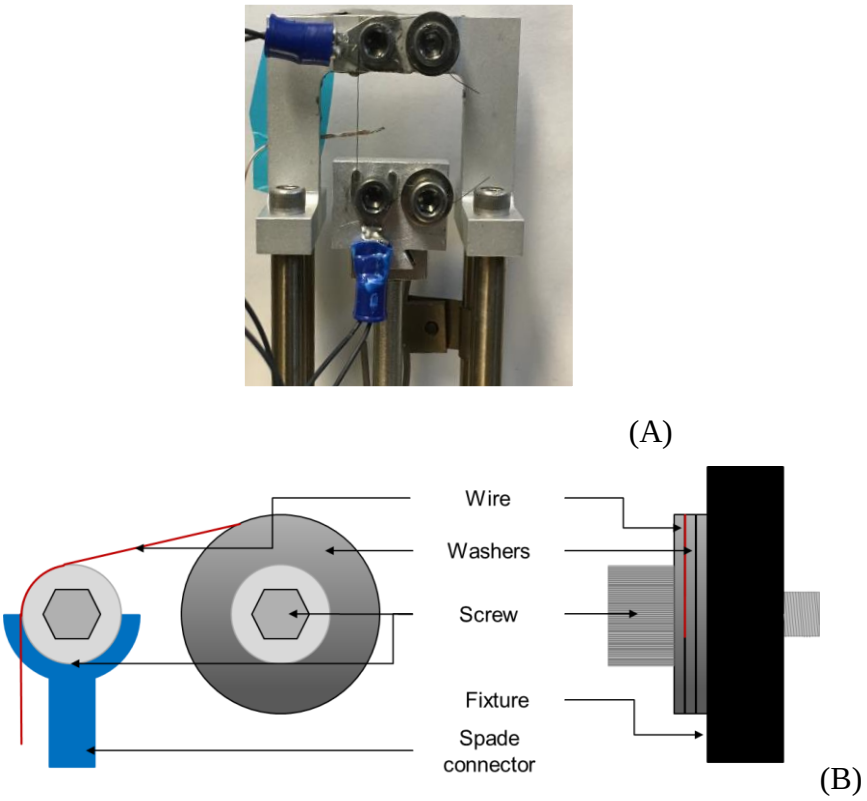

Figure 2.29 Thermo-Electro-Mechanical Characterization Fixture for TA Q800 DMA [82]

2.5.2. Fixture Calibration

B. Guyon performed calibration tests and proposed a calibration factor based on the *median* modulus measurement of a nylon sample [82]. However, the *mean* is the relevant factor to correct for the stiffness difference between the TA fixture and the new fixture, the experimental results of which are shown in Figure 2.30. A calibration factor of 4.75 [%] between means is measured. It is assumed that the calibration is constant in the testing range. The calibration factor will be applied to the force measurement from the DMA, according to Eqn. 2.7.

Eqn. 2.7. Resistivity Fixture Force Calibration Equation: $F_{Corrected} = 1.0475 * F_{Measured}$

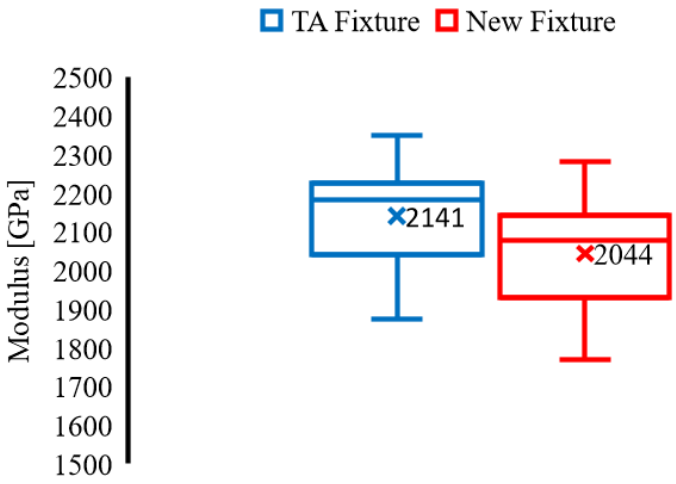

Figure 2.30 DMA Fixture Calibration Results adapted from B. Guyon [82]

2.5.3. Resistivity Measurement & Calculation

The experimental apparatus measures resistance of the wire using a four-wire resistance method to remove lead resistance [83]. Contact resistance is assumed to be negligible given that the contact area is two orders-of-magnitude greater than the wire diameter.

The measured variable is resistance, which is a combination of resistivity – a material property – and geometric factors of the sample. Since the goal is to measure resistivity under tensile load, an equation for it's calculation as a function of strain must be developed, as is done in Eqn. 2.8.

Eqn. 2.8. Resistance: $R(\varepsilon) = \rho(\varepsilon) * \frac{L(\varepsilon)}{A(\varepsilon)}$

Length and area – through the Poisson's Ratio – are both functions of tensile strain, which are shown in Eqn. 2.9 and Eqn. 2.10 respectively. Poisson's Ratio is assumed constant, as is commonly done with shape memory alloys [51], [52].

Eqn. 2.9. Sample Length: $L(\varepsilon) = L_o * (1 + \varepsilon)$

Eqn. 2.10. Sample Cross-Sectional Area: $A(\varepsilon) = \frac{\pi}{4} d_0^2 * (1 - v * \varepsilon)^2$

Combining these equations and rearranging them to calculate resistivity as a function of measured variables (resistance and strain) yields the equation that will be used to calculate resistivity at each strain increment.

Eqn. 2.11. Dynamic Resistivity (Iso-Poisson's Ratio)

$$\rho(\varepsilon) = R(\varepsilon) * \frac{\pi * d_0^2}{4 * L_o} * \frac{(1 - v * \varepsilon)^2}{(1 + \varepsilon)}$$

2.5.4. Yield Tests with Resistivity Measurements

Tensile yield tests are performed at 80 [°C] on a TA Q800 DMA with a maximum force of 18 [N] and a controlled loading rate of 0.1 [N/min] to investigate the transformation behaviour until yield. Four tests were conducted, whose results are shown in Figure 2.31. Normalized resistivity is used, as the results are very sensitive to the accuracy of the sample length measurement and normalization removes this measurement error for ease of comparison.

The tests exhibit similar curves, with the resistivity initially changing smoothly, followed by a significant jump which can be attributed to plastic dislocations being introduced at yield. The noise after yield can be attributed to plastic dislocations being introduced into the system.

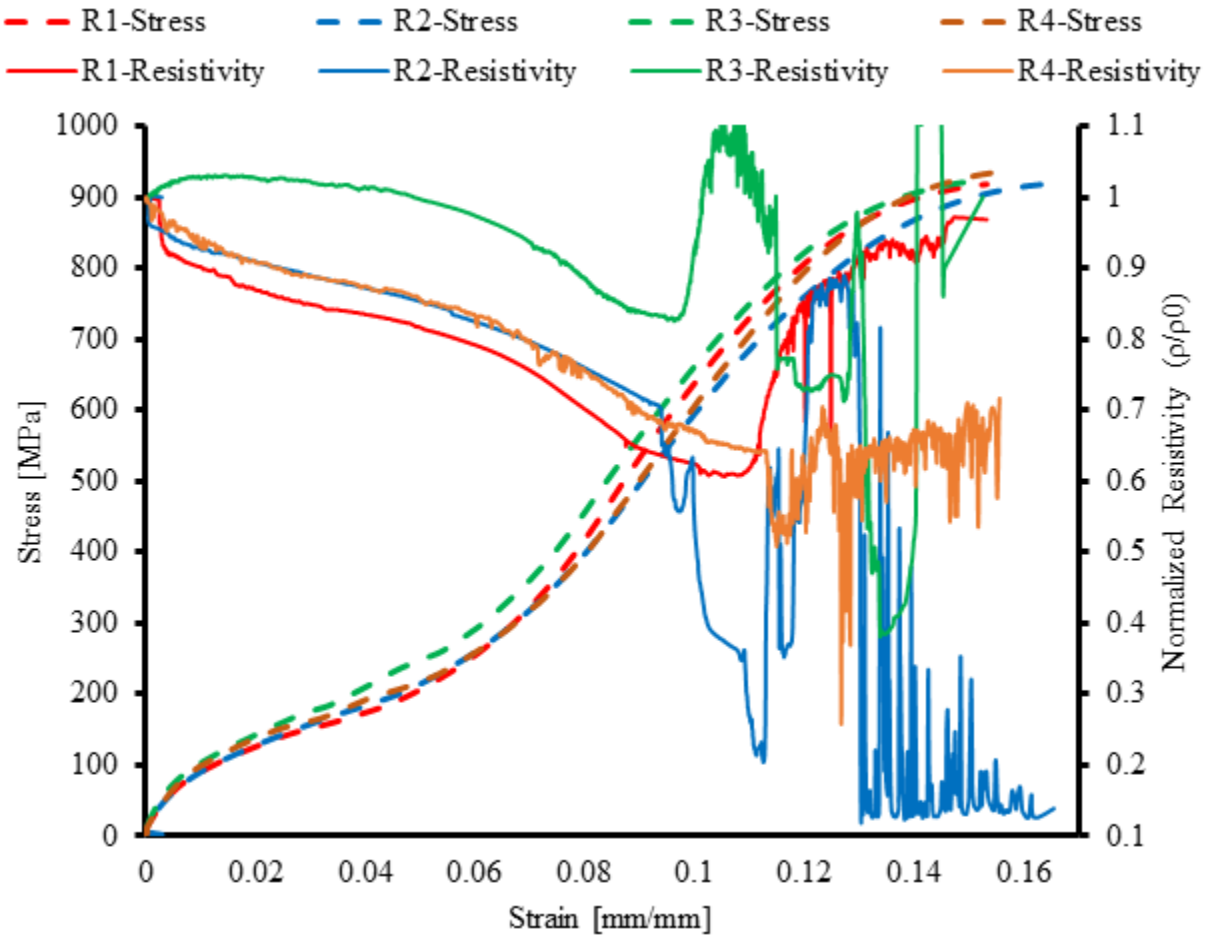

Figure 2.31 Yield Stress-Strain-Resistivity Response of NiTiCu1 (Four Repeats Shown)

Looking at a representative curve in Figure 2.32, and marking strains associated with the start of transformation A, end of transformation B, and yield C, the correlation between resistivity and stress can be analyzed.

Resistivity begins to change as soon as loading begins, indicating that the transformation begins very quickly once load is applied. This is unexpected, as prior to A no phase transformation is expected since the sample is in the linear austenite region. There is, however, a clear potential cause, the introduction of micro-stresses during stabilization. Grains which have high tensile stresses in the unloaded state due to functional stabilization will be primed for phase change with small applied tensile loads.

During the loading plateau, between A and B, a resistivity change is observed as well. The rate in this region is slower than prior to A or after B, which is unexpected as most of the phase change occurs in this region. Between B and C, the rate is faster again. These results indicate a more complex relationship between micro-stress distribution, grain orientation, and phase transformation. It is hypothesized that the underlying cause is the statistical distribution of grains, however extensive further work – which is outside of the scope of this thesis – is required to test this hypothesis.

There is also an offset between C – which marks failure as measured by the linearity of the stress-strain curve – and C’ which marks failure by a discontinuity in the resistivity-strain curve. This offset indicates that the transformation continues between C and C’, causing a non-linear response which leads to the incorrect prediction of yield stress when using traditional criterion for linear-elastic materials.

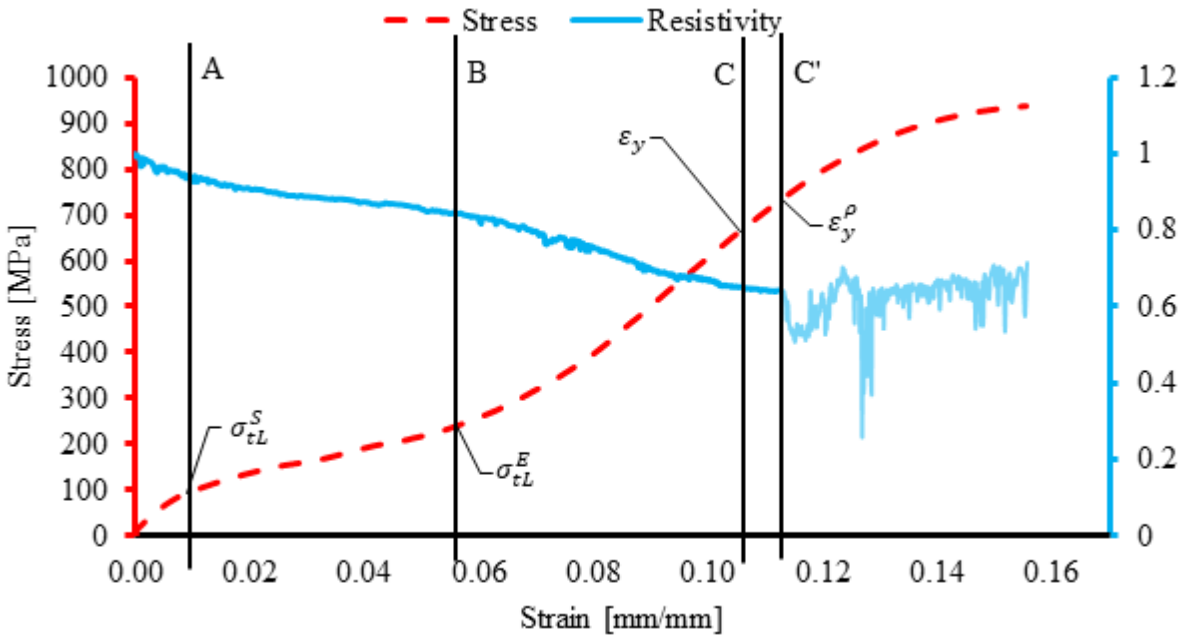

Figure 2.32 Representative Yield Stress-Strain-Resistivity Response of NiTiCu1

Another interesting result is that of normalized resistivity rate of change with respect to strain $\left(\frac{\delta\left(\frac{\rho}{\rho_0}\right)}{\delta\varepsilon}\right)$ – evaluated using a 6th order backwards difference – which is shown in Figure 2.33. The resistivity rate of change is constant within the plateau region between A and B, and noisy outside of this. This indicates that there is a 1st order dependency of phase on strain (i.e. $\rho = \rho_0 - \frac{\delta\rho}{\delta\varepsilon} * \varepsilon$) within the plateau region. The noisiness outside of these bounds indicates that other phenomena – such as instability of phase change due to micro-stress distribution – may influence measurements in these regions.

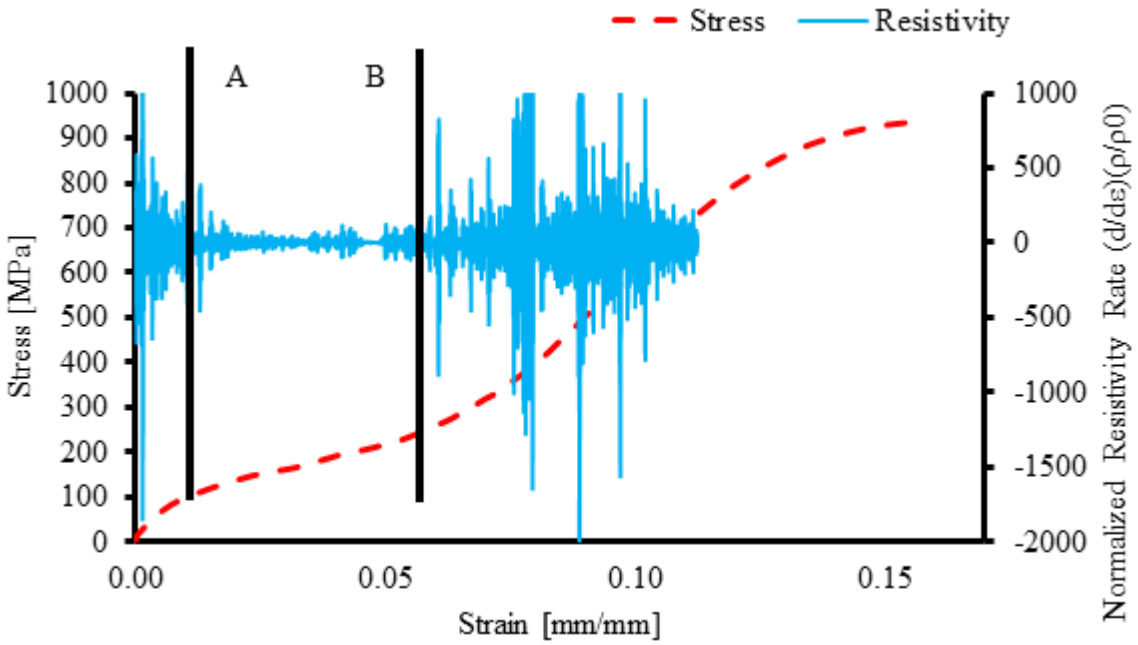

Figure 2.33 Resistivity Rate of Change with Respect to Strain for NiTiCu1

The unexpected resistivity vs. strain slope prior to A, shallowness from A to B, and steepness from B to C, in Figure 2.32 indicate that there is a more complex relationship between the micro-stress distribution and phase transformation than can be explained with the current state of the art. Given that the property being measured is resistance, it is possible that some geometric factors are not being accounted for in the calculation of resistivity. A notable assumption is the constant Poisson's Ratio, which though common is not widely recognized as valid (see [81] for an example of dynamic Poisson's Ratios). The corrected equation is Eqn. 2.12, here Poisson's ratio itself is a function of strain. The to calculate the dynamic resistivty ($\rho(\varepsilon)$) the values required are the are resistance (R); applied strain (ε); unstressed sample diameter (d_0) and length (L_0); and Poisson's ratio as a function of strain ($\nu(\varepsilon)$). Measurement of Poisson's Ratio for thin samples is not trivial (i.e. the 150 [mm] diameter wires used here) but is clearly an important avenue of future work. An analysis of rate using Figure 2.33 indicates that the result is more accurate within the plateau region (between A and B), and that outside of these bounds other factors must be further studied.

Eqn. 2.12. Dynamic Resistivity (Varied-Poisson's Ratio): $\rho(\varepsilon) = R * \frac{\pi * d_0^2}{4 * L_o} * \frac{(1-\nu(\varepsilon)*\varepsilon)^2}{(1+\varepsilon)}$

2.5.5. Functional Stabilization with Resistivity Measurements

Knowing that functional stabilization changes the phase distribution, it is interesting to investigate this behaviour with resistivity measurements. These tests are performed at 80 [^{o}C] on a TA Q800 DMA with a maximum force of 8 [N] and a controlled loading rate of 0.1 [N/min] for 550 cycles. Four tests were conducted, with a sample result is shown in Figure 2.34.

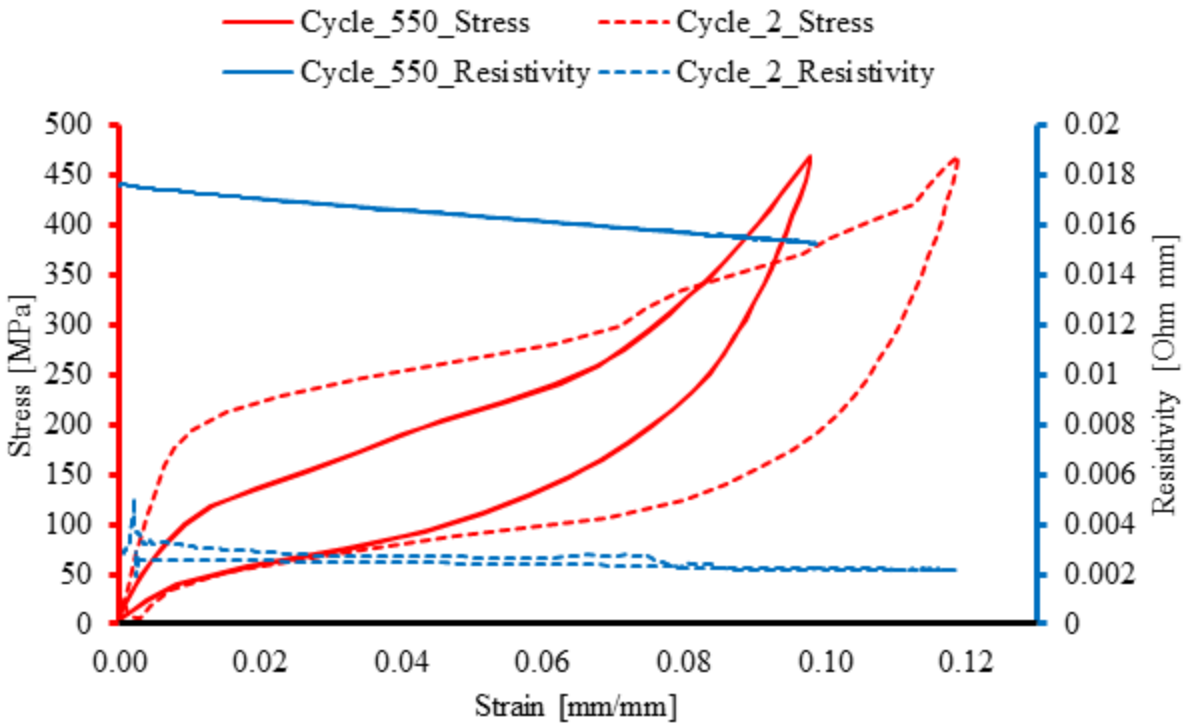

Figure 2.34 Functional Stabilization Stress-Strain-Resistivity Response for 2nd and 550th Cycles for NiTiCu1

There is a small hysteresis observed in the resistivity for the 2nd cycle, with no observable hysteresis for the 550th cycle. Given that resistivity is dictated by microstructure and not loading direction, resistivity measures phase transformation and that any hysteresis is indicative of a change in microstructure (i.e. TRIP) associated with loading cycle. Defects tend to increase resistivity in metals [84], so the increase in resistivity from 2nd to 550th cycle is expected.

Looking more closely at the 550th cycle, a very linear response is observed in Figure 2.35 – similar to that in Figure 2.32 – on both loading and unloading. Addressing at the rate of change of resistivity with respect to strain for once cycle in Figure 2.36, a similar trend is observed to that of Figure 2.33. There is significant noise at the beginning and end of the unloading cycles and little noise during the transformation region.

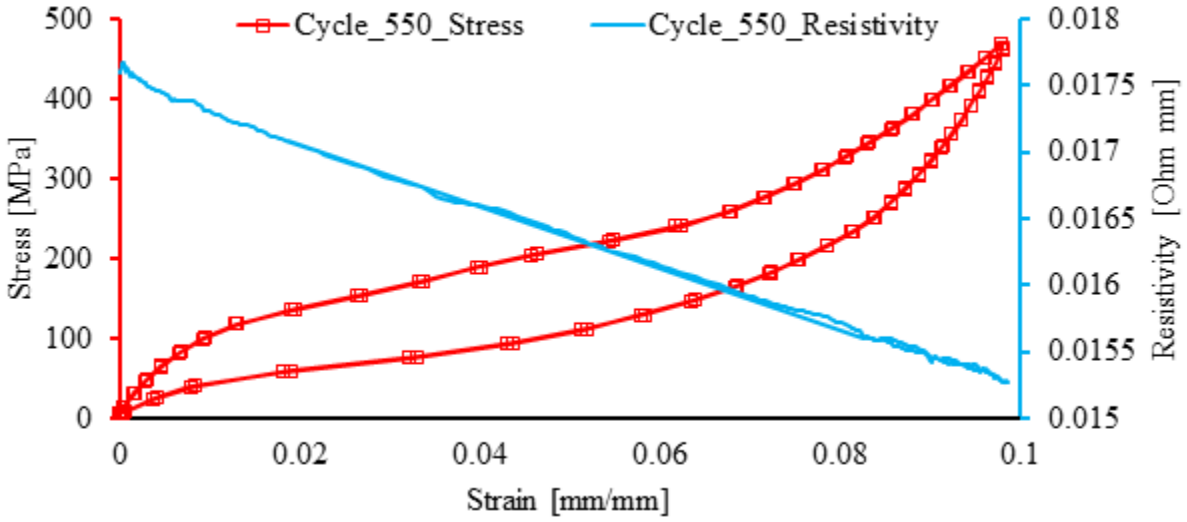

Figure 2.35 550th Cycle (Stabilized) Stress-Strain-Resistivity Response

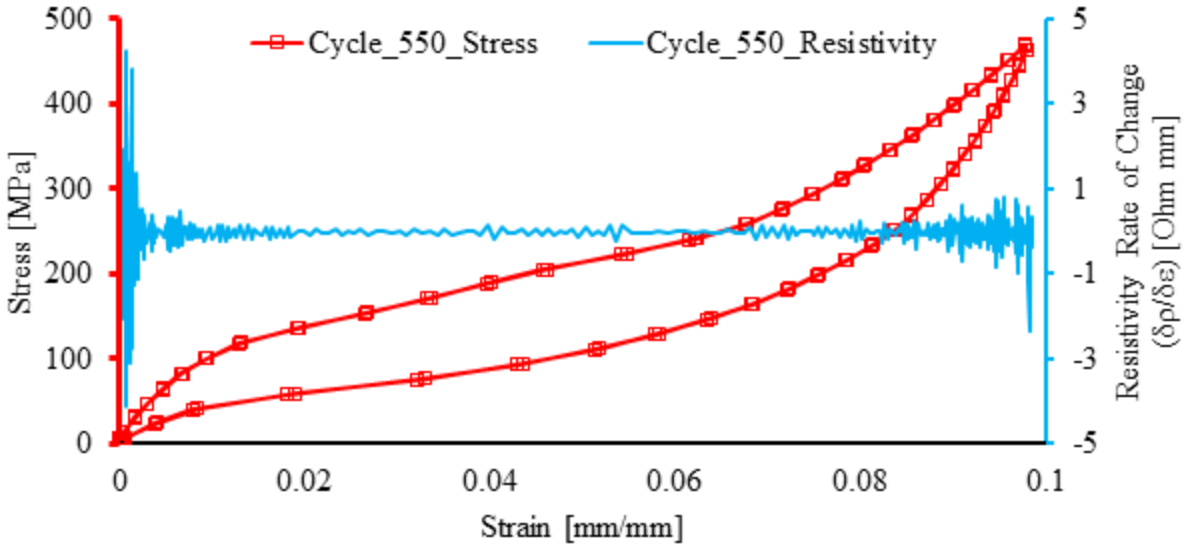

Figure 2.36 Stable Stress-Strain-Resistivity Loading-Unloading Cycle

2.5.6. Summary

A fixture was developed to perform coupled thermo-electro-mechanical characterization of shape memory wires using a TA DMA Q800, an NI DAQ system, and custom algorithms to synchronize the data. A method for calculating resistivity which accounts for both length changes due to strain and cross-sectional area changes due to Poisson's effect, was implemented. The functional stabilization results exhibit a resistivity hysteresis due to plastic dislocations in early cycles which does not appear as the sample becomes stabilized. The resistivity does not follow the expected behaviour – only changing in the plateau region – indicating a more complex relationship between phase transformation, functional stabilization, and the micro-stress distribution worthy of future work. It is also possible that the assumption that Poisson's Ratio is independent of strain is invalid, and that further work on characterization of Poisson's Ratio is necessary to interpret these measurements accurately. One potential avenue is molecular dynamics modelling of NiTi and NiTiCu alloys to provide insight into material properties and behaviours. Furthermore, the fixture should be updated to improve electrical contact and reduce the error in setting initial length of the sample, as measurements are sensitive to both these parameters.

While some observations are explicable with current understanding, significant future work is required to understand the correlation between phase change and resistivity of shape memory alloys. This work is key to developing sensor and control systems using shape memory alloys.

3. Finite Element Modelling of Hybrid Composites

In this section the state of the art of finite element modelling of SMA wire-fibre-thermoset composites is discussed. A new FE model is developed and used to investigate the effects of various design parameters which designers can readily control to achieve desired behaviours. SMA modelling in ABAQUS has been previously discussed in **Section 2.2**. Discussed herein are the tools available for FRP modelling in ABAQUS. From this, a method of combining the two for a SMAHC model is developed.

3.1. A Review on FEM of Hybrid Composites

Due to the nascency of commercial SMA modelling, SMAHC modelling is predominantly performed with proprietary algorithms and FE scripts, (see Lester et. Al. [10]). In this work, a method for SMAHC modelling which makes use of only commercially available tools, enabling for general application, is developed. Failure modes are not considered in this work.

Finite element packages, such as ANSYS [85] and ABAQUS [86] can model composites using micro- , macro- , or multi- scale approaches. Micro-scale approaches model the reinforcement and matrix discretely, while macro-scale approaches homogenize the reinforcement and matrix properties [86]. Multi-scale approaches are combinations thereof [86]. A common approach to modelling of composites is the modelling of discrete homogenized laminae which are then combined to model composite layup (referred to herein as the *Laminate Approach*), which is a multi-scale technique. The Laminate Approach studies inter- and intra- laminae properties without considering micro-scale behaviours. FRP lamina can be modelled using orthotropic plane-stress *linear* elastic properties [87]. Finite element material models for orthotropic plane-stress *non-linear* elasticity have been proposed [88] and implemented via custom scripts [10], [89], [90], but are not commercially available at the time of writing. Therefore, the macro-scale and the Laminate approaches cannot be used to model SMAHCs. There are other multi-scale approaches to SMAHC modelling, including continuum element methods presented by Lester et. Al. [10], the shell approach taken by Giuntoli [15] and Roh et. Al. [91], and lastly the beam approach taken by Lee & Lee [92]. Key concerns including computational power, verifiability, and compatibility with other tools in the finite-element software are addressed in this section.

3.2. Development of Finite Element Model for Hybrid Composites

In order to exhibit a bending response, shape memory alloys must be place off the neutral axis of a laminate, introducing unsymmetry. As a starting point, the response of unsymmetric fibre reinforced laminates is studied to gain an understanding of the linear effects. The integration of SMAs into the laminate is then discussed, and lastly a final model is proposed and evaluated.

3.2.1. Unsymmetric FRP Laminate Modelling

Analytic approaches with numeric solutions [20], [93]–[97], as well as finite-element [95], [96], [98], [99] approaches to modelling the cured room-temperature shapes of unsymmetric FRP laminates have been developed and validated experimentally. Schlecht et. Al. acknowledge the limitations of analytic approaches – termed Extended Classical Laminate Theory (ECLT) – accuracy regarding edge effects [95]. The forces which induce buckling or transformation between buckled states cannot be calculated using available analytic models [95]. Analytic models are also inconvenient to combine as there no generally accepted analytic models for SMAs. Therefore, finite element is the only approach worthy of further investigation.

Tawfik [98] presents validated approach to FE modelling of unsymmetric laminates which includes extensive comparison between FE simulation, ECLT, and experimentation on a wide variety of geometries and layups. Clearly demonstrated in this work is the improved accuracy of FE compared to ECLT. Included in Tawfik's FEM development is extensive element convergence testing. Of note are Tawfik's following claims for FE modelling for unsymmetric laminates:

- ABAQUS S4R shell elements provide enough accuracy and convergence when compared to higher order elements.
- Converged models based on ABAQUS S4R shell elements require similar computational time to ECLT and provide increased accuracy.
- Stable room temperature shapes can be created consistently through by introducing geometric imperfections based on a linear buckling approximation.
- The ABAQUS STATIC, STABILIZE step provides accurate results in terms of laminate geometry when force is applied, including the snap-through event.
- Geometry generated using ABAQUS STATIC, STABILIZE is valid for further static analysis steps.

Given demonstrated accuracy benefit of using an FE approach over ECLT, Tawfik's FE approach will be used to model unsymmetric laminates.

A notable extension of Tawfik's work is that of Portela [99], which includes hygroscopic compensation by varying the coefficients of thermal expansion. This is omitted from the analysis because of the lack of experimental data but could be easily integrated if it was available.

3.2.2. Test Case Replication

The first step taken to check this model is replicating the test case presented by Tawfik. This is done by simulating similar material properties and geometries. The material used is a Hexcel IM7 and 8551-7 graphite and epoxy prepreg, whose properties are presented in Table 3.1.

Table 3.1 Test Case Material (Hexcel IM7 and 8551-7) Properties [98], [100]

E_{11} [GPa]	E_{22} [GPa]	G_{12} [GPa]	G_{13} [GPa]	G_{23} [GPa]	ν_{12}
141.18	7.20	4.45	4.45	3.30	0.341

α_1 $[\mu m/_{m*K}]$	α_2 $[\mu m/_{m*K}]$	α_3 $[\mu m/_{m*K}]$	t [mm]
0.14	30.98	30.98	138.75

The simulation and geometry parameters used to replicate Tawfik's test case are listed in Table 3.2. See Figure 3.1 for the geometric representation. The square plate presents a worst-case test for unsymmetric laminates due to their geometric symmetry. Less accurate simulation approaches will readily yield inaccurate cured shapes (saddle rather than cylindrical) which are not in agreement with either ECLT or experimental results [98]. The model is created using S4R shell elements, with a fixed boundary condition at the centre node. The panel is thermally loaded by cooling from gelation to room temperature.

Table 3.2 Test Case Parameters [98]

Side Length (A) [mm]	150
Gelation Temperature (T_{Gel}) [^oC]	177
Room Temperature (T_{Room}) [^oC]	21
Layup	$[0_2/90_2]_T$
Boundary Condition	Fixed Centre Node
Mesh Dimensions	20 x 20
Element Type	S4R

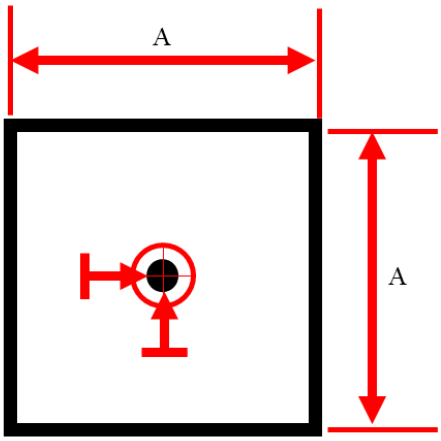

Figure 3.1 Test Case Geometry

Panel curvature is measured using the same geometric approach as Tawfik, which is shown in Figure 3.2 and Eqn. 3.1, for purposes of similar comparison. The depth of the arc (d) and the width of the arc between end points (C) are used to calculate the panel curvature when the radius (R) is unknown. However, this approach only captures a limited picture of the panel, as curvature is non-uniform due to edge effects. A mean value theorem (MVT) approach is taken to calculate an area-weighted (AW) average curvature (κ^{AW}, shown in Eqn. 3.2) as it captures the cumulative curvature of the section. Parameters $\kappa_{i,e}$ and A_e, which respectively represent the element surface area and curvature are used to calculate the area weighted panel curvature.

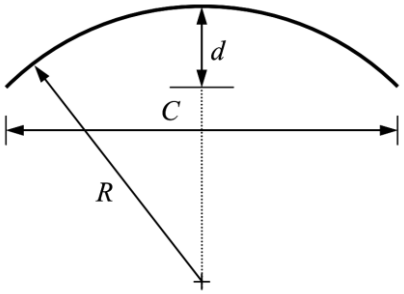

Eqn. 3.1. Curvature: $\kappa = \frac{1}{R} = \frac{8d}{C^2+4d^2}$

Eqn. 3.2. Area Weighted Curvature:

$$\kappa_i^{AW} = \frac{\sum_{e=1}^{\infty} \kappa_{i,e} * A_e}{\sum_{e=1}^{\infty} A_e}$$

Figure 3.2 Curvature Measurement[2]

[2] As a visualization aid, the curvature of a soda can is approximately 30 [m^{-1}] or 0.030 [mm^{-1}]

All temperatures are expressed as *Relative Temperature*, as in Eqn. 3.3. The temperature at which the panel takes on one of the two equilibrium shapes is referred to as the *Bifurcation Point Relative Temperature*, which is calculated as in Eqn. 3.4.

Eqn. 3.3. Relative Temperature: $T_{Relative} = T - T_{Room}$

Eqn. 3.4. Bifurcation Point Relative Temperature: $T_{Bifurcation,Relative} = T_{Bifurfaction} - T_{Room}$

The results of the test case are presented in Table 3.3. There is good agreement of equilibrium shape curvatures, indicating the approach has been accurately replicated. Notably, the area weighted approach measures an larger curvatures as it captures the high of curvature at the edges. The differences bifurcation point relative temperature are discussed further in **Section 3.2.3**.

Table 3.3 Test Case Results

		Curvature (κ_x) [m^{-1}]		Bifurcation Point Relative Temperature [^oC]
		1st Equilibrium	2nd Equilibrium	
Simulation	Geometric	5.93	0.02	145.39
	Area Weighted	5.81	0.06	
Tawfik [98]		5.96	0.02	141.16

3.2.3. Mesh Convergence Testing

Tawfik uses bifurcation point relative temperature and curvature to evaluate the convergence of his model. Curvature only evaluates the model at the endpoint, with no reference to the region of instability, leading it to be less useful as a convergence parameter for evaluating the snap-through region. There is a 4 [^{o}C] discrepancy in the bifurcation point relative temperature between this simulation and Tawfik's, which is attributed to the fact that bifurcation does not occur at a "point" in the finite element analysis, but rather over a range. Shown in Figure 3.3 is the curvature vs. relative temperature in the bifurcation region for a range of mesh sizes. First, it is clear that bifurcation does not occur at a discrete temperature as presented in Tawfik's work, but over a range, making it difficult to evaluate. Secondly, there is no clear trend relative to mesh size. Since bifurcation temperature cannot be evaluated at a discrete temperature and no trend is observed with mesh size, it is deemed a poor indicator of convergence and another variable must be used.

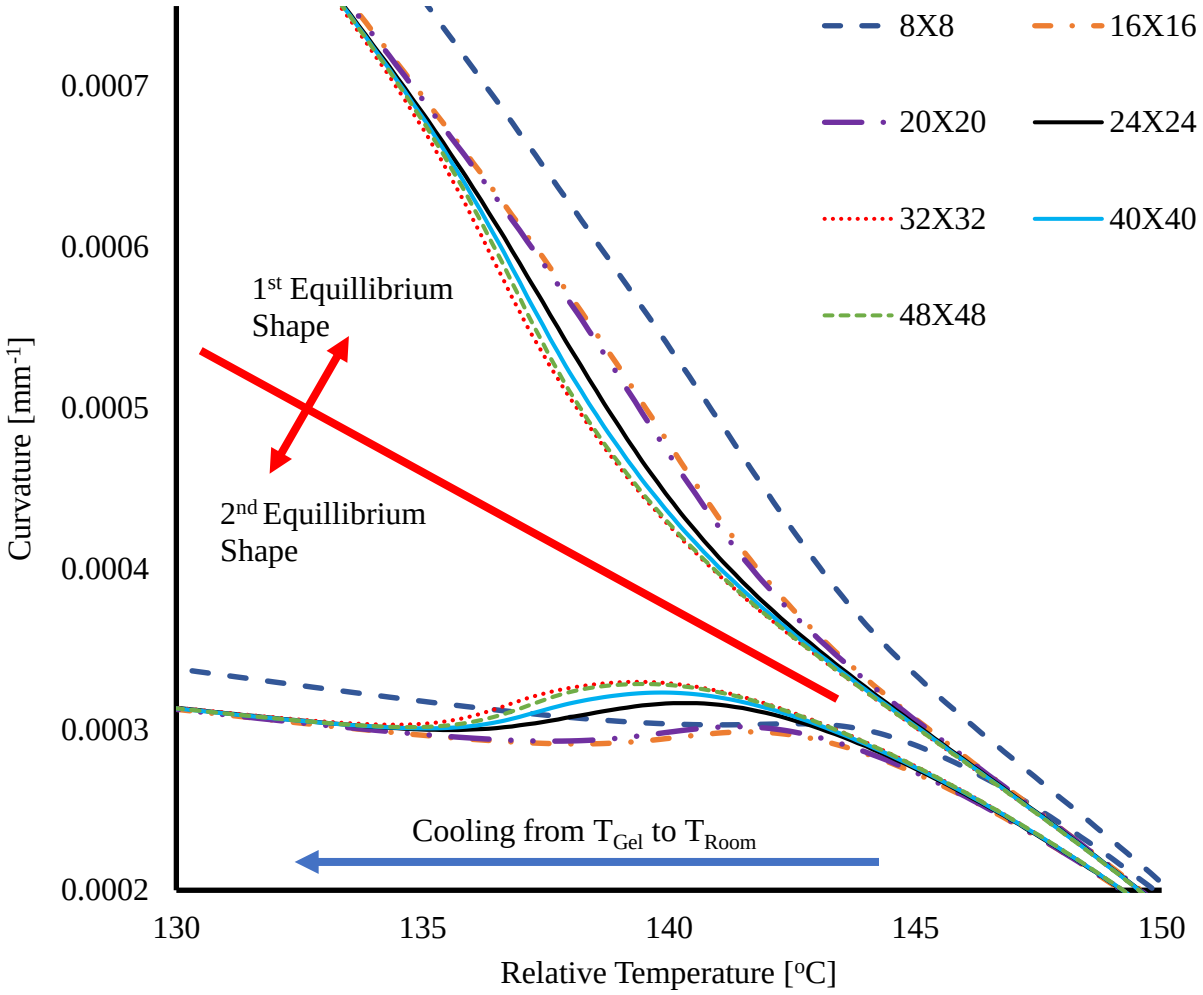

Figure 3.3 Curvature vs. Relative Temperature in the Bifurcation Region for Various Mesh Sizes

Another parameter considered for convergence is *Snap Through Force*. An example of which is shown in Figure 3.4 for the same 150x150 [mm] panel with meshes ranging from 16 to 104 elements per edge. The snap through force is measured during a highly non-linear region of the analysis and stabilizes as the mesh density is increased, indicating that it makes for a more suitable convergence parameter than curvature or bifurcation temperature for this study.

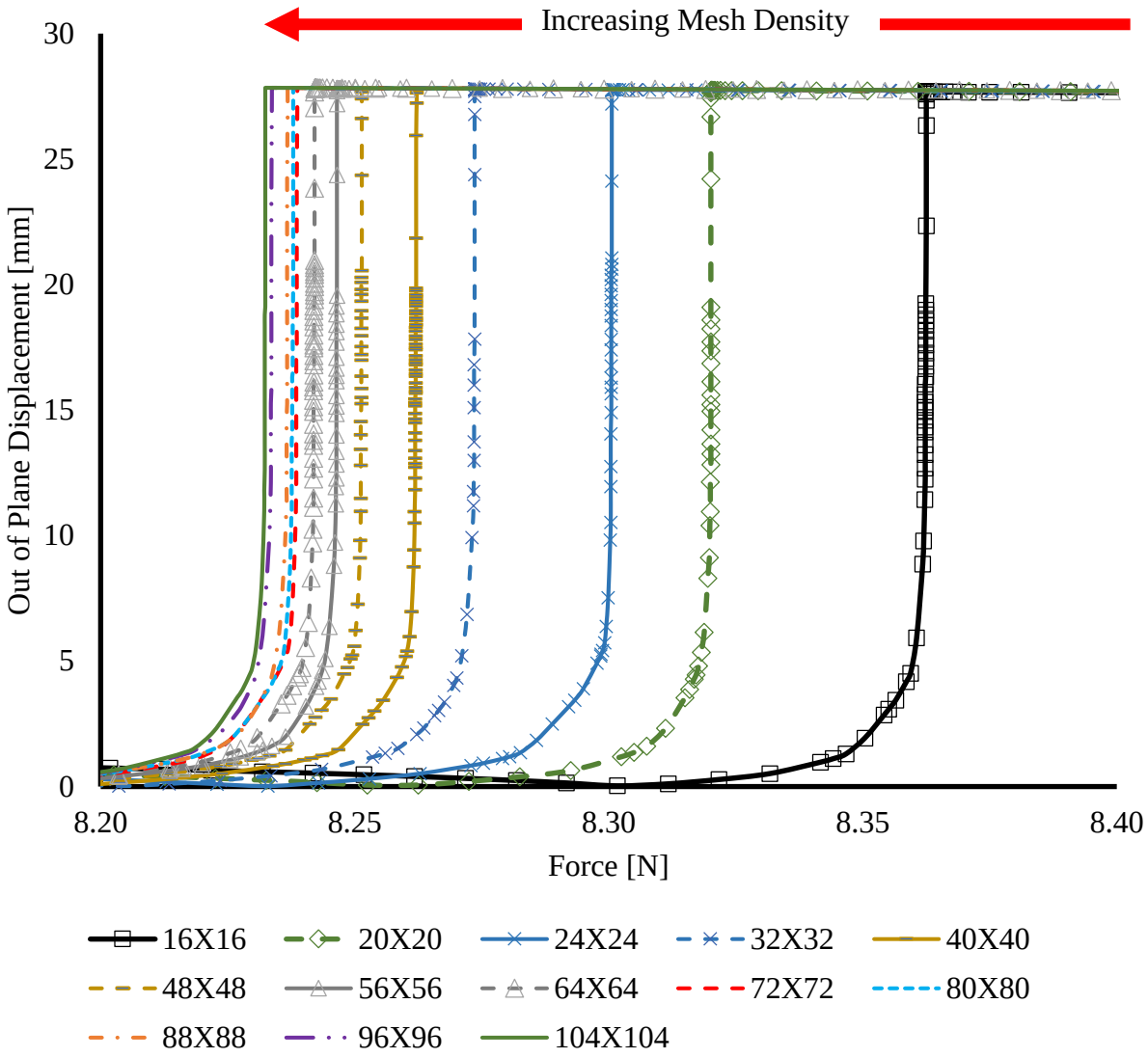

Figure 3.4 Out-of-Plane Displacement vs. Snap Through Force

A large discontinuity is observed when the snap through force is reached, indicating a rapid rate of change in the first derivative of displacement with respect to force, shown in Figure 3.5. The snap through force (F_{Snap}) can be specified as being at the point where this derivative is at a maximum (Eqn. 3.5).

Eqn. 3.5. Definition of Snap Through Force: $F_{Snap} = F|_{\max\left(\left(\frac{d}{dF}\right)Out\ of\ Plane\ Displacement\right)}$

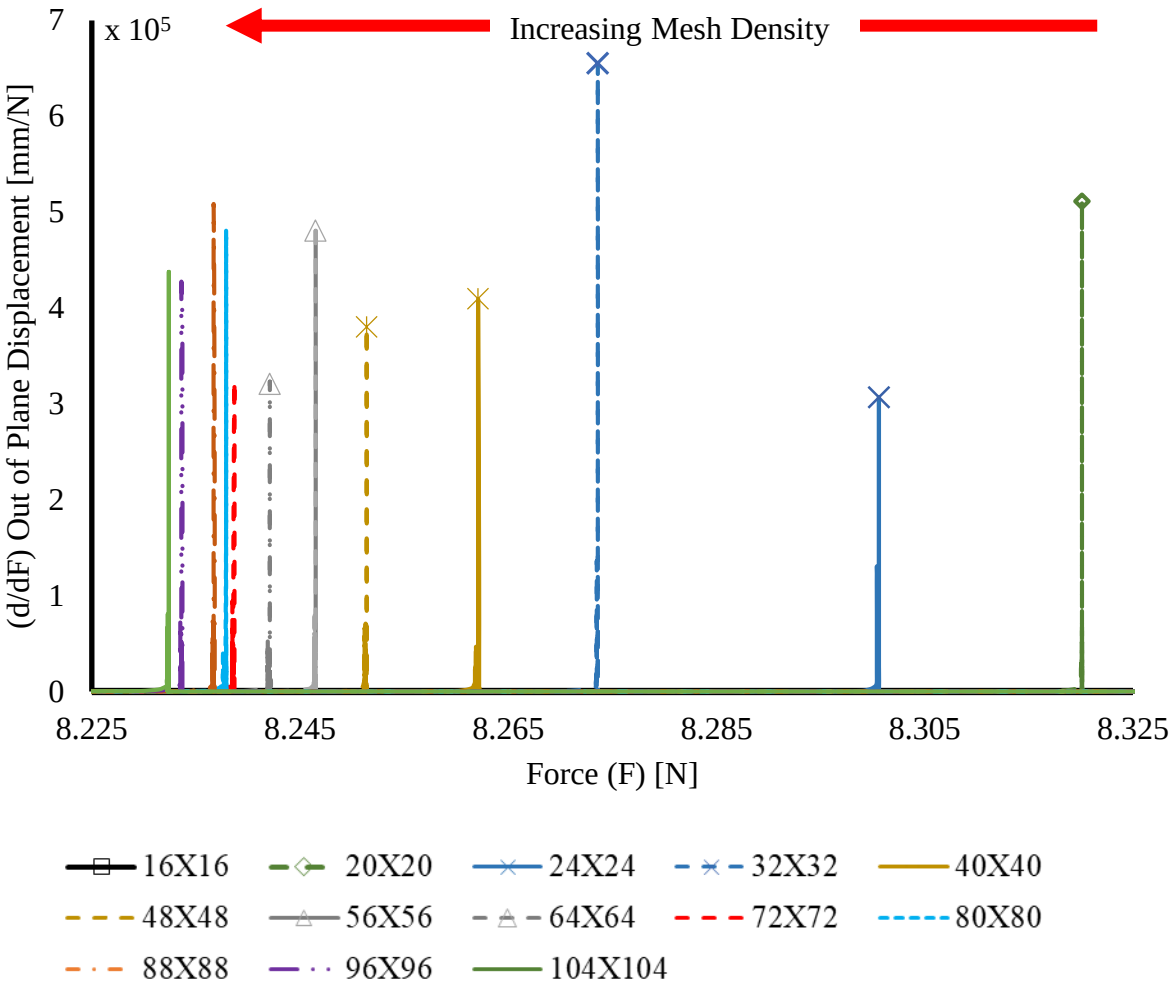

Figure 3.5 First-Derivative of Displacement vs. Force

To study convergence, snap through force is compared to the degrees of freedom in Figure 3.6. There is not significant variation in these results, with 1 [%] variation in snap through force between the 20x20 mesh ($10^{3.4}$ [DoF]) and the 104x104 (densest) mesh. This confirms Tawfik's finding that a mesh where the element edge length is 5 [%] of the part edge length is sufficiently fine for modelling of bistable laminates.

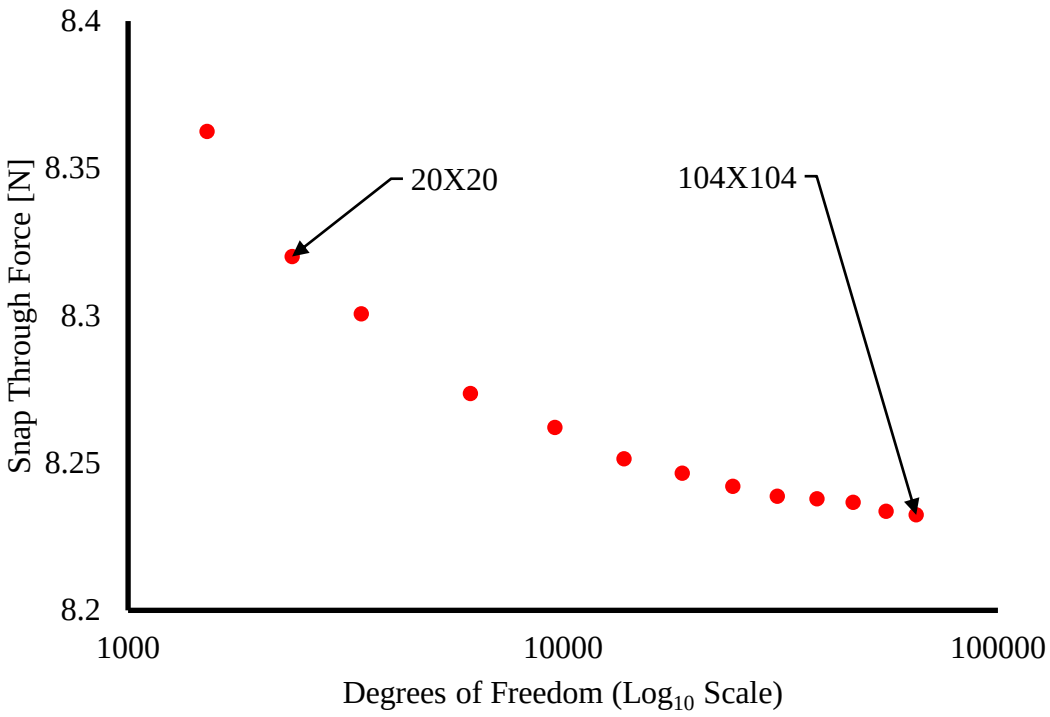

Figure 3.6 Snap Through Force vs. Degrees of Freedom

It is shown that snap through force makes a good convergence parameter as it can be discretely measured in the non-linear region of the analysis. It is shown that force stabilizes within 1 [%] when S4R elements whose edge length is 5 [%] of the edge length is used to mesh the part. This mesh density or greater will be used to model all laminates in the remainder of this work.

3.2.4. Finite Element Modelling of Hybrid Composites

There are two key concerns in developing the SMAHC model. The first of which is prestraining[3] SMA wires independently from the FRP structure. The second of which is addressing the non-linear plane stress orthotropic elasticity of SMA lamina.

3.2.4.1. SMAHC Prestraining

Prestraining of SMA wires enables force exertion through the stress-strain-temperature coupling of superelasticity, thereby enabling morphing composite structures. Thus, it is a key aspect of SMAHC modelling. It's discussed first as it limits options available for subsequent considerations.

Prestraining of SMAs in SMAHCs presents a modelling challenge which can be illustrated using a simple two element wire fixed on both ends with nodes in the centre (Figure 3.7). Assembly length (L_{Asm}) is a fixed geometric property, such as the length of a SMAHC panel.

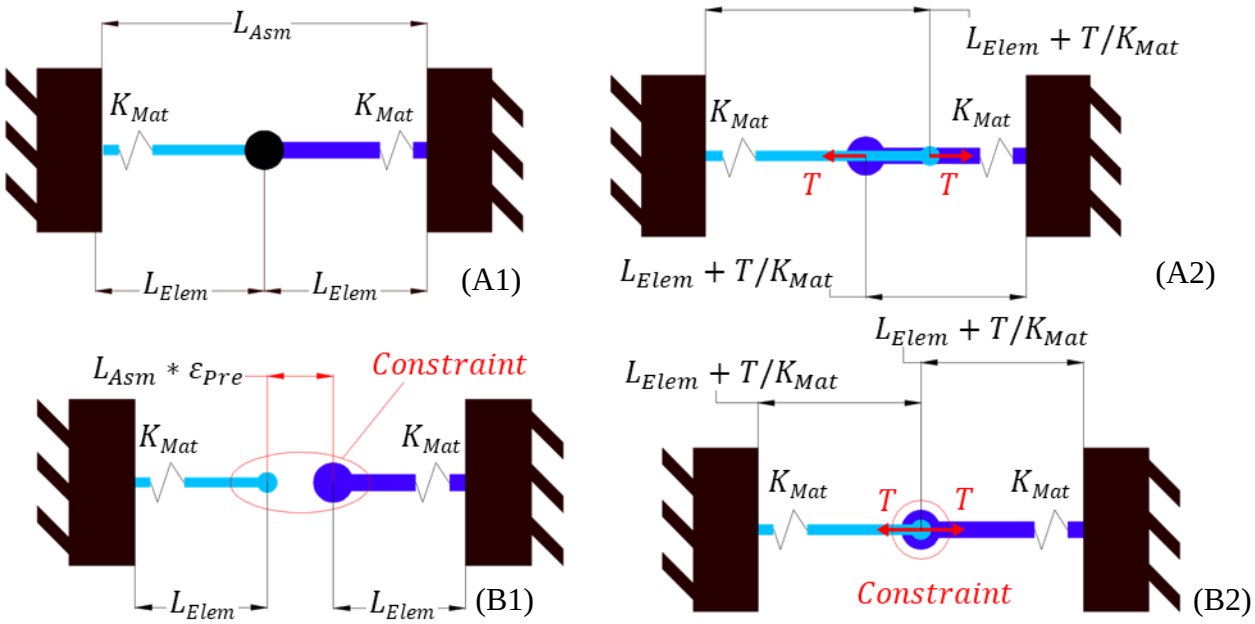

Figure 3.7 Diagrams showing unstrained geometric (A1), separately pre-loaded (A2) and modified mesh geometric (B1), and modified mesh pre-tensioned (B2) model states

[3] *Prestrain* refers to the SMA wire strain prior to integration in the composite. Since strain is insensitive to temperature and is controllable manufacturing, it is used as the reference. *Preload* refers to any force- or stress-based phenomena related to this strain, which are not independently controllable and dependent on temperature for SMAs.

The initial meshed condition where $L_{Elem} = L_{Asm}/2$ and the elements share a node is shown in (A1). To apply a tensile force, the nodes must be separated, and preload force applied to a node on each element (B). Separating the nodes allows them to cross through each other in a non-physical manner called *overclosure* [101], which is clearly inaccurate (A2).

Solving this problem is challenging. For example, Autodesk, as of 2017, only supports prestrain of fixed-sliding beam elements [102] or prestrain of solids using CTE [103], neither of which is suitable for this model. Another approach is to geometrically separate the nodes to which a tensile force is applied and apply some form of constraint [104] or element [105], [106] to tie the nodes together (B1). The two nodes are then brought together to apply the prestrain (B2) [104]. These types of adjustments are referred to as *mesh modification methods*. Hibbitt & Nagtegaal [104] state that these methods reduce mesh clarity and don't solve overclosure.

One method available in ABAQUS to apply a preload, developed by Hibbitt & Nagtegaal [104], differs significantly from aforementioned methods. Hibbitt & Nagtegaal propose a method which applies the prestrain by adding a constant-offset term to one or more of the element stiffness matrices. For detailed insight into this approach, it is recommended that the reader reads reference [104]. Of course, this deforms the mesh geometrically too. However, the node continues to be shared between mating elements, thereby preventing overclosure while applying the preload or prestrain. Theoretically this method can be applied to any element type [104], but in practice ABAQUS only allows it's use with beam and continuum elements [107]. This limits the modelling of the SMA-epoxy lamina(e) to being done either with continuum or beam elements.

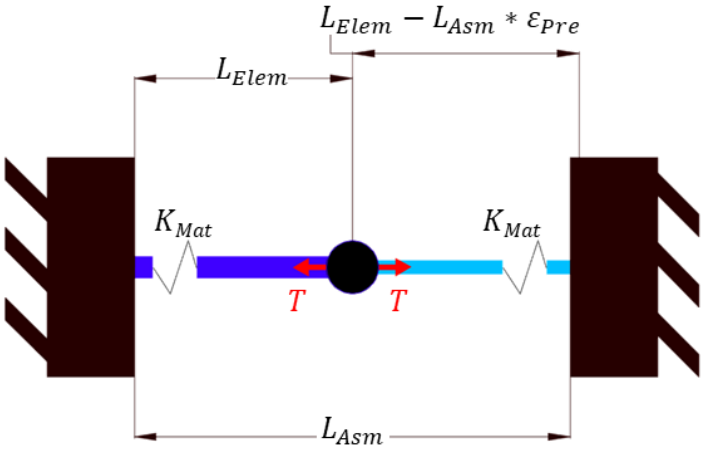

Figure 3.8 Hibbitt & Nagtegaal [104] Prestrain Method

To apply a prestrain using Hibbitt & Nagtegaal's approach in ABAQUS requires the user to input the desired length of the updated element, as calculated in Eqn. 3.6.

Eqn. 3.6. Preload Length: $L_{Pre} = L_0 * (1 - \varepsilon_{Pre})$

To summarize, the Hibbitt & Nagtegaal's approach to element prestraining is used as it prevents overclosure problems and maintains mesh clarity. In doing so, however, the options for modelling the SMA-epoxy lamina(e) are limited to the use of beam and continuum solid elements.

3.2.4.2. SMA-Epoxy Lamina Plane-Stress Orthotropy

Both continuum and beam element based meshes are considered for modelling of the SMA. Continuum solid elements can clearly be used to represent the problem accurately using micro-scale modelling. They are, however, computationally intensive due to the large aspect ratios that need to be modelled ($Wire\ Length/Wire\ Diameter > 10^4$). Therefore, the suitability of beam elements to this problem should be evaluated in the interest of computational efficiency. While the SMAHC beam element model has been proposed before by Lee & Lee [92], no discussion of assumptions was provided and the work makes use of a UMAT for the SMA constitutive model.

First, it's useful to describe how such a problem could be meshed. If the problem was represented using continuum solid elements Figure 3.9, the SMA (orange) and epoxy (grey) regions would be meshed with continuum solid elements with some sort of interaction (cohesive, tie, or otherwise) applied at the nodes at the interface (red).

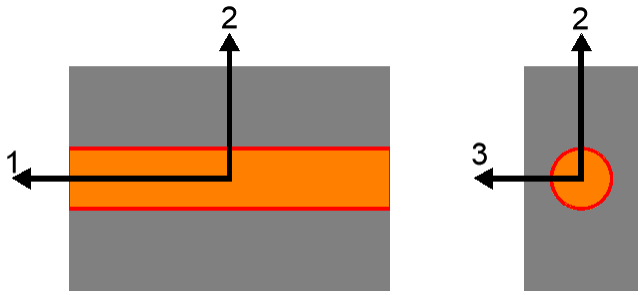

Figure 3.9 SMA-Epoxy Lamina Continuum Mesh Representation

Were the problem to be meshed with beam elements (Figure 3.10) for the SMA (orange), the SMA beam would cross the epoxy section (grey) and be constrained at nodes using tie-constraints (red). The epoxy section could be meshed using any element type in this case, so long as there are nodes available at the tie-constraint locations. The issue with this method is that it ignores the SMA

interfaces with the epoxy layer. This includes stress generated by thermal expansion and Poisson's Ratio differences as well as relative movement between the SMA and matrix, while failure modes are not considered, some assumptions must be made to model the desired behaviour.

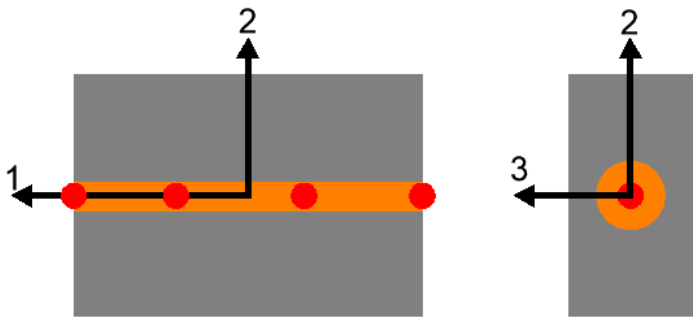

Figure 3.10 SMA-Epoxy Lamina Beam Mesh Representation

The first assumption, that *micromechanical behaviour has negligible effects on macromechanical behaviour*, means that Poisson's effect and interfacial stress distribution will not be included in the study. This assumption is made in Birman et. Al.'s [88] non-linear lamina multicell modelling approach which was validated by Cho and Rhee [90], indicating that these assumptions are accurate and can be built upon.

The validity of the assumption that *interfacial stresses caused by thermal expansion are negligible* is less clear because the matrix and SMA coefficients of thermal expansion (α_M and α_{SMA} respectively) differ by about a factor of four [88] and the temperature changes are significant as the system is thermally cured and actuated. The differences in elastic modulus and Poisson's ratios of matrix and SMA will also affect this assumption (E_{Mat}, v_{Mat}, E_{SMA} and v_{SMA} respectively). The radii of the SMA wire (R_{SMA}) as well as the surrounding matrix layer (R_o) factor into the solution as well. This problem can be represented using Blosser's model (Eqn. 3.7) [108], which uses a concentric cylinder approach that allows for expansion around a fixed geometric centre (Figure 3.11), thereby enabling a quantitative investigation into validity.

Eqn. 3.7. Blosser's Model: $$\sigma_{int} = \frac{E_m\left[\left(\frac{R_O}{R_{SMA}}\right)^2 - 1\right](\alpha_{SMA} - \alpha_m)}{\left(\frac{R_O}{R_{SMA}}\right)^2 (1+v_{Mat}) + (1-v_{Mat}) + \left(\frac{E_{Mat}}{E_{SMA}}\right)\left(\left(\frac{R_O}{R_{SMA}}\right)^2 - 1\right)(1-v_{SMA})} \Delta T$$ [108]

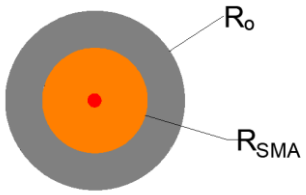

Figure 3.11 SMA-Epoxy Lamina Geometric Representation of SMA Diameter (R_{SMA}) and Matrix Diameter (R_o) used for Blosser's Model (Eqn. 3.7)

Where the temperature difference Eqn. 3.8 is defined with respect to the cure cycle. The gelation temperature (T_{Gel}) is the zero-stress state in the matrix, so it serves as the reference:

Eqn. 3.8. $$\Delta T = T_{Gel} - T$$

This expression uses a *tension-positive* convention, where the operating temperature is *below* the matrix gelation will cause the matrix to pull radially outwards on the SMA. In practice, this may cause debonding. However, this analysis assumes maintenance of intimate contact and thus failure modes, such as debonding, is not assessed. Assuming intimate contact, the results are symmetric, so in the cases where operating temperature is above gelation temperature the negative (compressive) stress is applied to the wire.

To estimate the effect of the interfacial stress (σ_{int}), a wire element state-of-stress on is studied (shown in Figure 3.12). With the Poisson's ratio (ν_{SMA}) and preload stress (σ_{Pre}) included, the available actuation stress (σ_{Act}) can be calculated using Eqn. 3.9.

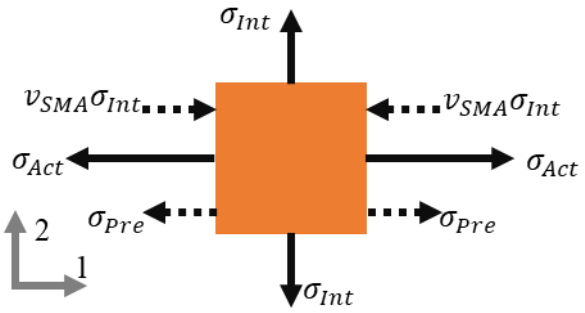

Figure 3.12 SMA Wire Element State of Stress to Calculate Available Actuation Stress (σ_{Act})

Eqn. 3.9. Actuation Stress: $$\sigma_{Act}(T) = \sigma_{Pre}(\varepsilon_{pre}, T) - \nu_{SMA}\sigma_{int}(T)$$

Based on Eqn. 3.9, it is possible to investigate the significance of Poisson's stress ($v_{SMA}\sigma_{int}$) on the available actuation stress (σ_{Act}). The Poisson's stress is plotted as a function of radius ratio and temperature using Blosser's model in Figure 3.13 to estimate the effects. This result is based on material properties from Birman et. Al. [88] and a radius ratio of $0.5 \leq \frac{R_o}{R_{SMA}} \leq 1$, representing matrix thicknesses that are between one- and four- times the SMA wire diameter.

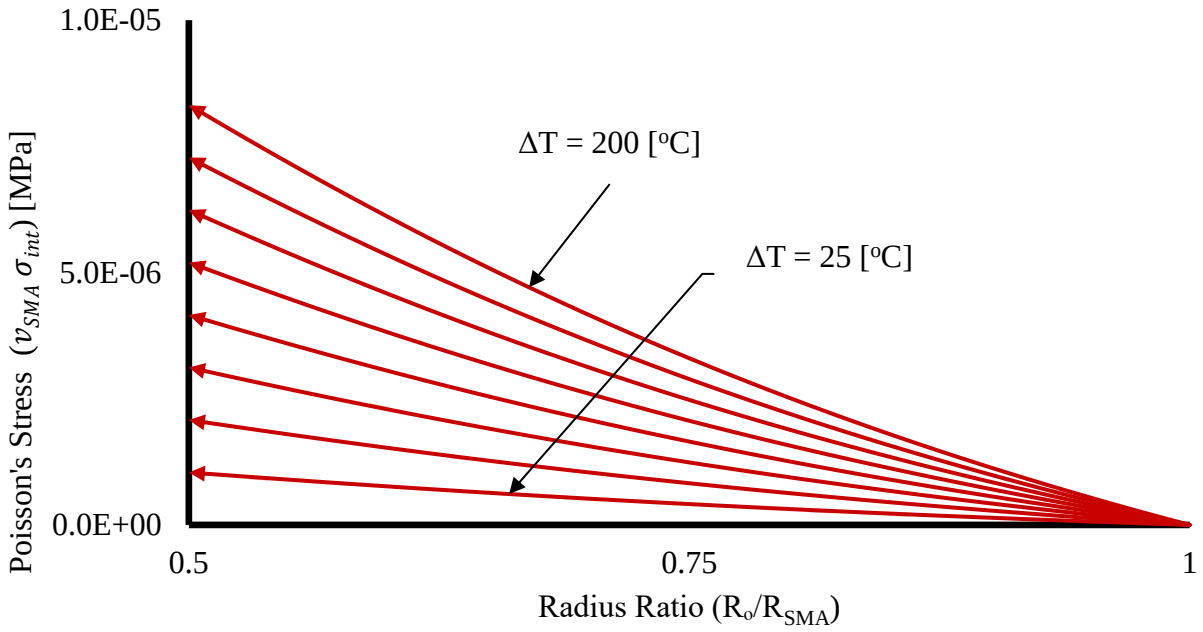

Figure 3.13 Poisson's Stress as a Function of Radius Ratio and Temperature in 25 [°C] Increments

For an example case to assess validity, the following limits are used:

- A preload stress of: $\sigma_{Pre}|_{T=80\,[^oC]}^{\varepsilon_{Pre}=25\,[m\varepsilon]} = 136\ [\text{MPa}] > \sigma_{tL}^{S}(T)|_{T_0}$
- A temperature range bounded by the processing and service limits of Hexcel 8551-7 and IM7 prepreg [109] and liquid salt water for sailing (0 [°C]): $84 \leq \Delta T \leq 177$ [°C]
- A radius ratio of: $\frac{R_o}{R_{SMA}} = 0.5$

In this case, $v_{SMA}\sigma_{int}(T) = 8.32\ [Pa]$, corresponding to a 0.006 [%] contribution to available actuation stress. Due to symmetry of the problem in tension and compression, a case where ΔT < 0 [°C] would yield similarly insignificant effects.

Furthermore, Kirkby [110] shows that the SMA-Epoxy interface can support a shear stress on the order of [MPa]. Since heating will only generate stresses on the order of [Pa], it can be said that the interfacial stresses due to heating are insignificant compared to other loads (such as prestrain). This confirms the applicability of Blosser's model in developing this assumption. The assumption that *differences in thermal expansion are negligible* is valid and will have insignificant effects on SMAHC behaviour in terms of actuation force and does not affect the interfacial strength.

Heat transfer between the SMA and CFRP laminate is not considered. The SMAs have a much smaller mass than the laminate. For simplicity, it is assumed that the relative thermal mass will cause the laminate to follow the ambient temperature and the SMAs to be heated independently.

3.2.4.3. SMA Element Selection

The beam-element approach is demonstrated to be appropriate for SMAHC modelling. This leaves the final step of selecting a suitable beam element. Of course, a discussion point is whether to use Euler-Bernoulli or Timoshenko beam theory. In terms of diameter-to-length ratios, ABAQUS documentation recommends Timoshenko for $\frac{L}{D} \geq 8$ and Euler-Bernoilli for $\frac{L}{D} \geq 15$ [111]. The length of a beam (L) is the distance between supports or loads, which in this case means the length of one element which models the CFRP to which the SMA beam element is tied (see Figure 3.15). Using a Timoshenko beam is then advantageous as it allows for finer meshes, shorter wire segments, and smaller systems to be modelled since wire diameter is fixed at 0.15 [mm] [112]. However, a linear isotropic shear stiffness is assumed for Timoshenko beams [111], the validity of which should be discussed. Timoshenko beam theory is applied to SMA modelling in ABAQUS using B31 elements by [32] and [113], who don't discuss how they managed this problem. Shear stiffness is an additional material property required from the user [111], calculated as:

Eqn. 3.10. $\boldsymbol{Shear\ Stiffness}: K = kGA_X$ [111]

where:

$$Shear\ Factor\ (k)\ is\ from\ Cowper\ [114]$$

$$Cross\ Sectional\ Area\ of\ Wire\ (A_X)\ is: A_X = \pi r^2$$

$$Shear\ Modulus\ (G)\ of\ an\ Isotropic\ Material\ is: G = \frac{E(\varepsilon,T)}{2(1+v)}\ [115]$$

Thus, for isotropic SMA wires:

Eqn. 3.11. Shear Stiffness of Isotropic SMA Wire

$$K(\varepsilon,T) = \frac{k\pi r^2}{2(1+v)} E(\varepsilon,T)$$

For SMAs, the elastic moduli ($E(\varepsilon,T)$) can vary by orders-of-magnitude depending on thermomechanical state. Given that ABAQUS does not allow for transverse superelasticity in Timoshenko theory, the representative linear elastic modulus should be carefully selected.

Transverse loading of a composite can be studied using stress equilibrium according to the orientation in Figure 3.14. Stress compatibility (Eqn. 3.12) defines the transverse behaviour of the

composite. This is then rewritten in terms of strain and evaluated using the material properties from Birman et. Al. [88] in Eqn. 3.13 to estimate the transverse strain ratio.

Eqn. 3.12. Transverse Stress Compatibility

$$\sigma_2^m = \sigma_2^{SMA}$$
$$\rightarrow E^m \varepsilon_2^m = E^{SMA} \varepsilon_2^{SMA}$$

Eqn. 3.13. Approximated Interface Strain Ratio

$$\boldsymbol{\varepsilon_2^{SMA} \approx 0.1 \varepsilon_2^m}$$

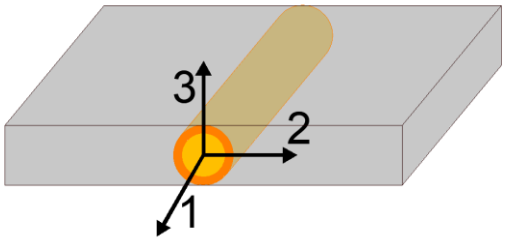

Figure 3.14 Orientation Definition of SMA Wire in Epoxy

The maximum strain sustainable in the transverse directions (2 and 3) is the yield strain of the matrix, which is 44 [mε] for neat 8551-7 epoxy [109], the corresponding SMA strain is 4.4 [mε]. This means the SMA will remain within austenite's linear elastic range when $T \geq A_f$ in the transverse direction, and Timoshenko theory can be used.

In cases of geometric non-linearity, ABAQUS recommends a *hybrid formulation* element [111]. Considering this, the *B31H* element is selected for this analysis. This element uses a hybrid formulation, Timoshenko beam theory, and linear interpolation [111]. The shear stiffness for this beam will be calculated as:

Eqn. 3.14. Timoshenko Beam Shear Stiffness

$$K = \frac{k\pi r^2}{2(1+v)} E^{Austenite}$$

3.2.4.4. SMAHC Model Development Summary

Before discussing the exact implementation of the SMAHC model components, the discussion thus far should be summarized. First, the Hibbitt & Nagtegall approach is used to apply prestrain by modifying select elements' stiffness matrices. Second, the beam-approach is selected as the assumptions that *micromechanical elastic behaviour has negligible effects on macro-mechanical elastic behaviour* and *interfacial stresses caused by thermal expansion are negligible* are shown to be valid. Lastly, a linear approximation of transverse stiffness is shown to be suitable for SMAHC modelling, thereby allowing the use of Timoshenko theory and the B31H element.

3.2.5. Proposed Modelling Approach

Presented in this section is an outline of how the SMAHC model is built using the tools and assumptions previously discussed, as well as a discussion of expected limitations. A unit-cell of the proposed SMAHC laminate model is shown in Figure 3.15. The FRP substrate is modelled with S4R elements (grey elements with black edges and nodes). The SMA is modelled using B31H elements (orange lines with orange nodes). At joints between the SMA and FRP, kinematic coupling constraints are placed (red). To allow for the prestrain of SMA wires, there must be at least three SMA elements between pairs of tied nodes. The SMA element to which prestrain is applied is shown in purple.

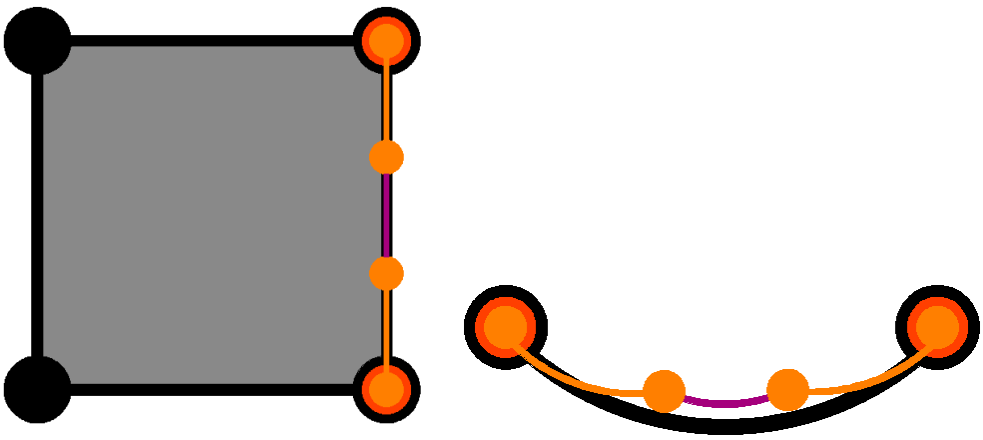

Figure 3.15 (A) Unit Cell of SMAHC Laminate and (B) Relative Displacement of SMA & FRP Elements in Bending, with the S4R Shell in Grey with Black Nodes, B31H Beam in Orange, Prestrained B31H Beam in Purple, and Kinematic Coupling Constraints in Red

The kinematic coupling constraints constrain all six translational and rotational degrees of freedom (DoFs) for the nodes pairs to which they are applied. However, edges between these nodes are free to move independently – a limit imposed by the use of the prestrain algorithm. Therefore, there will be a relative displacement between the shell and beam elements Figure 3.15. The more SMA elements per FRP element, the more relative movement will be possible, so there is need to minimize this element ratio (defined below) while ensuring sufficient mesh density for convergence. An element ratio (Eqn. 3.15) of one is ideal, as this would force the SMA element to follow exactly the FRP element, however the prestraining method requires that $R_{elem} \geq 3$.

Eqn. 3.15. Element Ratio: $R_{elem} = \frac{\#\ SMA\ Elements}{FRP\ Element\ Edges} \geq 3$

3.2.5.2. SMAHC Model Layout

As the simplified elements abstract the model from its physical representation, visualizing the desired model setup is critical. First, to repeat the coordinate axes of the system, as shown in Figure 3.16. The laminate's 1st axis is aligned with the SMA against which the ply angle (θ) is referenced. All plies are defined within the same shell element.

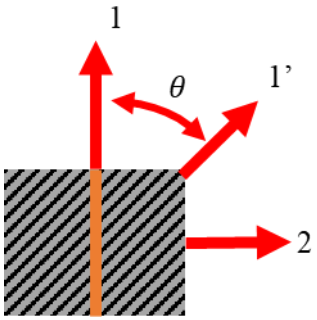

Figure 3.16 SMAHC Laminate Axes with Ply Angle

Given that the laminate is modelled with shell and beam elements, the cross-section is abstracted in the model. Starting at the top of the laminate, there is an adhesive layer which holds the SMA. There is then the FRP ply stack. The adhesive and FRP plies are defined within a single shell element. The SMA beam elements are given the same diameter as the SMA wire and are offset along the third axes so they pass through the middle of the adhesive ply.

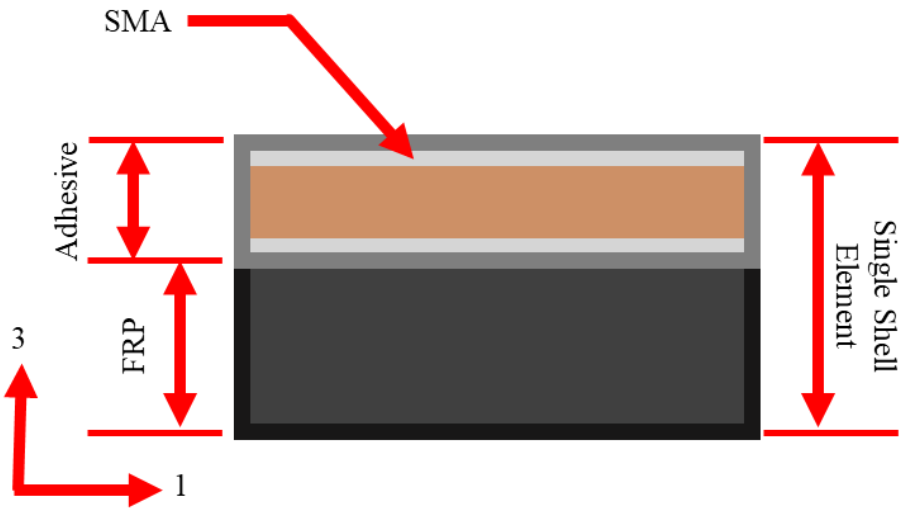

Figure 3.17 SMAHC Laminate Model Cross Section

The complete SMAHC layup in conventional bottom to top format is expressed using Eqn. 3.16. However, given that the adhesive and SMA layer is constant for all trials, it is convenient to compress this. Since the FRP angles are the only laminate parameters varied, the layup is compressed as in Eqn. 3.17. Symmetric laminates can be further compressed, as in Eqn. 3.18. Laminates described using the compressed convention for SMAHCs are denoted with a superscript C on the outside of the brace.

Eqn. 3.16. Total Laminate Layup:

$$\{\theta_{1,\mathrm{FRP}}/\theta_{2,\mathrm{FRP}}/\ldots\theta_{n,\mathrm{FRP}}/Adhesive-SMA\}_T$$

Eqn. 3.17. Compressed Total Laminate Layup:

$$\{\boldsymbol{\theta_1/\theta_2/\ldots\theta_n}\}_T^C = \{\theta_{1,\mathrm{FRP}}/\theta_{2,\mathrm{FRP}}/\ldots\theta_{n,\mathrm{FRP}}/Adhesive-SMA\}_T$$

Eqn. 3.18. Compressed Symmetric Laminate Layup:

$$\{\boldsymbol{\theta_1/\theta_2/\ldots\theta_n}\}_S^C = \{\theta_{1,\mathrm{FRP}}/\theta_{2,\mathrm{FRP}}/\ldots\theta_{n,\mathrm{FRP}}/\,\theta_{n,\mathrm{FRP}}\ldots/\theta_{2,\mathrm{FRP}}/\theta_{1,\mathrm{FRP}}/Adhesive-SMA\}_T$$

The SMAHC laminate in-plane geometry is shown in Figure 3.18. The wire length and the panel width respectively define the edges parallel and perpendicular to the wires. The wire spacing

defines the distance between SMA wire centres. The 1st wire passes through the centre of the laminate, and the number of SMA wires is mirrored about this. Geometric parameters are expressed as normalized with respect to panel width, as shown in Eqn. 3.19 and Eqn. 3.20.

Eqn. 3.19. $$Wire\ Density = \frac{Wire\ Spacing}{Panel\ Width}$$

Eqn. 3.20. $$Aspect\ Ratio = \frac{Wire\ Length}{Panel\ Width}$$

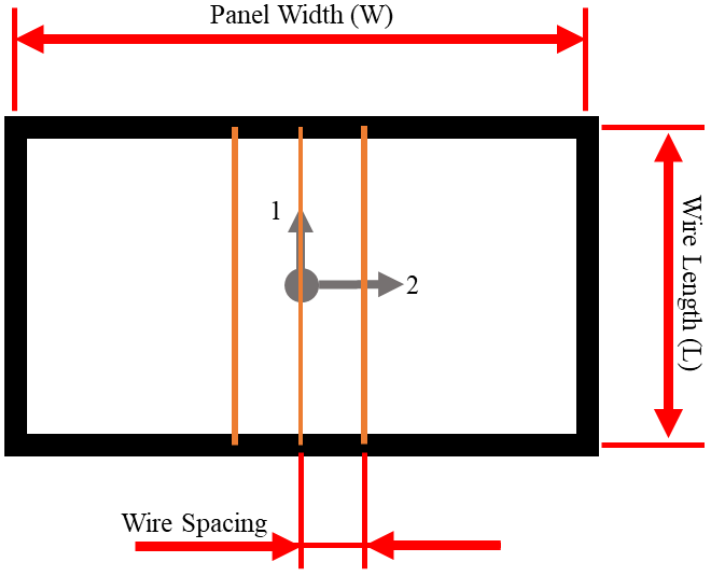

Figure 3.18 SMAHC Laminate Geometric Parameters

For this model there are two element densities of interest. The first density is the number of elements previously defined as R_{Elem} (see Eqn. 3.15), or the number of SMA beam elements per FRP shell element edge. The second is the minimum number of elements between SMA wires (M_{Elem}), which must be sufficiently fine to capture laminate curvatures accurately. These two parameters are graphically shown in Figure 3.19. M_{Elem} is used to calculate the shell seed size (S_{Shell}) as shown in Eqn. 3.21 to ensure an aspect ratio of approximately 1:1 to ensure mesh validity. Shell seed size is then used to calculate the SMA beam seed size (S_{Beam}) using Eqn. 3.22. With the seed sizes defined, the preload length applied to each of the preloaded SMA elements can be calculated as in Eqn. 3.23.

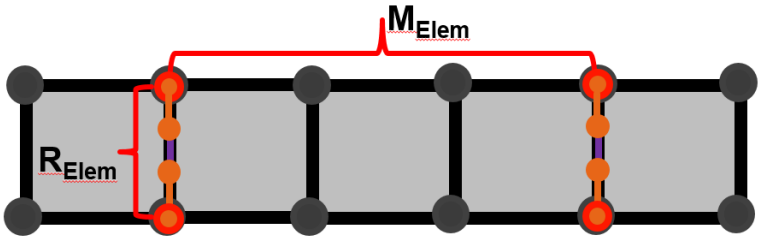

Figure 3.19 Convergence Element Ratios R_{Elem} & M_{Elem}

Eqn. 3.21. FRP Shell Seed Size [mm]: $S_{Shell} = M_{Elem} * Wire\ Spacing$

Eqn. 3.22. SMA Beam Seed Size [mm]: $S_{Beam} = R_{Elem} * S_{Shell}$

Eqn. 3.23. Preload Length [mm]: $L_{Pre} = S_{Shell} * \varepsilon_{Pre}/(R_{Elem} - 2)$

3.2.5.3. Model Algorithm

The proposed model depends on tying together nodes and applying bolt loads at the element and node levels. The overall algorithm is shown in Figure 3.20, with detailed flow charts in **Appendix A-5.** To summarize the code, a rectangular shell is generated and partitioned where the SMA wires are desired, ensuring that nodes will exist in the FRP plate along the SMA wire. A single SMA wire part is generated and patterned in the assembly according to the desired wire density and count. Using the known geometry and seed sizes, the script loops through the SMA elements and nodes, selecting elements for bolt loads and SMA and plate nodes for constraints. The bolt loads and constraints are applied in this step. The two default steps created are the SMA preload step and cooling from gelation to operating temperature, which are defined by the manufacturing cycle. Subsequent steps must be written in by the user either in ABAQUS\CAE or via script.

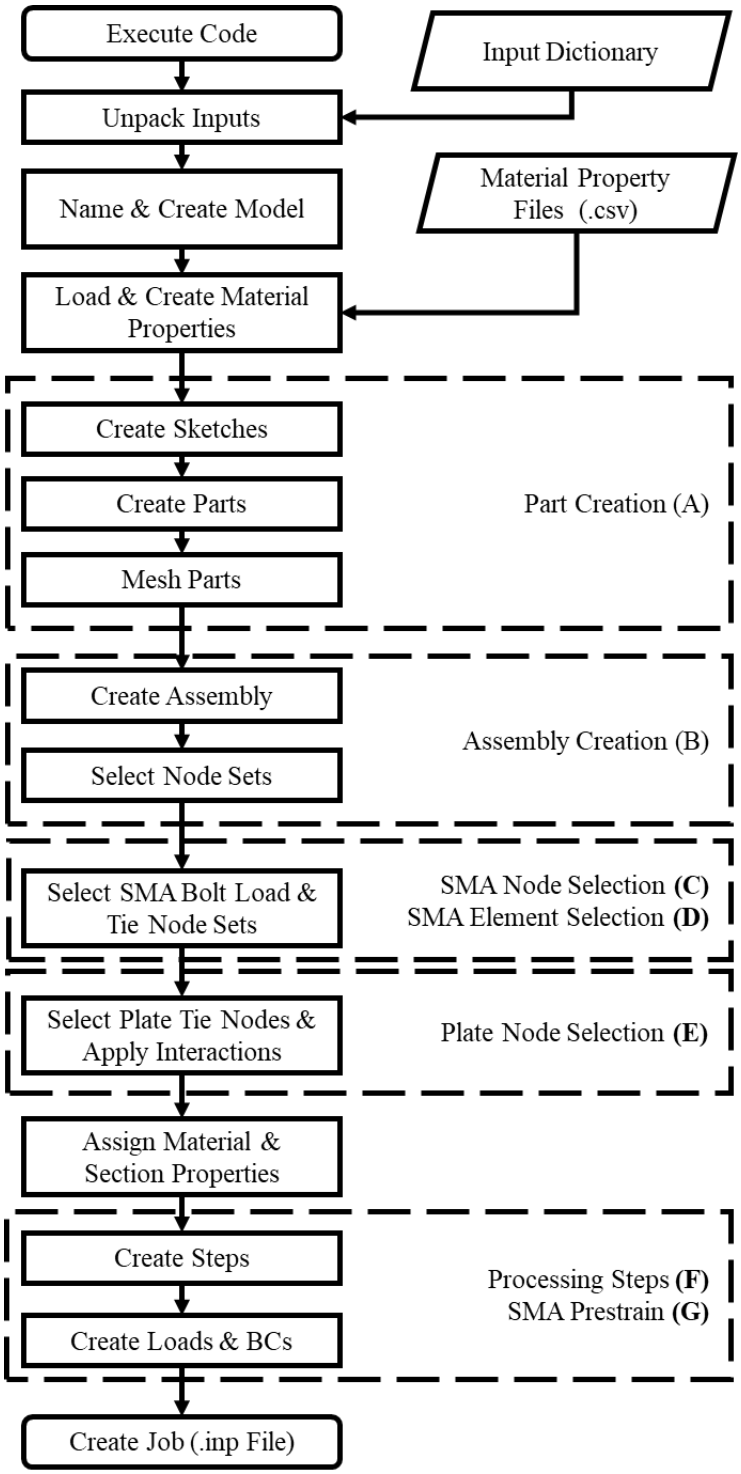

Figure 3.20 SMAHC ABAQUS Model Generation Code Overview Flowchart with Subsections in **Appendix A-5**.

3.2.5.4. Mesh Convergence Testing

A unique feature of the proposed model is that it involves multiple steps to build a model that represents the desired, as-manufactured part. Firstly, the SMA elements must be prestrained and then the laminate must be cooled from gelation temperature to operating temperature. From here, thermal loads can be applied to the SMAs and mechanical loads to the laminate to simulate the in-use behaviour. In general, the parts made in this process are not expected to see stress concentrations as they will be gently curved or flat plates. The following test case is used for the convergence test with a sample result shown in Figure 3.21.

- 100x100 [mm] $\{90_4\}_T^C$ Laminate
  - IM7-8551 FRP properties from [100]
  - 8551-7 Adhesive properties from [100]
  - SMA properties from Table 2.7 on page 38
- 19 SMA wires & 5 [mm] wire spacing

0. Fixed Centre Node & 180 [^{o}C] T_{Gel} (Initial Step)
1. 5 [ε%] SMA Prestrain (Step 1)
2. 21 [^{o}C] Operating Temperature (Step 2)
3. 95 [^{o}C] SMA Actuation Temperature (Step 3)
4. Displace Corner Nodes to 0 in out-of-plane direction (Step 4)

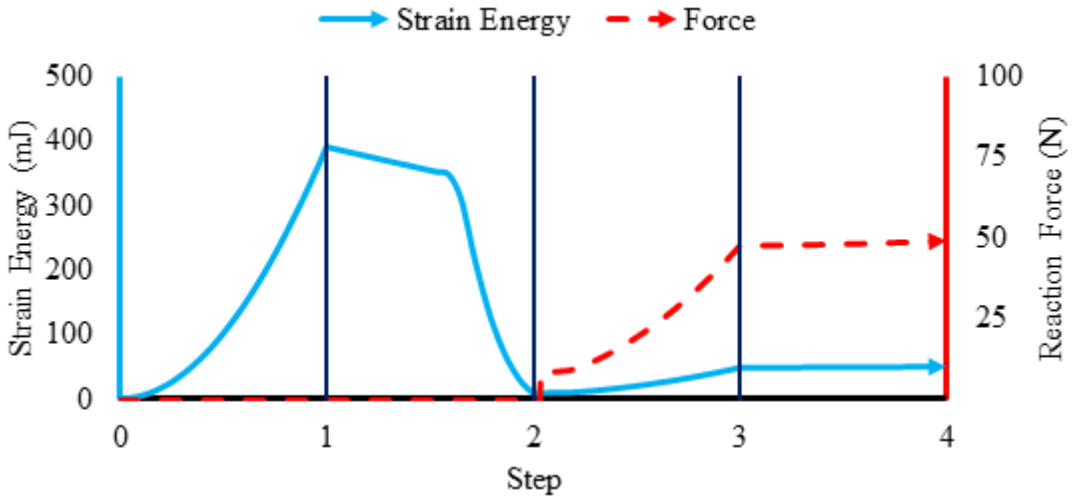

Figure 3.21 Convergence Test Sample Result

Given the number of steps required to process the SMAHC, an end-point value (i.e. max stress) which is typically used to evaluate convergence does not necessarily capture all trends. Rather, it is more appropriate to compare the evolution of parameters through all these steps. The two parameters used are total strain energy and reaction force at the fixed centre node. The total strain energy captures the global behaviour of the laminate. The reaction force captures force at a boundary which is the only location in this structure where a numerical singularity may occur. Both element densities R_{Elem} and M_{Elem} are evaluated for convergence.

The results of the convergence study are presented in terms of a coefficient of determination (R^2) for all simulation steps relative to the densest mesh studied are shown in Table 3.4. In all studies, the coefficient of determination is exact until at least the 5th decimal place, indicating that mesh density has little effect on the accuracy of this FE model. This is because even the coarsest mesh used is 1.7 [%] of the edge length, finer than the 5 [%] required to model unsymmetric laminates, as found in Section 3.2.3. A 1:1 element aspect ratio is maintained and there are only gentle curves are observed, so there is no expectation of mesh distortion errors or singularities. Therefore, it can be concluded that element ratios of R_{Elem} of 5 and a M_{Elem} of 3 provide a dense enough mesh for the proposed SMAHC model.

Table 3.4 Coefficient of Determination (R^2) for SMAHC Convergence Studies

R^2 [Strain Energy] (Reaction Force)		**M_{Elem}** **9**	**7**	**5**	**3**
R_{Elem}	**13**	**Reference**	\	\	\
	11	[1](1)	\	\	\
	9	[1](1)	\	\	\
	7	[1](1)	\	\	\
	5	[1](1)	[1](1)	[1](1)	[1](1)

3.2.6. Summary of SMAHC Model Development

In this section a novel method of modelling shape memory alloy hybrid composites is devised using tools available in ABAQUS. Components of this model are verified either in the referenced literature or within this section. With the proposed modelling methodology, a finite element model is built and tested for convergence. It is shown that this technique converges for the entire path of SMAHC processing and loading. The SMAHC FE model is not experimentally validated.

3.3. Parametric Studies of SMA Hybrid Laminates

The goal of this parametric study is to gain introductory insight into the effect of various design variables on the behaviour of SMAHC panels. Due to the number of potential parameters, the known and potential couplings of parameters, and preliminary nature of this discussion, a factorial approach to design of experiments is not used. A list of known influencing parameters which are both considered and not considered in this study is in Table 3.5 and a break down of values investigated are listed in Table 3.6.

Table 3.5 Parameters Affecting SMAHC Behaviour

Parameters Considered	Parameters Not Considered
• Ply Angle for Symmetric Stacks[4] • Wire Count[4,5] • SMA Prestrain[6] • Cure Temperature[6] • Wire Density[5] • Aspect Ratio	• Material Properties • Unsymmetric Laminates • Laminate Thickness • Placement of Wire within Laminate

[4] Ply Angle and Wire Count are simultaneously evaluated in a coupled parametric study

[5] Wire Count and Wire Density are simultaneously evaluated in a coupled parametric study

[6] SMA Prestrain and Cure Temperature are simultaneously evaluated in a coupled parametric study

Table 3.6 Values for Parameters Affecting SMAHC Behaviour

Symmetric Layup $\{\theta/-\theta\}_S^C$ [Degrees]	Wire Count	Wire Density (Eqn. 3.19)	Aspect Ratio (Eqn. 3.20)		Cure Temperature (Relative, Eqn. 3.3) [°C]	SMA Prestrain [mε]
0	11	$1/100$	$1/6$	1 1/2	99	25
15	21	$1/60$	$1/3$	1 2/3	119	40
30	31	$1/50$	$1/2$	1 5/6	139	55
45	41	$1/30$	$2/3$	2	159	
60	51	$1/20$	$5/6$	2 1/6		
75			1	2 1/3		
90			$1\ 1/6$	2 1/2		
			1 1/3			

3.3.1.2. Material Properties for Parametric Study

The same material properties are used for all SMAHC laminates in the parametric study, shown for the FRP in Table 3.8, Adhesive in Table 3.7, and SMA from Table 2.7 on page 38.

Table 3.7 FM-300 Material Properties from [116]

Thickness [mm]	Young's Modulus (E) [MPa]	Poisson's Ratio (v)	Coefficient of Thermal Expansion (α) $\left[\frac{\mu m}{m*K}\right]$
0.13	2400	0.4	60

Table 3.8 NCT-301 Material Properties

Thickness [mm]	Modulus [MPa] [117]				Poisson's Ratio (v_{12}) [117]	Coefficient of Thermal Expansion (α) $\left[\frac{\mu m}{m*K}\right]$ [100]		
	E_{11}	E_{22} & E_{33}	G_{12} & G_{13}	G_{23}		α_{11}	α_{22}	α_{33}
0.13	113900	7986	3138	3071	0.288	0.14	30.98	30.98

3.3.2. Parametric Model Setup & Analysis Methods

A similar model is used for all parametric studies, which is shown in its generalized form in Figure 3.18 and Figure 3.22. Panel Width (see Figure 3.18) is fixed at 150 [mm] for all trials, which is within the size known to exhibit bistable behaviour with an aspect ratio of 1 [98]. The boundary conditions applied to the panel are intended to prevent only rigid body motion of the panel, shown in Figure 3.22 and described as follows:

- Corner nodes one through four (CN1, CN2, CN3, & CN4) fixed in Z axis translation
- Corner nodes one and two (CN1 & CN2) fixed in Y axis translation
- Corner nodes one and three (CN1 & CN4) fixed in X axis translation

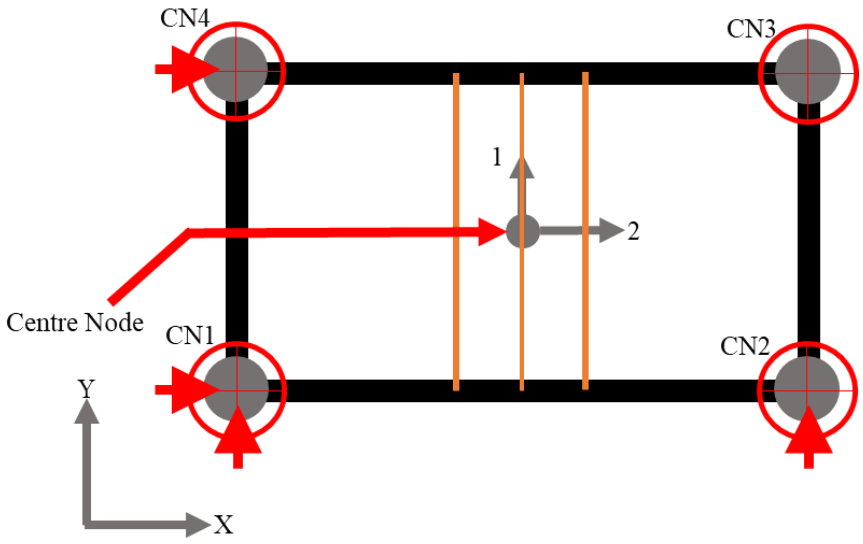

Figure 3.22 Parametric Study FE Model Boundary Condition and Load Setup

The loads applied to the panels are intended to simulate both the after thermal cool down effects and the behaviour under two separate load cases, SMA heating (actuation) and external out of plane loads. Chemical effects of laminate curing are not considered. The steps are included below.

0) Prestrain is applied to the SMA elements (see **Section 3.2.4.1** on page 62)
1) The laminate is cooled from gel temperature to a room temperature of 21 [^{o}C] and the SMAs to the reference temperature (see T_0 in Table 2.7 on page 38)
2) The SMA wires are then heated to $T_{Heat} = 95\ [^{o}C]$ to simulate actuation
3) Lastly, a load is applied to the centre node (see Figure 3.22 on page 81) to simulate out of plane behaviour and measure the out of plane response

To measure the laminate response, the as-cured curvature, change in curvature due to actuation, and snap through force are used. The as-cured curvature (κ_i^{AC}, see Eqn. 3.24) captures the shape of the laminate due to residual stress from thermal shrinkage as well as the prestrain of SMAs in steps 0→1. The change in curvature ($\Delta\kappa_i^{AW}$, see Eqn. 3.25) expresses the actuation available from heating the SMAs in step 2. Snap through force (F_{Snap}, see Eqn. 3.5) is measured in the third step as representative of the out-of-plane behaviour of the laminate.

Eqn. 3.24. As-Cured Curvature

$$\kappa_i^{AC} = \kappa_i^{AW}|_{T_{Laminate}^{Relative}=0\ [^oC]\ \&\ T_{SMA}=T_0}$$

κ_i^{AW} is calculated with Eqn. 3.2

$T_{Laminate}^{Relative}$ is calculated with Eqn. 3.3

T_0 is from Table 2.7.

Eqn. 3.25. Change in Curvature

$$\Delta\kappa_i^{AW} = \frac{\kappa_i^{AW}|_{T_{SMA}=\mathrm{T_{Heat}}} - \kappa_i^{AW}|_{T_{SMA}=T_0}}{\kappa_i^{AW}|_{T_{SMA}=T_0}} * 100\ [\%]$$

3.3.3. Reference Case

Prior to the parametric study, it's useful to discuss in detail a reference case, setup with baseline values, and to gain a more detailed insight into how the laminates respond to the implemented load cases. The reference case parameters are shown in Table 3.9.

Table 3.9 Reference Case Parameters

Symmetric Layup $\{\theta/-\theta\}_S^C$ [Degrees]	Wire Count	Wire Density (Eqn. 3.19)	Aspect Ratio (Eqn. 3.20)	Cure Temperature (Relative, Eqn. 3.3) [^{o}C]	SMA Prestrain [mε]
45	41	$^1/_{60}$	1	159	40

The 1st axis curvature response is shown in Figure 3.23. In the initial state, without any loads, the plate is flat. In the first step, when prestrain is applied, a gentle curvature is observed, which is expected as the SMA wires are on the surface of the layup. The curvature becomes more significant during the cooling from cure temperature to room temperature due to the orthotropic thermal expansion. Further curvature is created when the SMA is heated, due to the increase in applied stress of the SMA. Lastly, this laminate exhibits a snap through behaviour during load application.

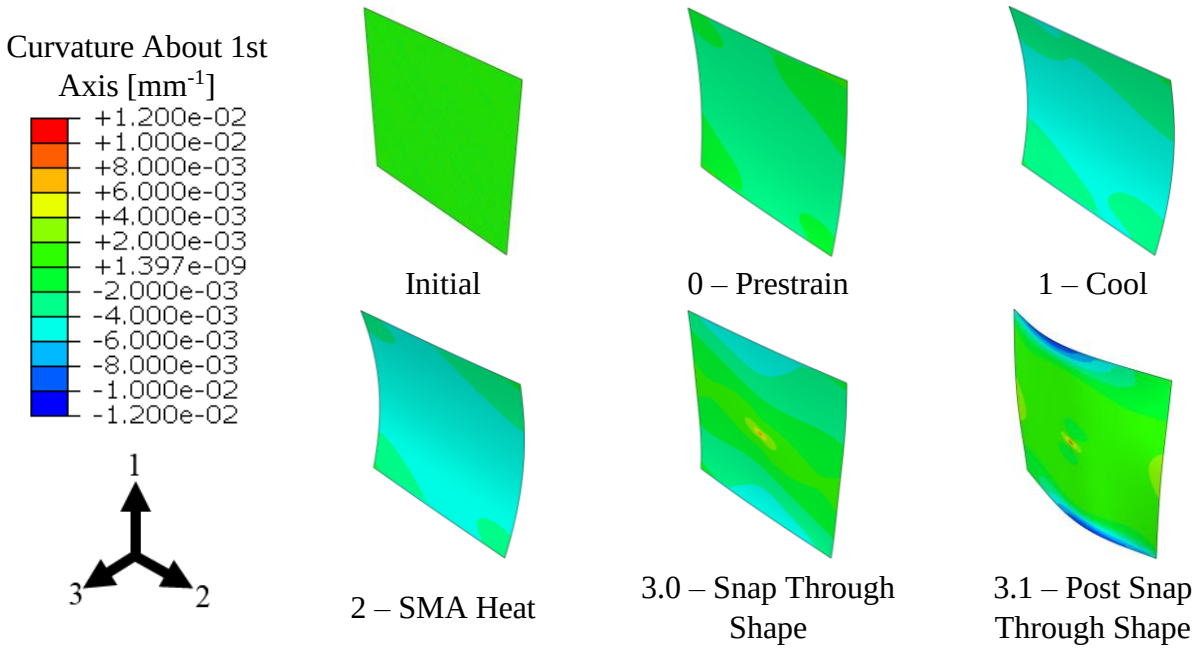

Figure 3.23 Reference Case Finite Element Curvature Results

A quantitative representation of this response is shown in Figure 3.24. Again, the out of plane displacement as well as the curvature evolve most significantly during the 1st (prestrain) and 2nd (laminate cooling) steps. Changes to out of plane displacement and curvature are observed, but to a lesser degree, during the SMA heating step. It's interesting to note the non-linearity of the SMA heating response. Despite the SMA exhibiting a linear $\sigma(T)$ response, the non-linearity is likely a result of the prestrain and laminate curvature. A very sharp curvature and displacement response is observed in the 3rd step, confirming the previously observed a snap through response.

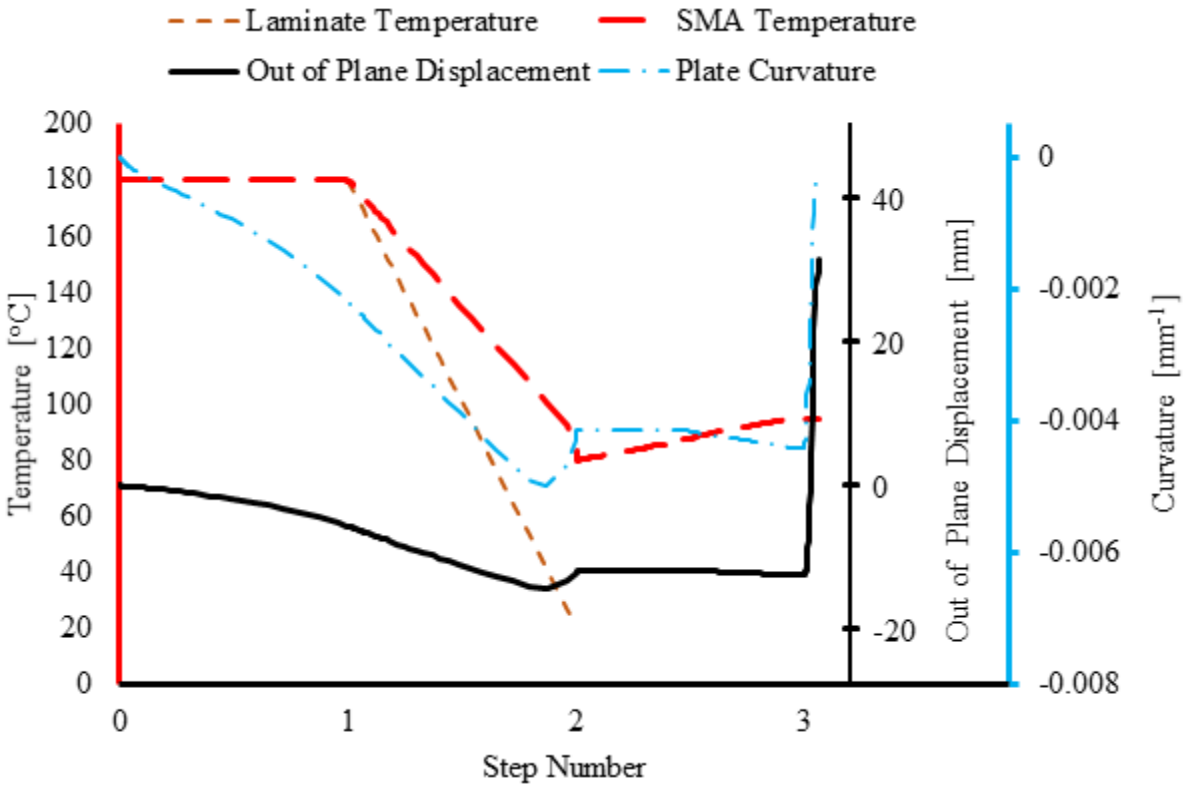

Figure 3.24 Processed Finite Element Results for Reference Case

The reference case shows three key states, curvature introduced during the prestrain steps, the curvature and displacement due to the SMA heating, and the snap through response due to the unsymmetry of the laminate.

3.3.4. Finite Element Parametric Study of Wire Density

The first parameter evaluated is the effect of wire density on the response of the laminates for wire counts between 11 and 41. The first result, shown in Figure 3.25, is the initial curvature vs. wire spacing. It appears the initial curvature is independent of wire spacings, which is sensical the cumulative wire force, which dictates the initial curvature, is dependent on number of wires and not their spacing.

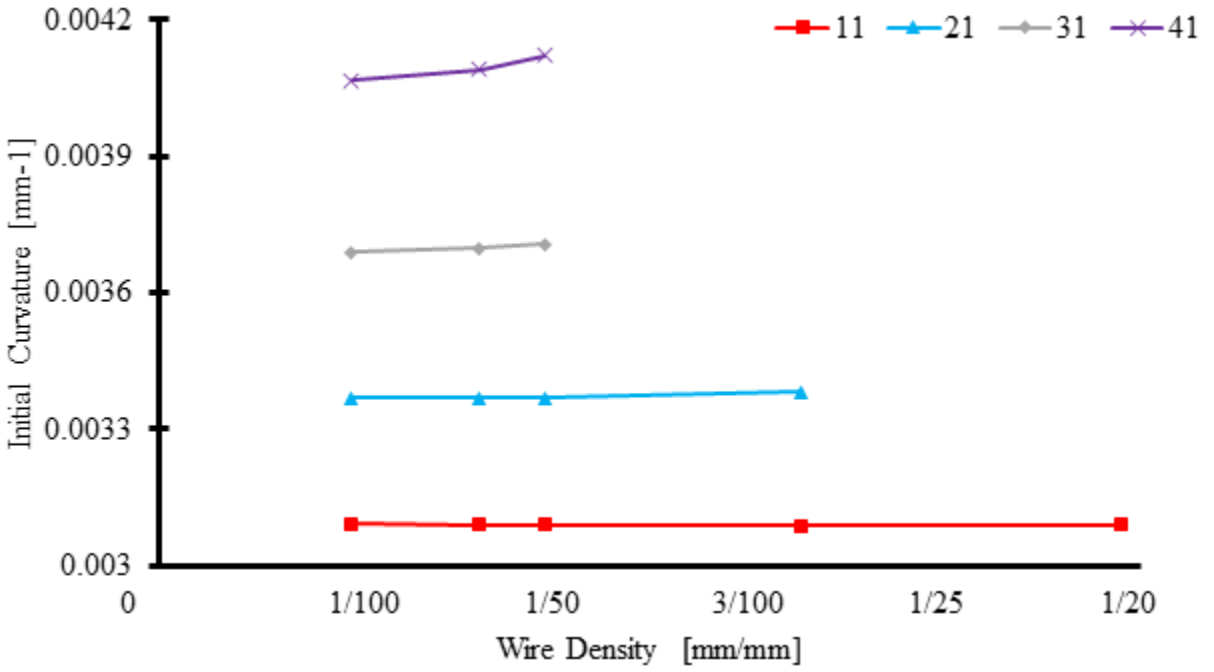

Figure 3.25 Initial Curvature (End of Step 1) vs. Normalized Wire Spacing for Multiple Wire Counts

The curvature change between the beginning and end of Step 2 is plotted in Figure 3.26 which is observed to be independent of wire spacing for the 11 and 21 wire cases, while significantly less curvature change is possible for the 31 and 41 wire counts at lower wire densities. This indicates that both stress gradient (correlated to wire density) and applied stress (correlated to wire count) contribute to the behaviour. It appears that as wire count increases, so must wire density to maximize actuation capability.

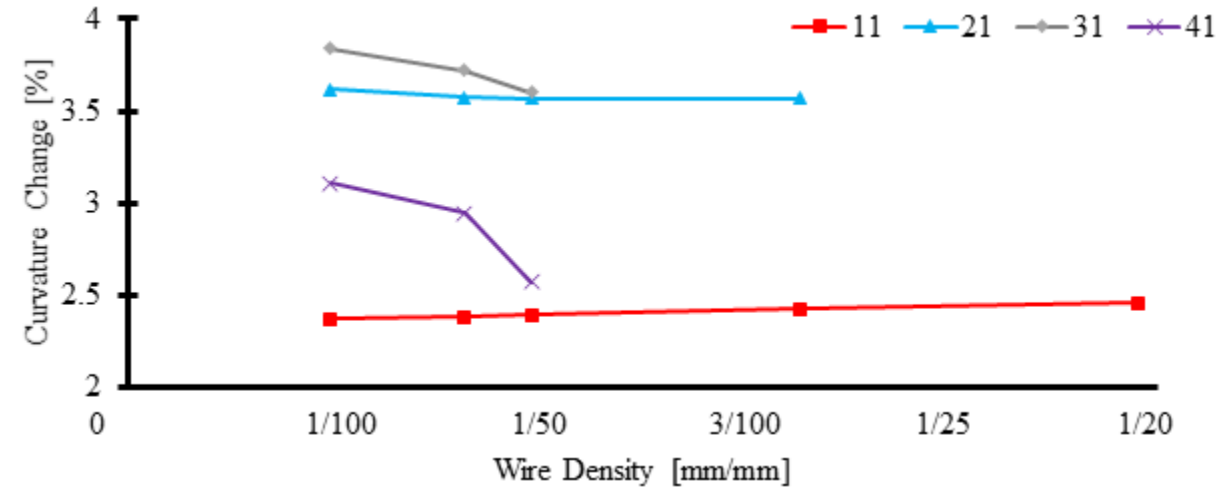

Figure 3.26 Beginning to End of Step 2 Curvature Change vs. Wire Density for Multiple Wire Counts

The final metric, snap through force (shown in Figure 3.27) appears to also be significantly affected by wire density. Upon detailed investigation, true snap through behaviour is only observed for 31 wires with 1/50 spacing and 11 wires with 1/30 spacing. While nonlinearity is observed for all cases, the 21 wire with 1/60 spacing exhibits a highly non-linear response without snap through. This result is extremely interesting, as it indicates that while number of wires in the panel dictates the as cured shape, the stress distribution will have a significant effect on the out of plane behaviour as well. It appears that whose curvature change is wire density independent (11, 21, and 31) have an out of plane response that is highly dependent on wire density.

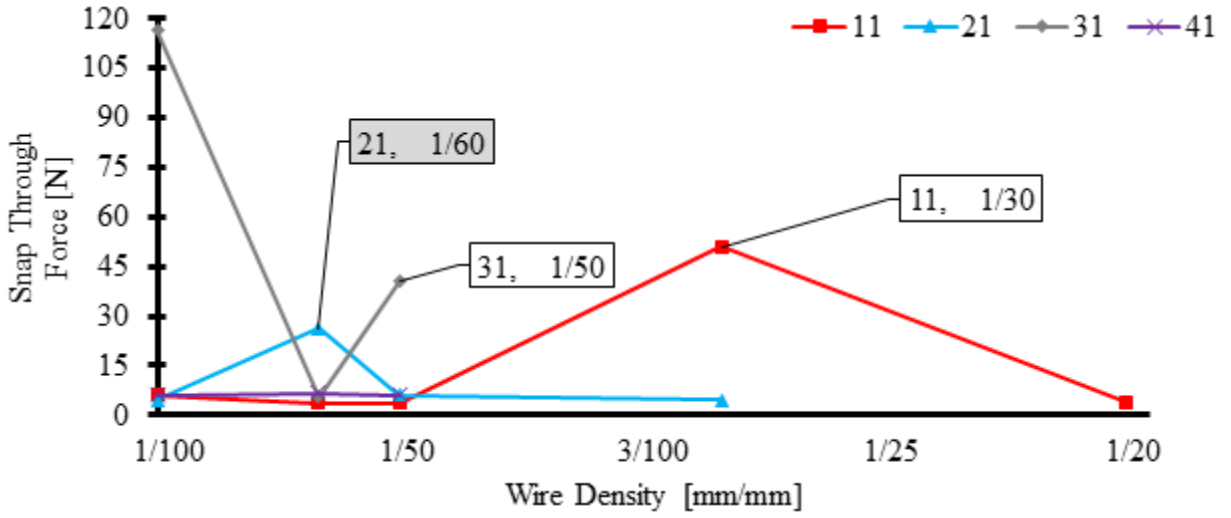

Figure 3.27 Snap Through Force vs. Wire Density for Multiple Wire Counts

Looking at the stress distribution for 11 wire panels in Figure 3.28, it becomes clear that wire count significantly changes the stress distribution in the panel. The panel which exhibits snap through has a wire density of $1/30$. Along the centre of the $1/20$ panel there is near zero 1st axis stress. There is a significant compressive stress along the centre of the $1/50$ panel, and significant tensile stresses along the edge. The $1/30$ panel has slight compressive stress along the centre of the panel. Clearly the stress distribution effects the out of plane response, and there is a balance to be struck to achieve the desired out of plane response, but a clear pattern is not observed.

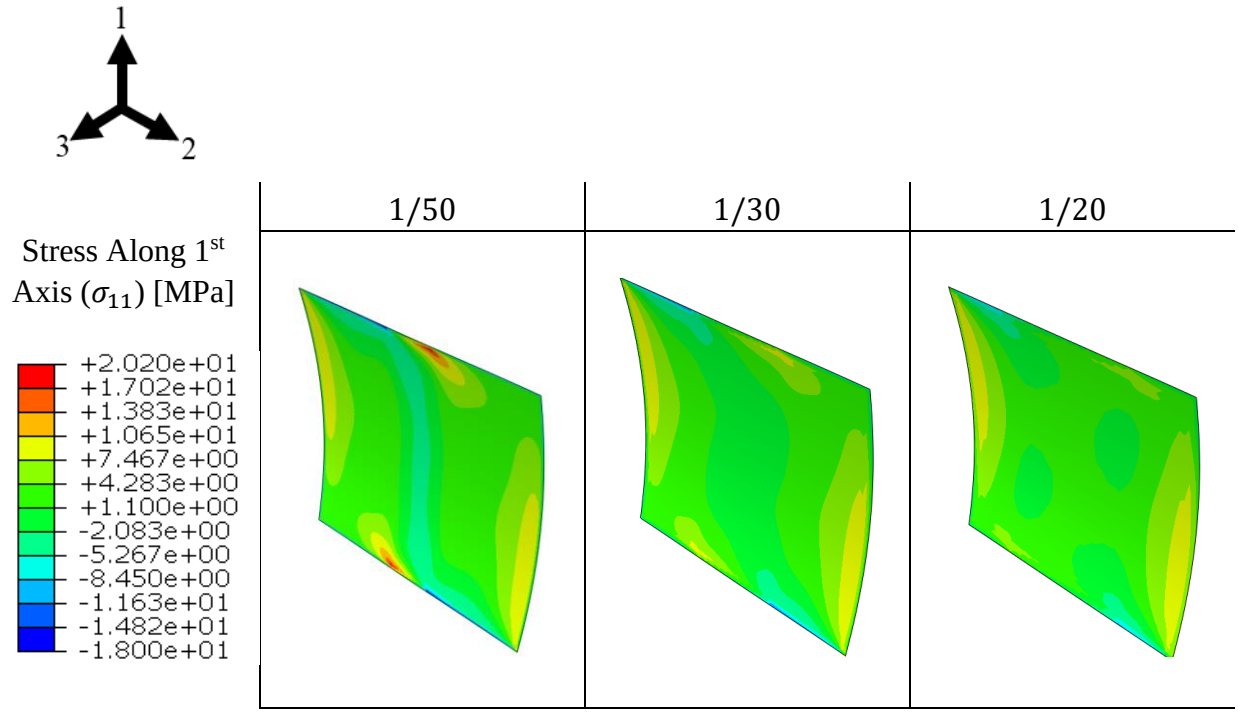

Figure 3.28 End of Step 1 Stress distribution for 11 Wires and Multiple Wire Densities

A second interesting way of probing this result is with the phase transformation percentage (PTP) of the SMA wires in the panel, as shown in Figure 3.29. Phase transformation percentage captures the SMAs' full thermo-elastic state in a single parameter. While the average PTP changes by a small amount, the PTP gradient (ΔPTP in Eqn. 3.26) appears inversely proportional to wire density. This is expected, as there is more uniform stress in the less dense panel, whereas in the dense panels there are wires inside and outside of the high stress region. This will affect the rate and uniformity of the phase transformation during out of plane loading, leading to the difference in out of plane loading response observed.

Eqn. 3.26. Phase transformation percentage gradient: $\Delta PTP = \mathrm{PTP_{Max}} - \mathrm{PTP_{Min}}$

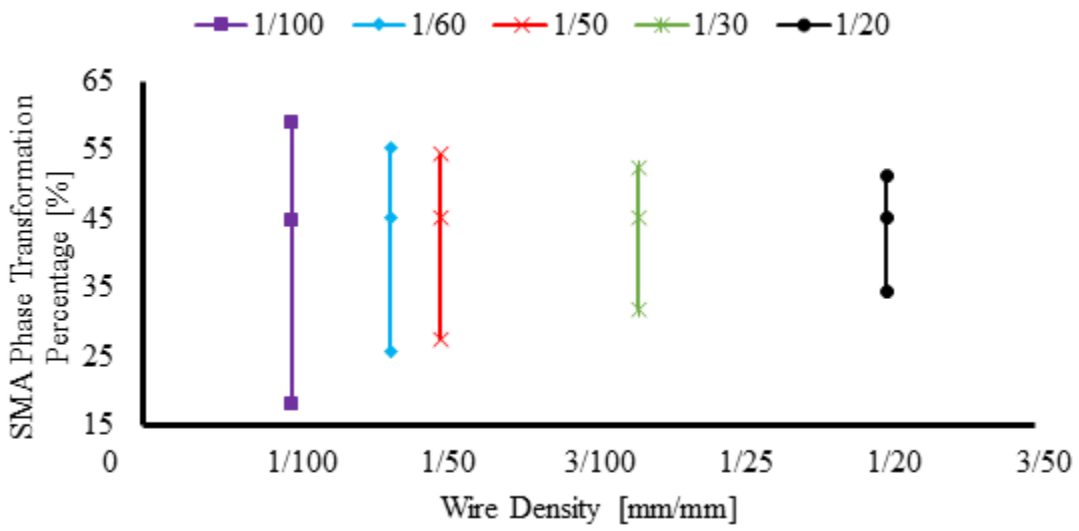

Figure 3.29 Shape Memory Alloy Phase Change Percentage [%] maximum, minimum, and average vs Wire Density at the end of Step 1

Firstly, no effect on initial curvature is observed as a result of wire spacing. However, the stress distribution and PTP are affected by the wire density, which will significantly affect the stress-linked responses (change in curvature and snap through force). No clear trend is observed, indicating the importance of having clear design goals when selecting wire spacing and count.

3.3.4.2. Finite Element Parametric Study of Aspect Ratio

The first study addresses aspect ratio, as defined in, as Tawfik [98] observed this to have significant effects on snap through behaviour. The results of the aspect ratio study are shown in Figure 3.30. While the initial curvature trend appears to be continuous with aspect ratio, the change in curvature and snap through force show three different behaviours. As a result of these differences in the response, the results are divided into three zones, Z-1, Z-2, and Z-3.

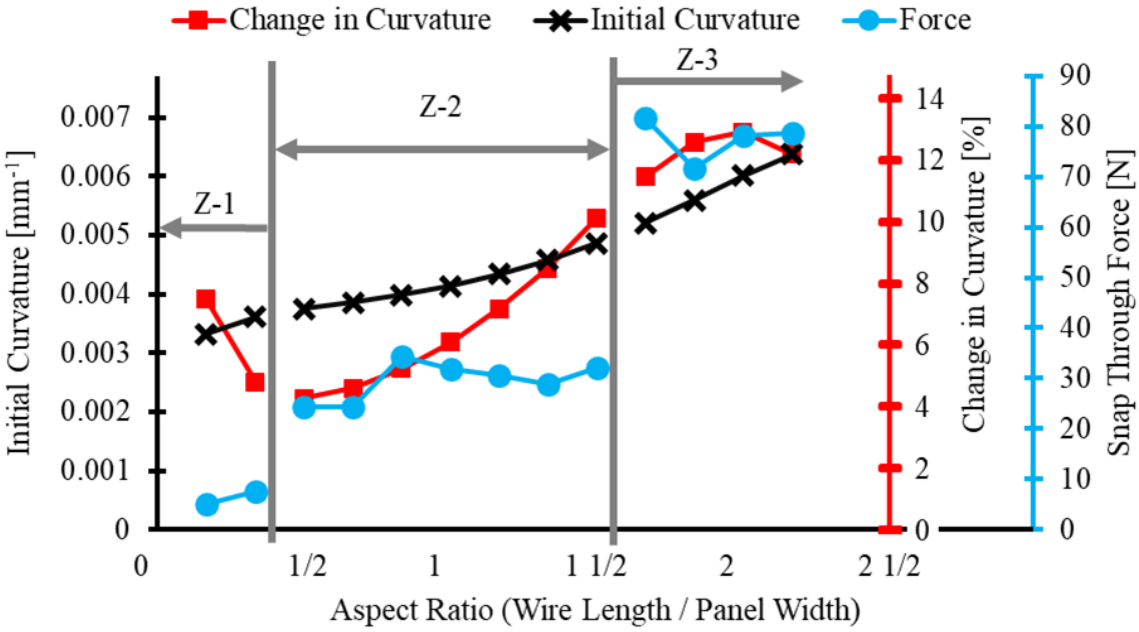

Figure 3.30 Initial Curvature, Change in Curvature, and Snap Through Force vs. Aspect Ratio

In Z-1, the change in curvature decreases and the snap through force increases with increasing aspect ratio. When the Force vs. Displacement response is studied, as in Figure 3.31, the 1/3 aspect ratio in Z-1 exhibits a non-linear response, but no large discontinuity associated with true snap-through. At small aspect ratios, the out-of-plane response is not governed by buckling.

In Z-2, a highly non-linear out of-plane response, comparable to a damped snap through, is observed for the smallest case (1/2, see Figure 3.31), while significant discontinuities are observed at the upper case (1 ½, see Figure 3.31). The snap through forces remain relatively constant, while more curvature change is possible with increasing aspect ratio in this region.

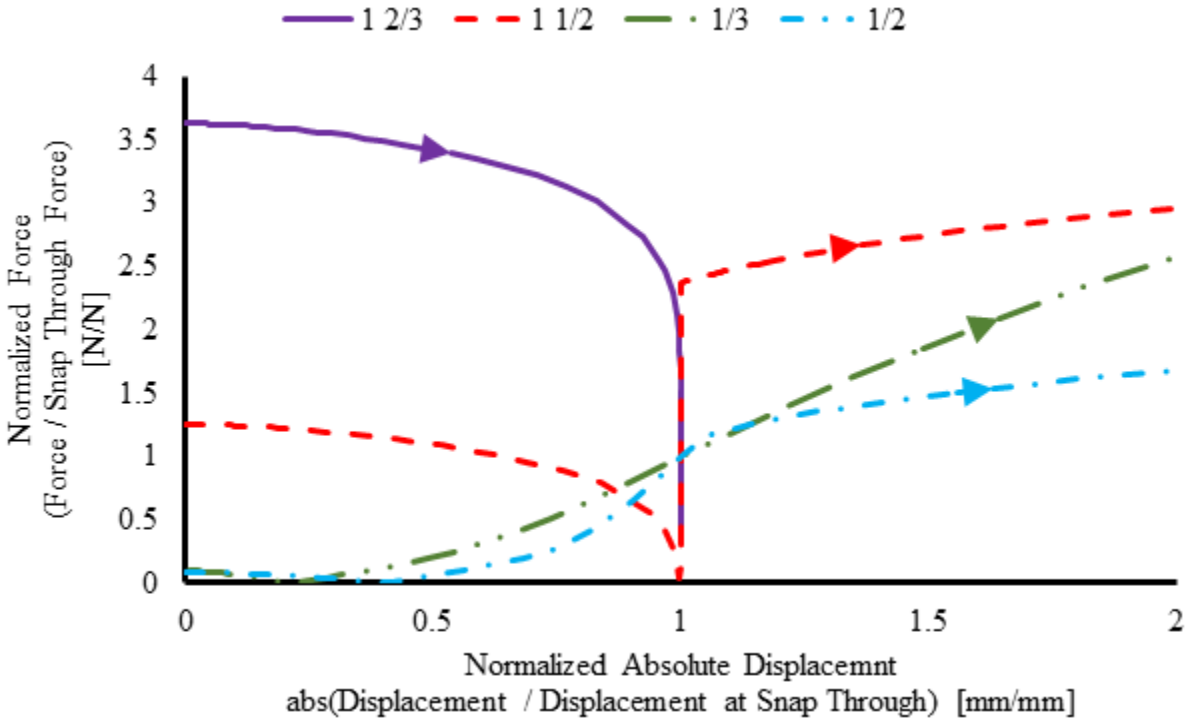

Figure 3.31 Initial Normalized Force vs. Normalized Absolute Displacement for Multiple Aspect Ratios

The third Zone (Z-3) is marked by a significant increase in the snap through force and an inversion of the aspect ratio vs. [%] curvature change response. While instability is observed at a critical force (see Figure 3.31), no stable response is exhibited after buckling occurs. When looking at the physical results, shown in Figure 3.32, the difference in response is clear. For the largest aspect ratio case in Z-2 (1 ½), snap-through is observed and the post-buckled shape is of the 1st mode. For the smallest aspect ratio in Z-3 (1 2/3), a similar unloaded shape is observed while the post-buckled shape is of the 3rd mode. The aspect ratio of the panel effects the buckling response which is captured in change in loading behaviour.

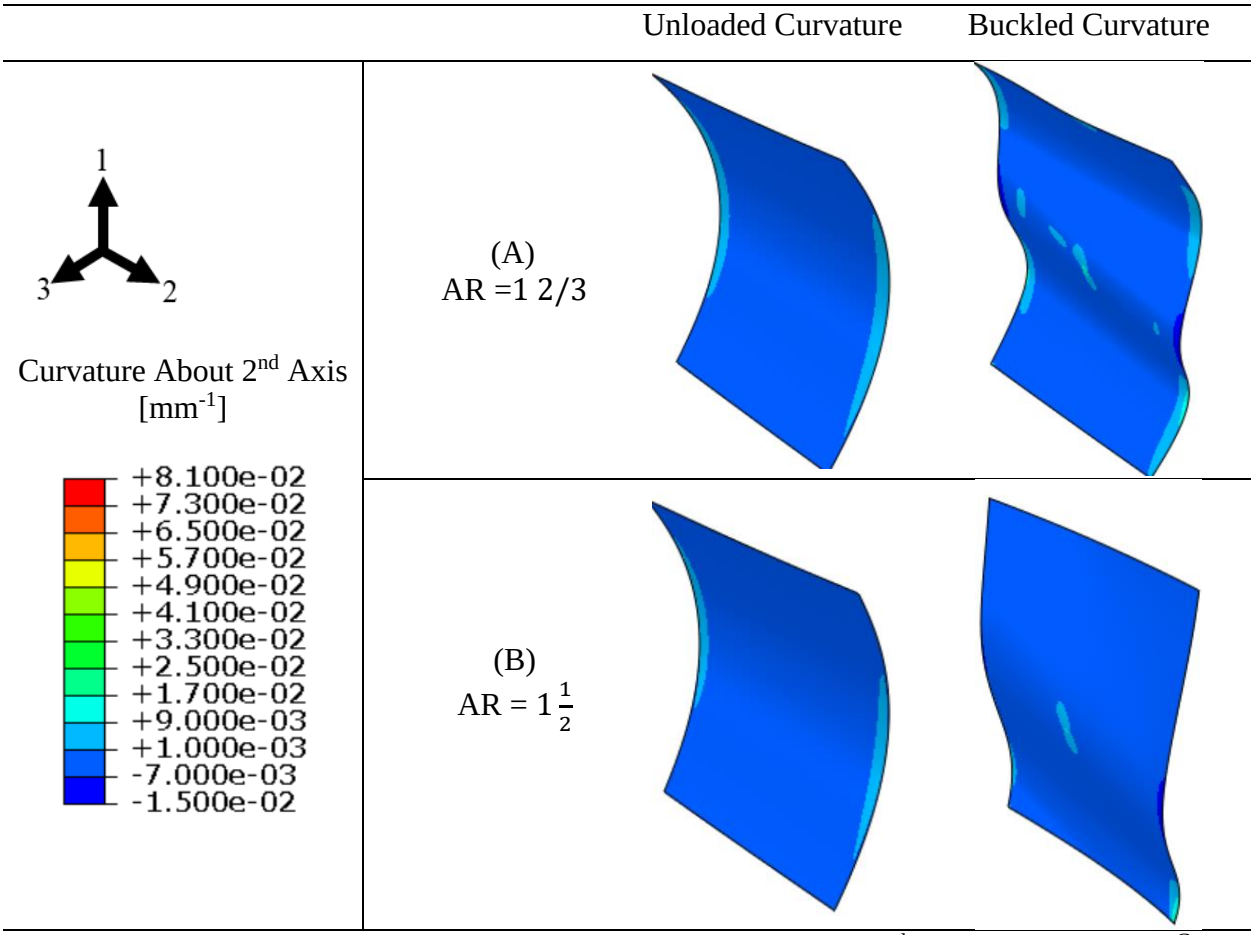

Figure 3.32 Pre- and Post- Snap-Through Curvatures about 2nd Axis for a $\{45/-45\}_S^C$ Laminate with 41 SMA Wires Spaced at 1/60 Panel Widths for a (A) 1 2/3 and (B) 1 1/2 Aspect Ratio SMAHC Panels

To summarize the results of the aspect ratio study, three distinct behaviours are observed. At low aspect ratios, an inverse relationship between aspect ratio and change in curvature is observed and no buckling behaviour is observed in response to out of plane loads. At medium aspect ratios, a linear relationship between aspect ratio and change in curvature is observed, with a non-linear 1st mode buckling response to out of plane loads. High aspect ratios again invert the curvature change response and exhibit higher mode buckling responses to out of plane load. While these behaviours are sensitive to other parameters, Aspect Ratio is clearly a parameter which can be leveraged to tailor significantly different responses of SMAHC laminates.

3.3.5. Finite Element Parametric Study of Symmetric Ply Angle and Wire Count

This study investigates the coupled response of ply angle for symmetric layups and wire count. The first result, Initial Curvature vs. Ply Angle, is shown in Figure 3.33. When the fibre orientation is 0 [Degrees] – i.e. carbon fibres & SMA wires are aligned – there is negligible curvature introduced during the manufacturing process. In general, as the angle becomes greater the initial curvature increases, expected due to the relative softness in the transverse direction of the CFRP. For high wire counts (41 and 51 wires) and ply angles (90 [Degrees]), the solution is unstable due to the very high degree of curvature. The greater the ply angle, the greater the difference in initial curvatures between each wire count, indicating a coupling of these factors.

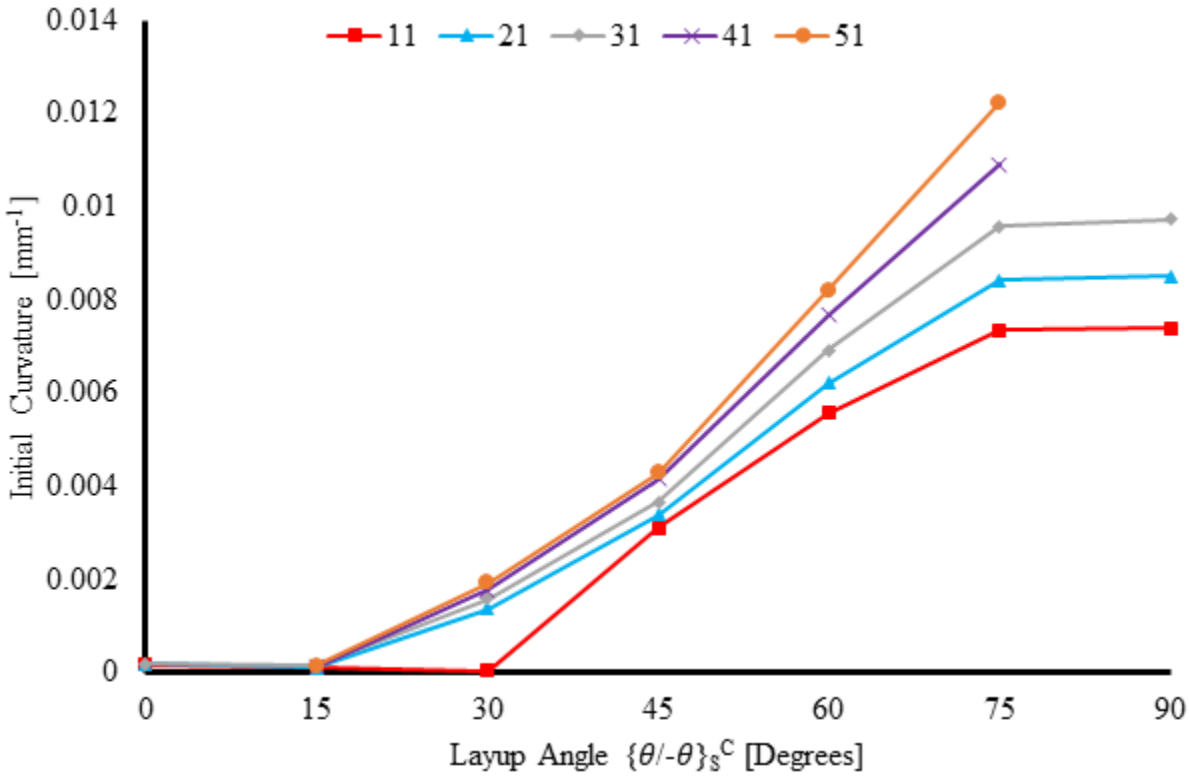

Figure 3.33 Initial Curvature vs. Layup Angle for Multiple Wire Counts and Ply Angles

When looking at the change in curvature (Figure 3.34), it is observed that, generally speaking, increasing wire counts and ply angles increase the change in curvature. There are, however, certain cases which appear to respond significantly differently. A similar trend is observed for snap through force (Figure 3.35), where the force appears independent of wire count for most cases. Again, certain cases seem to differ significantly from this trend.

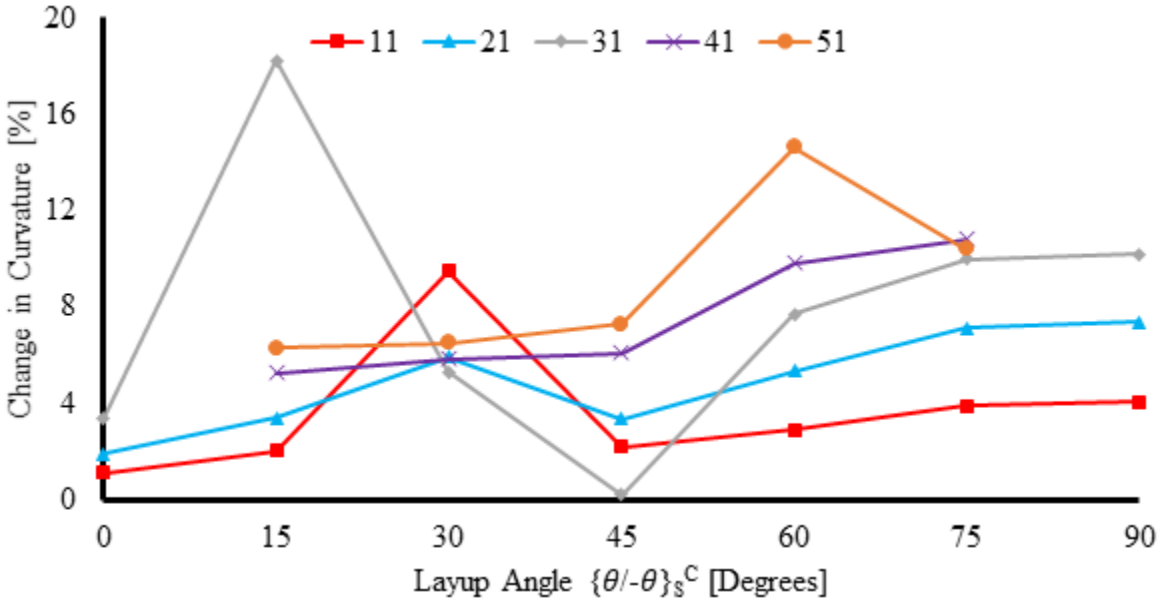

Figure 3.34 Change in Curvature vs. Layup Angle for Multiple Wire Counts and Ply Angles

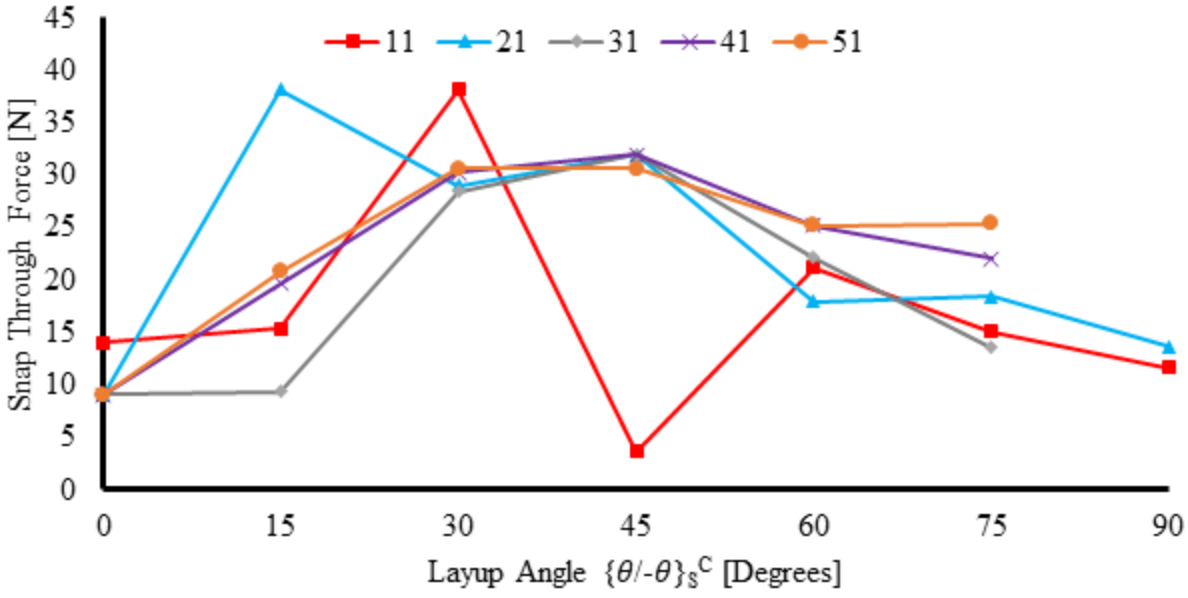

Figure 3.35 Snap Through Force vs. Layup Angle for Multiple Wire Counts and Ply Angles

To gain insight into the differences in response of these specific cases, the FE results are studied more closely for 11 wires (Figure 3.36) and 21 wires (Figure 3.37) for multiple ply angles for as-cured laminates. Take note of the primary axis of curvature, shown on each of the images. While small ply angles exhibit a 1st axis primary curvature for as cured laminates, large ply angles will cause the curvature to be dominated by the 2nd axis. An interesting case is the 21 wire $\{30/-30\}_S^C$ laminate, which is nearly flat in its as cured state. Clearly, whether the SMA wire direction (1st axis) is aligned with the primary axis of curvature will significantly affect the response of the laminate during heating and out of plane loading cases. The as-cured curvature of the laminate then, is sensitive to both wire count and layup, which effects laminate response.

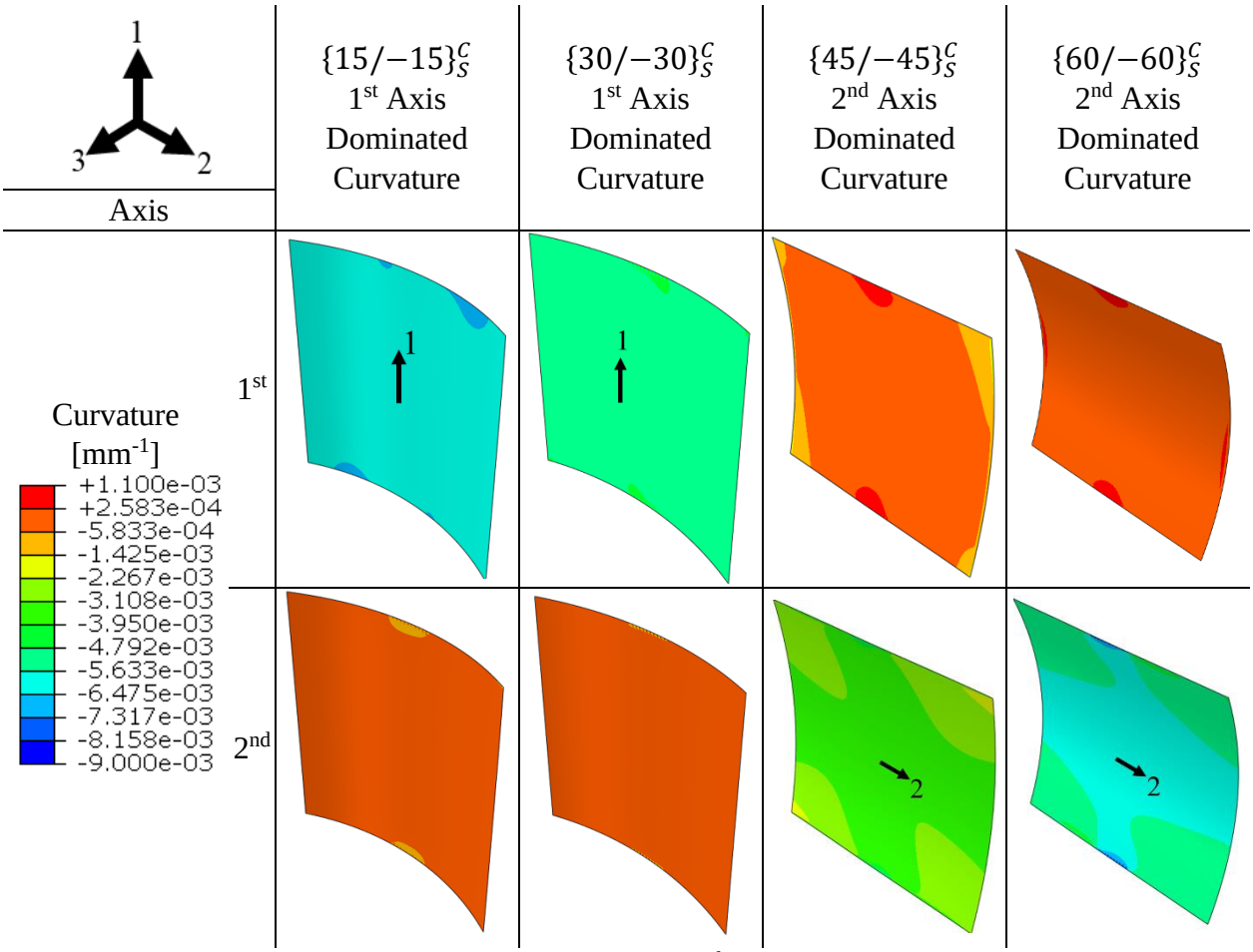

Figure 3.36 End of Step 1 Curvatures about 1st & 2nd Axis for 11 Wires with Ply Angles from 15° to 60°

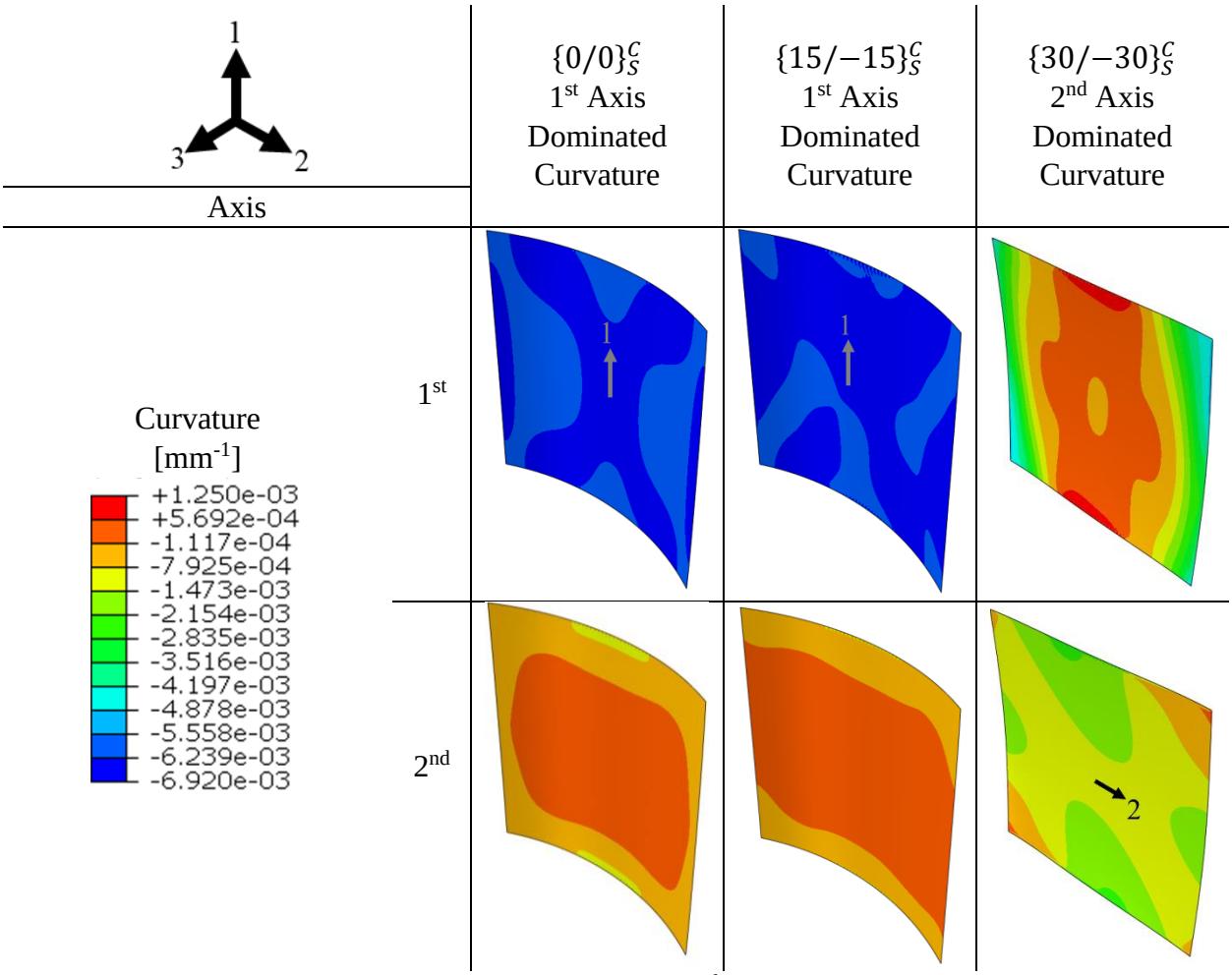

Figure 3.37 End of Step 1 Curvatures about 1st & 2nd Axis for 21 Wire Count Layup from 0° to 30° Plies

The key observation in this parametric study is that the wire count and ply angle influence the orientation of the primary axis of curvature. The alignment of this laminate's primary axis to the primary axis of curvature is shown to significantly effect the response. It is also observed that there is a non-linear coupling of wire count and ply angle for as-cured curvature.

3.3.6. Finite Element Parametric Study of Cure Temperature & SMA Prestrain

The final parametric study investigates the coupling of relative cure temperature[7] and prestrain of the SMA wires. Both of which are variables controllable during manufacturing which will affect the residual stresses in the laminate. The initial curvature for all prestrains appear to vary linearly with cure temperature, which is expected as the laminate residual stress will vary linear with temperature as well due to CTE.

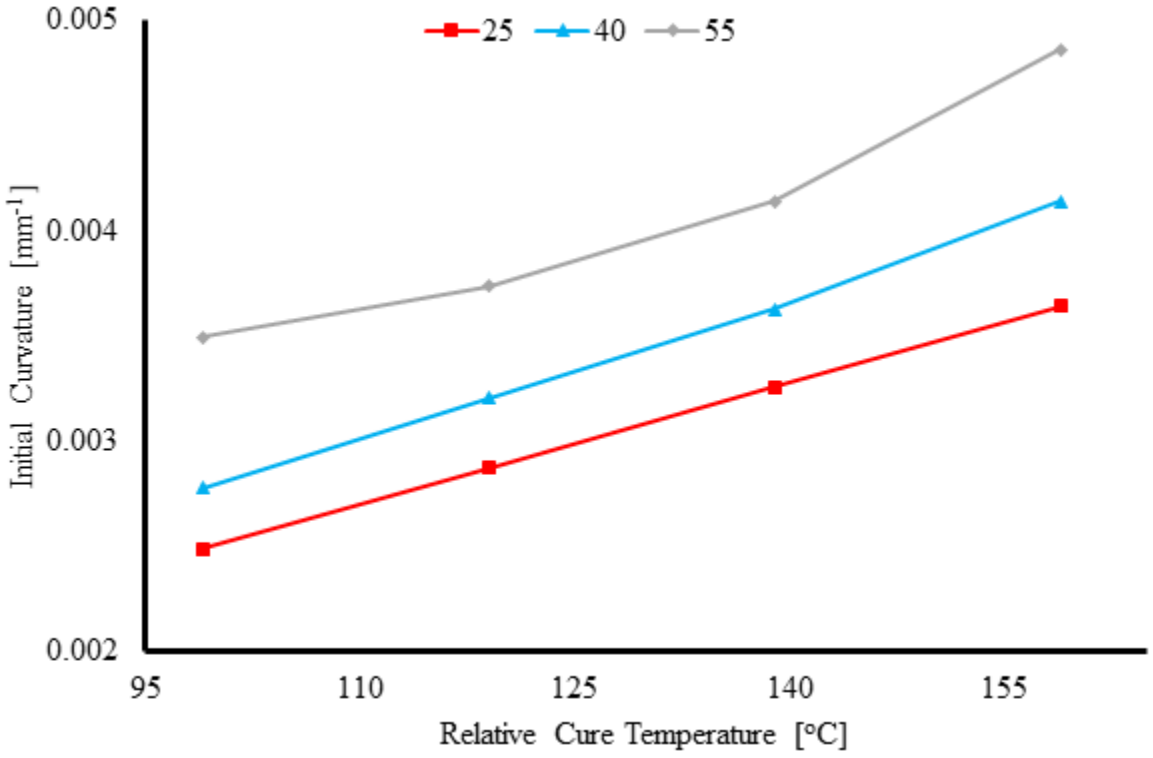

Figure 3.38 Initial Curvature vs. Relative Cure Temperature for Multiple Prestrains

[7] Note that all temperatures in this section are presented as relative according to Eqn. 3.3.

For change in curvature during SMA heating for laminates cured at or below 139 [°C], lower cure temperatures decrease the amount of possible curvature change. It appears that at 159 [°C] cure temperatures for 40 and 55 [mε] laminates the trend flips, and more change in curvature is possible. A similar trend is observable in **Section 3.3.5**, where laminates with more initial curvature tend to have a greater change in curvature during heating. This is likely because of the different mechanics governing curved structures from flatter ones amplifying effect of SMA actuation stresses. This indicates again that the as-cured shape can significantly affect the impact of the SMA wires.

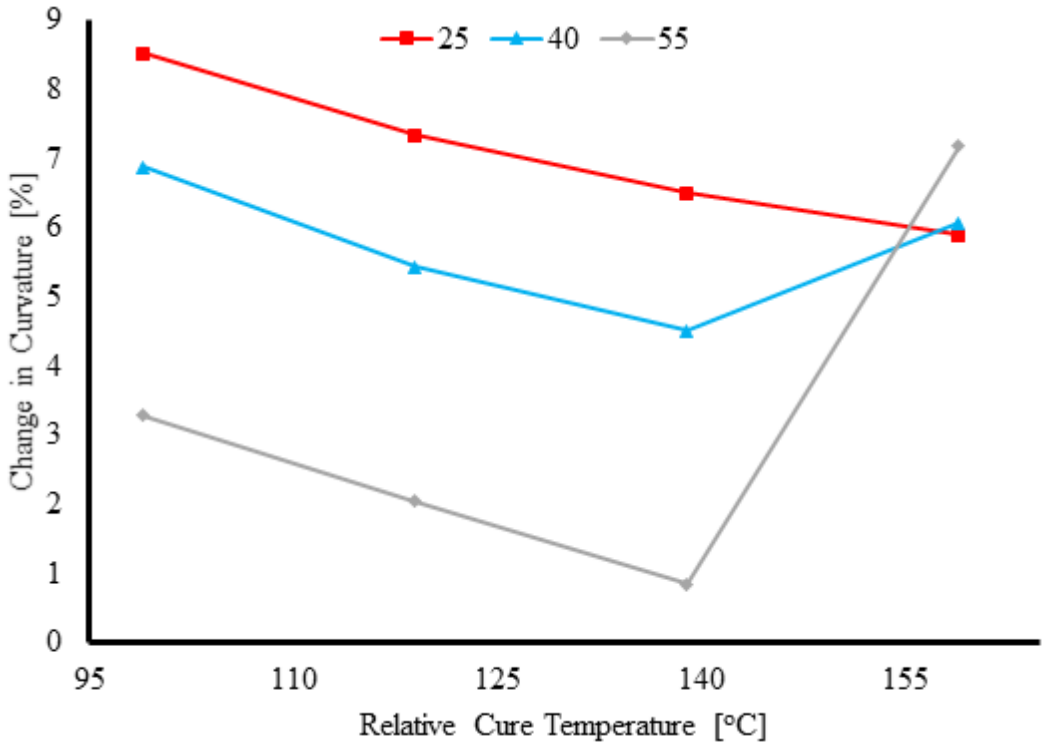

Figure 3.39 Change in Curvature vs. Relative Cure Temperature for Multiple SMA Prestrains

The snap through force, shown in Figure 3.40 displays yet another interesting trend. Of all the tests, the only example which demonstrated actual snap through behaviour is the 40 [mε] and 159 [ºC] case. The 55 [mε] and 159 [ºC] case exhibited a stiff response with local instabilities at the point of force application which may not be realistic. The other cases exhibited non-linear-elastic responses, but no instabilities like snap through behaviour. Snap through is known to be sensitive to variables such as material properties and cure temperature. This result highlights just how sensitive, as only the "perfect storm" will allow it.

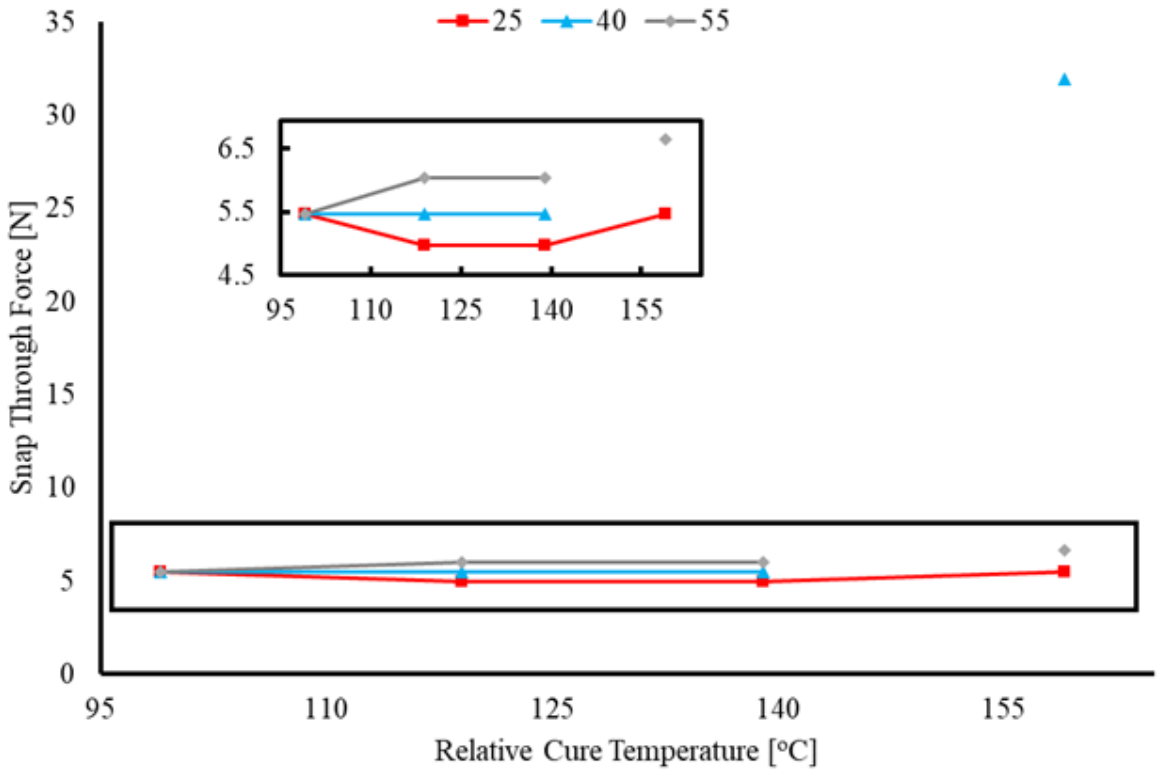

Figure 3.40 Snap Through Force vs. Relative Cure Temperature for Multiple SMA Prestrains

Cure temperature and prestrain are shown to have significant coupling and effects on the as cured shape, [%] change in curvature, and out-of-plane loading behaviours of SMAHCs. Only one of these cases exhibits a bistable behaviour. These parameters are key for varying the behaviours of SMAHCs and can be controlled to exhibit certain responses. The use of cure temperature to change response is particularly interesting, as even once the laminate is defined, the cure cycle can be adjusted to fine tune the final response.

3.4. Summary of SMAHC Finite Element Modelling

In this section a novel finite element model for Shape Memory Alloy Hybrid Composites is developed using commercially available tools in ABAQUS. This model includes key features of SMAHCs, such as prestraining, composite layups, and unidirectional superelasticity. The model begins with unsymmetric FRP composites, lessons from which are used in the evaluation of SMAHCs. A parametric study which evaluated the effect of ply angle for symmetric stacks, wire count, SMA prestrain, cure temperature, wire density, and aspect ratio is performed. To summarize the results of the parametric study:

1) Aspect ratio is shown to effect whether the laminate undergoes a buckling response and the mode of the response to out of plane loads. The possible change in curvature is also affected by aspect ratio, demonstrating the sensitivity to geometry as well.
2) In the coupled study of wire count and ply angle, it is observed that largely speaking snap through behaviour is independent of wire count, except for cases where the primary axis of the cured shape changes as a result of specific wire count and layup combinations.
3) Cure temperature and prestrain are shown to affect the as-cured shape, change in curvature, and snap through behaviour in a coupled manner.

The parametric study demonstrates how sensitive the response of SMAHCs are to subtle changes in parameters, and the coupling of these parameters. Practically speaking, this means that a robust understanding of the load case and manufacturing process is required to model SMAHC behaviour accurately, and experimentation is required to validate simulation results.

4. Preliminary Investigation into SMAHC Manufacturing

4.1. Introduction

The manufacturing of SMA hybrid composites is largely academic currently, which limits the usefulness and applicability of these techniques to industrial settings. The goal of this section is to review current techniques to inform the design of a new apparatus which solves issues. The design of a new apparatus is summarized (not as a complete design report[8]). This is a preliminary work intended to lay the groundwork for in depth future SMAHC manufacturing.

4.1.1. Types of SMA Hybrid Composites

Generally speaking, there are three categories for processing of SMAHCs, unstrained (at any temperature) and strained while processed below the M_f or above the A_f (see Table 4.1). Each of combination of these conditions yields unique mechanical responses with varying challenges.

The first category, SMAHCs with unstrained SMAs (herein referred to as UHCs for ***u**nstrained **h**ybrid **c**omposites*) do not provide the ability to create actuated structures. UHCs can be used to improve impact damage tolerance [17], [118]. These structures can be manufactured relatively simply, as they just involve attaching SMAs to composites, with no special considerations for wire prestrain.

Secondly, are composites where processing is done below the SMA's M_f while prestrained (herein referred to as SLHCs for *pre**s**trained **l**ow-temperature **h**ybrid **c**omposites*), a technique comprehensively studied by [110]. Others have used this technique include [119]–[123]. This process allows SMAs to be prestrained then co-molded with or bonded to the composite while still in the shape memory regime. This removes the need for fixtures which maintain prestrain during cure. However, fixtures are still required for initially prestraining SMAs and positioning them during cure, especially for co-molding and LCM processes as compaction and flow can cause SMA movement. Designing SLHCs involves consideration to ensure matrix performance will not degrade at temperatures at which the wire will be activated (i.e. $T_{Glass} > A_f$ while $T_{Gel} < M_f$). The thermal compatibility of SMAs and matrix limits the possibilities for SLHCs.

[8] More detailed design information for the fixture but was not included in this thesis due to relevancy and maximum thesis length. Please contact the author for more information directly.

The last option is processing the composite above the SMA's A_f while strained (herein referred to as SHHCs for *pre**s**trained **h**igh-temperature **h**ybrid **c**omposites*). SHHCs are the most complex to manufacture from a fixture perspective, as the mold must maintain wire position and prestrain at elevated temperatures (in the superelastic regime). The trade-off is that since the SMAs are constrained, any matrix can be used (i.e. $T_{Gel} > A_f$). This allows the use of any composite and SMA wire combination. A fixture which restrains the wires during the curing process is required, and can add considerable complexity as in [124].

Table 4.1 Summary of SMAHC Manufacturing Techniques

Gelation Temperature (T_{Gel})	**Unstrained**	**Strained**
$<M_f$	- No actuation - Any cure cycle possible - Easiest to manufacture	- Actuation possible - Low temperature or multi-step cure cycles - Limited SMA–Matrix pairs - Reduced custom fixtures
$>A_f$		- Actuation possible - Costly custom fixtures - Many material combinations

4.1.2. SMA – Epoxy Interface

A significant consideration when manufacturing SMAHCs is the SMA-matrix interfacial bonding strength (see [10], [110], [125]–[131]). This is not studied for this work, as Kirkby [110] showed that the interfacial strength for the NiTiCu wire used in this work is sufficient. For other SMA-Matrix combinations, this interface must be evaluated prior to further development.

4.1.3. Electrical Isolation of SMAs in SMAHCs

There are three key components to manufacturing of SMAHCs. The purposes of the first two, the SMAs and the FRP substrate are clear. The third component, the electrical isolation layer, is less clear in purpose but essential to the successful manufacturing of actuatable SMAHCs.

The electrically conductive properties of carbon fibres are known [132], which is especially of interest in corrosion applications [133]. SMAs are also electrically conductive. Given the possibility for galvanic corrosion to occur, as well as the need to control SMAs using electrical current, it's important that the SMAs are electrically insulated from the carbon fibres. The electrical resistivity of an epoxy matrix is on the order of 10^{10} [Ω mm] [134], while FRPs and SMAs are on the order of 10^{0} [Ω mm] [59], [134]. That they are on similar orders indicates that current will readily flow from SMAs to carbon fibres in direct contact. The effective resistance of the matrix between the SMA and the carbon fibres will vary linearly with the distance between them, as the epoxy is an insulator. Assuming the actuation voltages are on the order of 100 [V], and the current leakage is desired to be on the order of [mA/m], the SMA must remain approximately 100 [mm] (i.e. one ply thickness) away from the fibres. Therefore, each SMA ply is approximately twice the thickness of a traditional UD CFRP tape. This, of course, is going to vary significantly with material properties and actuation voltages but gives a sense of scale when dealing with minimum SMA wire insulation thicknesses.

It is clear that any consolidation pressure applied to SMA composites will cause the SMA to come into close proximity, and likely contact, with the carbon fibres (see microscopy from [135] and [136]) which will cause electrical contact issues. Herein lies the purpose goal of the electrical isolation layer, to prevent contact of the SMA and carbon fibres to minimize current leakage.

There are several ways to provide electrical isolation. For this work, a fibre glass veil and an adhesive are used, as shown in Figure 4.1. The fibre glass veil and epoxy adhesive promote a uniform resin rich region near the SMA wires. This serves two purposes, first is to ensure the SMA is well molded into the composite. The second is to ensure the carbon fibres and SMAs remain separated. The thicker this resin layer, the better the electrical isolation but worse the mechanical properties.

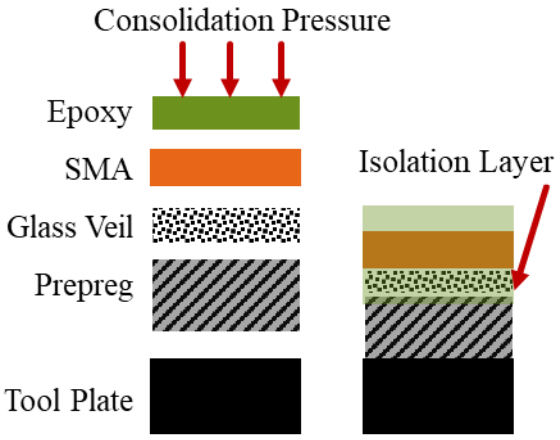

Figure 4.1 SMAHC Layup with Glass Veil for Electrical Isolation of SMA from CFRP

4.1.3.2. Electrical Isolation Testing

A rudimentary check is used to evaluate the electrical isolation of the panels, a schematic of which Figure 4.2. A DC voltage is applied to one end of a single wire using a Keithley 6221 power supply. A Keithley 2701 digital multimeter (DMM) is used to measure the current running through the circuit when the lead is applied to different SMA wires. This method identifies if two wires are in contact with the carbon fibre, so it must be repeated for all wire combinations. The positive terminal is fixed each wire, and the current is measured across each wire, with the number of wires being (N), the number of measurements required is N^2. The DMM is capable of measuring signals on the order of [nA] [137], ensuring a useful measurement can be made.

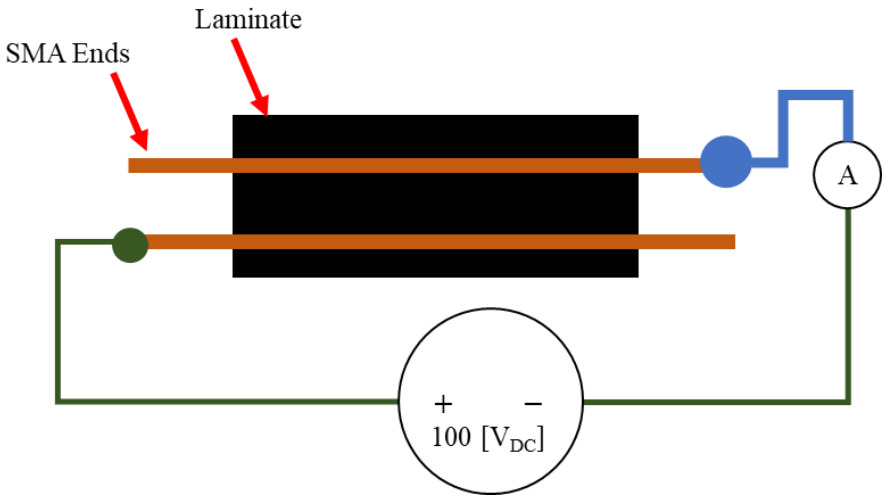

Figure 4.2 Schematic of Electrical Isolation Test

4.2. Existing Manufacturing Fixtures

SHHCs, though the most technically complex, is the most attractive as it allows readily available high-performance prepreg composites to be used. Firstly, this allows for precise ply orientation control offered by unidirectional prepregs – useful in elastically tailored structures. Secondly, using prepregs enables the use of existing processing techniques and infrastructure, such as autoclaves and ovens, allowing SHHCs to be more easily implemented. It's worth noting that similar equipment is required to position the wires for SMAHCs cured above A_f and below M_f, so the SLHCs don't allow for simpler tooling if wire-placement-precision is important.

The work on manufacturing SHHCs is limited, even in academia. Turner et. Al. [138] use a tensile machine to apply prestrain and clamp the SMA ribbon to restrain it during cure. Another approach, used in fixtures including those at EPFL [139] and at Loughborough University [140] uses the same fixture to prestrain SMA wires and restrain them during cure. The EPFL fixture (see Figure 4.3) uses wire-EDM cut combs to position the wires, enabling a high wire density of 500 [mm] between wires. Notable issues with both fixtures are the abilities to control SMA prestrain magnitude and equality, as well as the fact that they are both intended for use with cast resin systems. Controlling wire prestrain precisely is central to producing SMAHCs and must be improved upon in future work. Hebda et. Al. [141] show void agglomeration around SMAs can be reduced by autoclave processing, so a fixture which enables the application of consolidation pressure (i.e. a vacuum bag or autoclave) is also an important improvement to be made.

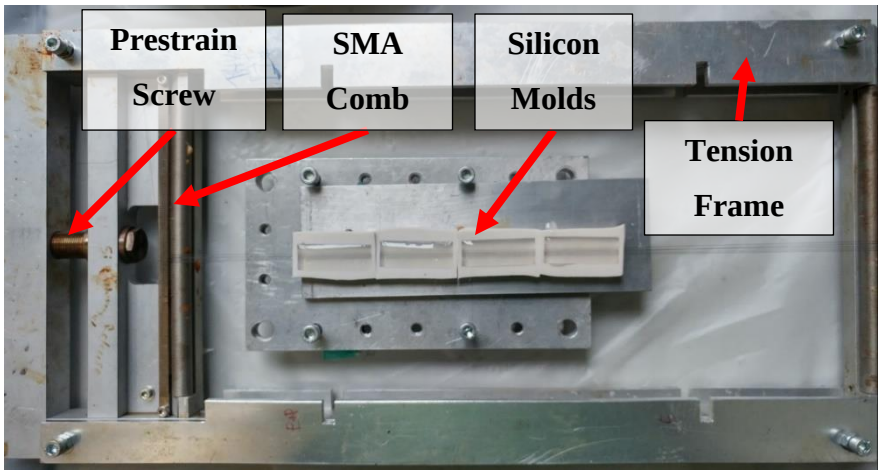

Figure 4.3 EPFL SMAHC Manufacturing Frame

4.3. New Manufacturing Fixture

The newly developed manufacturing fixture is shown in Figure 4.4. This fixture is designed to be used with vacuum bagging and out-of-autoclave prepregs and can be subject to temperatures as high as 260 [^{o}C] and allows the possibility for use with an autoclave. The key features of this fixture are:

1) The ACME lead screw for accurate and precise prestraining of the SMA wires
2) Custom 7075 aluminum combs for restraining SMA wires during cure with up to 80 wires 2 [mm/wire] spacing.
3) Combs are 2 [mm] deep, allowing layering of SMA wires as desired.
4) Combs have a 2 [mm] diameter round to allow for self-balancing tension between wires
5) An A2 steel tool plate with integrated vacuum ports to manufacture 250 x 250 [mm] panels
6) A custom die set with ball bearings to maintain smooth operation and rigidity
7) Custom brackets to precisely align the tool plate with the die set and SMA combs
8) A load cell for precisely measuring SMA preload up to 100 [kgf] total

This fixture solves several of the key issues with the EPFL fixture and enables the manufacturing of SMAHCs.

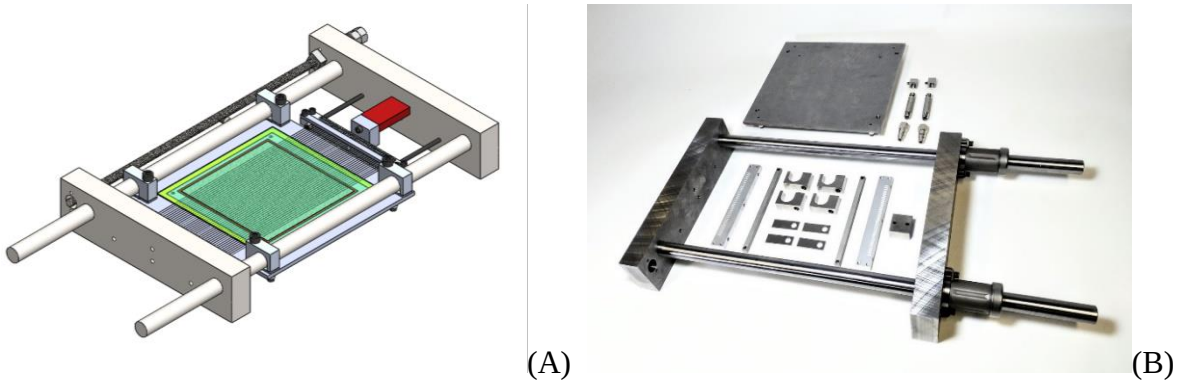

(A) (B)

Figure 4.4 SMAHC Manufacturing Fixture CAD (A) and Parts (B)

4.4. Test Panel

The purpose of manufacturing test panels for this work is to confirm the fixture functionality as well as confirming the electrical isolation of the wires. An extensive experimental series is not conducted and is considered future work. Panels are manufactured using Stabilized NiTiCu1, NCT-301 matrix, and 34-700 fibre. Either Owens Corning M524-C64 [142] glass veil and FM300-2U [143] film or with Vivian Regina Fibasil Genmat 12 [mil] [144] glass veil and FM300U [145] film. Both Fibasil and Owens-Corning glass veils use C-Glass with areal weights of 30 [gsm], and similar binder contents, fibre diameter are 16 [mm] and 12.5 [mm] for Fibasil and Owens Corning respectively. A total of four panels were manufactured, however only two tests are discussed. For more information about manufacturing see A-4 SMAHC Panel Manufacturing Process

The second test panel, shown in Figure 4.5, is a proof of concept to demonstrate the electrical isolation of the laminate using the technique described in **Section 4.1.3.2**. No non-zero measurements were made for amperage, indicating that the glass-veil and epoxy separation technique worked correctly. Note the void agglomeration around the SMA wire (consistent with observations by Hebda et. Al. [141]), and wicking of epoxy along the SMA wires. This first panel confirms the utility of the manufacturing fixture in maintaining SMA wire position as well as electrical isolation of the adhesive-glass veil approach.

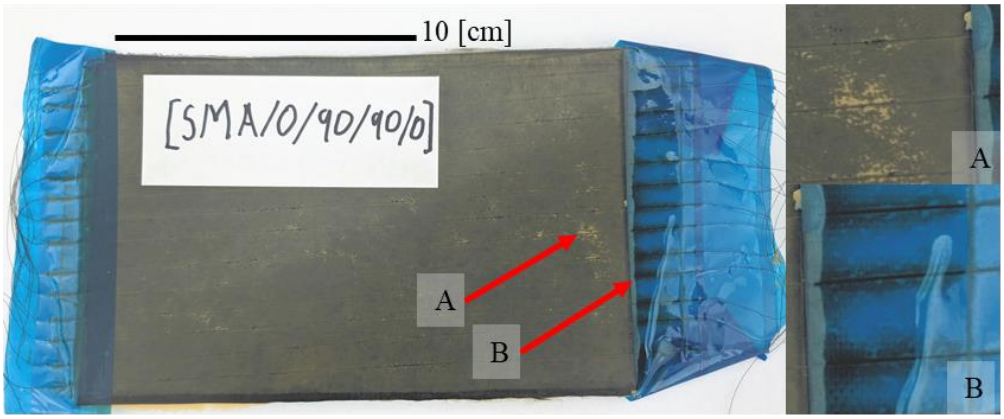

Figure 4.5 Test Panel 2 – Stabilized NiTiCu1 and FM300-2U with NCT-301 Matrix, 34-700 Fibre, and Owens Corning M524-C64 Glass Veil cured using the cycle from [146]. A wire spacing of 4 [mm/wire] is used Detail A showing void agglomeration around SMA and Detail B showing epoxy wicking along SMA.

The fourth test panel was made with the omission of the heated blankets, a greater wire density (2 [mm/wire]) using Vivian Regina Fibasil Genmat 12 [mil] glass veil and FM300U adhesive film. No non-zero measurements were made for amperage, indicating that the glass-veil and epoxy separation technique worked correctly again. There are dry spots where wrinkling in the release film occurred, as well as significant void formation on the right edge of the part. There are also noticeable ridges on this part between the SMA wires. This is likely because no heating blanket – a silicone sheet – was not used for this sample. The heating blanket acts as soft-caul plate which promotes a smooth pressure distribution and prevents release film wrinkling. For panels it is recommended that a smooth soft caul plate is used to prevent ridges between the wires. It's possible a second layer of glass veil on top of the wires would prevent these ridges as well. The difference in resin distribution is likely attributable to the fact that the FM300U was cured at 135 [^{o}C] well below its nominal of 177 [^{o}C].

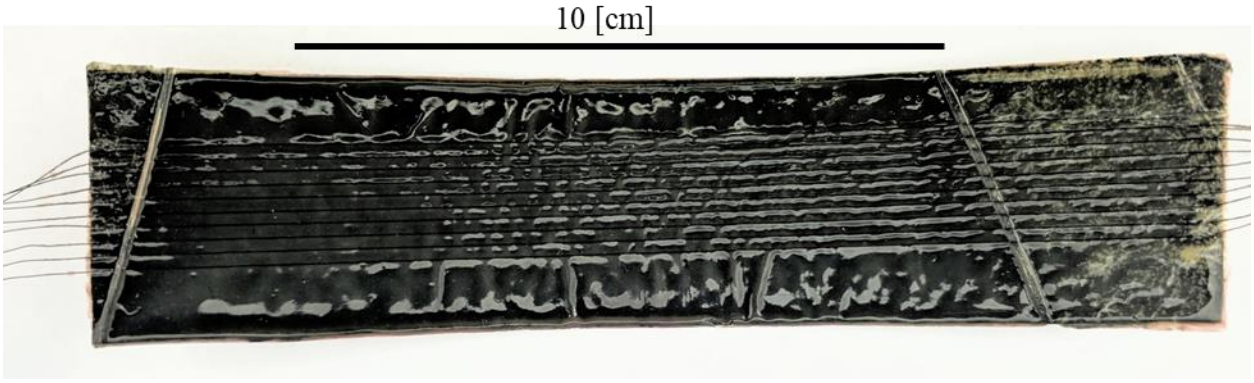

Figure 4.6 Test Panel 4 – Stabilized NiTiCu1 and FM300U with NCT-301 Matrix, 34-700 Fibre, and Vivian Regina Fibasil Genmat 12 [mil] Glass Veil cured using the cycle from [146].

The materials used in this manufacturing process were largely defined by what was available at low cost. In future work, it's suggested that the prepreg, adhesive, and glass veil used are carefully selected for compatibility and characterized. A small fibre, very low GSM surfacing veil is important (Owens Corning M524-C64 appears to be a good candidate). Prepregs and adhesives with a low temperature cures, a maximum of 135 [^{o}C] but ideally lower, are recommended as well. Furthermore, a semi-rigid (i.e. silicone or similar) caul sheet is recommended to improve surface quality of the manufactured part.

5. Conclusions

The goal of this work is to use modern, commercially available tools to develop morphing shape memory alloy hybrid composites in pursuit of morphing composite structures. During the characterization of shape memory alloys, it was observed that functional stabilization and its inclusion in all aspects of SMAHCs is critical. The 70 [%] changes in material properties and narrowing of the suitable thermal actuation window due to the increase in A_f will have significant effect on SMAHC behaviour and viability of the design. In studying the electrical behaviour, correlations between resistivity, tensile loading, and functional stabilization are observed. Though experiments are limited, it was confirmed that the proposed layup provides enough electrical isolation to allow for Joule heating of SMAs in the laminate.

The SMA characterization resulted in key findings in terms of end use applications. Firstly, it's critical that the A_f and useful actuation range is below the T_{Glass} of the composite structure. Secondly, due to the sensitivity of the plateau stresses to temperature (on the order of [MPa/^{o}C]), for a structure to behave predictably the SMA temperature must be controlled, which can be done conveniently through Joule heating. This requirement may preclude the design of passive systems, limiting the applicability to systems where temperature is controlled to be isothermal (semi-passive) or active SMA systems. It is important to select materials which are compatible, such as composites with a low T_{Gel} and a high T_{Glass}, to manufacture SMAHCs.

A new finite element modelling technique for the simulation of SMA and SMA-hybrid composites is also developed and used to execute a parametric study of SMAHC design variables. It is observed that the ability to change shape and response to external load is highly coupled amongst all factors effecting SMAHCs. Despite the complexity of these results, they can be summarized using the *Longitudinal Net Actuation Stress* ($\sigma_{11}^{Net\ Act.}$ in Eqn. 5.1) and the *Longitudinal Structural Stiffness* (K_{11} in Eqn. 5.4) as in Figure 5.2. The Longitudinal Net Actuation Stress is the amount of actuation available to the structure in the SMA wire direction, when accounting for SMAHC design variables and materials, stresses introduced by processing the SMAHC, and stresses from external loads. The Longitudinal Structural Stiffness is the stiffness of the structure in the direction of the SMA wire, including variables such as layup, size, and aspect ratio.

Structures with enough actuation stress will self-yield (left of graph). Very stiff structures are un-actuatable (top of graph). An interesting class of structures are Net-Zero Structures (right of graph), where actuation stress balances the processing and external loads, allowing zero stress even at low stiffnesses. This class of structures is interesting for applications like satellite dishes and composite tooling where precise geometry is important, a cleverly designed SMAHC can allow for the shape to remain unchanged despite external loads.

For structures where actuation is desired, the direction of desired actuation compared to the external loads and directions of stiffness are critical the suitability of SMAHCs for morphing. The case of typical hydrofoils or aerofoils where, due to their high geometric aspect ratio, the chordwise external stress is significantly smaller than the spanwise external stress. Again, due to the aspect ratios, the spanwise direction is likely to be less stiff than the chordwise. By using the ratios of external stress to stiffness (i.e. strain) in the longitudinal and transverse directions, the viability of high-aspect aspect ratio morphing structure can be evaluated. Longitudinally load bearing structures (i.e. SMA aligned with external stress) will typically allow only small actuation strains. Transversely loaded structures (i.e. SMA aligned with zero external stress direction) are prime candidates for morphing as actuation is in their softest direction, allowing high actuation strains. If it is decided that potential actuation magnitudes and directions are useful, a detailed analysis should be performed. Within these two outer limits of high principal strain gradients lies the more general category of morphing structures, where one must carefully inspect the principal strain directions due to loading and the desired actuation directions to design an efficient SMAHC.

Several challenges associated with the characterization, modelling, and, manufacturing of morphing SMAHCs were addressed and solved in this work. While there is significant work to be done prior to commercialization, there is now a clearer path to the challenges which need to be solved and some additional tools to addressing them.

Eqn. 5.1. Longitudinal Net Actuation Stress

$$\sigma_{11}^{Net\ Actuation} = \sigma_{11}^{Actuation} - \sigma_{11}^{Processing} - \sigma_{11}^{External\ Load}$$

Eqn. 5.2. Longitudinal Actuation Stress

$$\sigma_{11}^{Actuation} = f\left(Materials, Wire\ Density,\ Prestrain,\ A_f,\ T_{Max},\ Number\ of\ Wires, R_{SMA}\right)$$

Eqn. 5.3. Longitudinal Processing Stress

$$\sigma_{11}^{Processing} = f\left(Materials, T_{Gel},\ T_{Operation}, Layup\right)$$

Eqn. 5.4. Longitudinal Structural Stiffness

$$K_{11} = f(Materials, Aspect\ Ratio,\ Size,\ Layup)$$

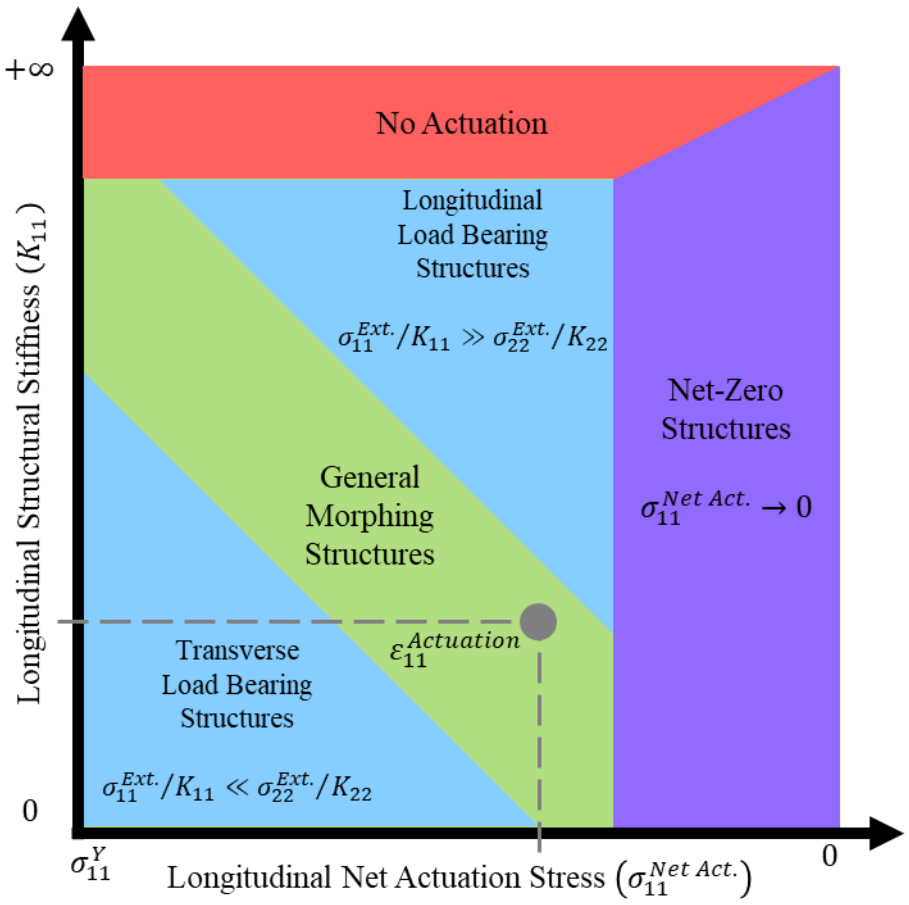

Figure 5.2 Design Regions for Morphing SMAHC Structures

5.2. Future Work

While several questions were answered in this thesis, it opened several new ones related to all aspects covered. Recommended avenues of future work are below.

- A lack of techniques to functionally stabilize large batches of SMA wire prior is a key barrier of further SMAHC research & commercialization. These techniques and apparatus must be further developed. This is currently being worked by the author (Sanesh Iyer) and Prof. Pascal Hubert who are supervising several students.
- There is a complete lack of research in the literature which tests SMA-Epoxy interfacial strength – both in terms of yield and fatigue – using stabilized SMA samples. Given TRIP and Poisson's effects, it's expected that there will be a significant effect. This should be done using pretrained high-temperature cured SMA composites to ensure test applicability.
- Extended work studying the interfacial strength of SMAs in SMAHCs is recommended, as the glass veil and processing techniques are likely to affect the interface.
- The literature is nearly devoid of work studying the Poisson's Ratio of SMAs experimentally, and values are often assumed. With the high range of reported values and the SMA phase change under loading, an understanding of Poisson's effects is key to future development.
- Further development is required to improve electrical contact of the DMA thermo-electro-mechanical fixture and characterizing. This should also include refined Poisson's Ratio measurements.
- Improvements to superelasticity models, including potentially a coupled molecular dynamic simulation (MDS) and macro-model.
- Further work is required to manufacture more panels and validate the finite element model. This is dependent on the ability to functionally stabilize greater lengths of SMA wire.
- Development of experimental techniques to measure the performance of SMAHC test panels using appropriately accurate measuring equipment.
- The use of shaped molds to both prestrain the wire and serve as a form for a composite part should be investigated.

6. References

[1] "Chapter 6: Innovating Clean Energy Technologies in Advanced Manufacturing Technology Assessments, Composite Materials," United States Department of Energy, 2015.

[2] "The markets: Aerospace (2019)." [Online]. Available: https://www.compositesworld.com/blog/post/the-markets-aerospace. [Accessed: 26-May-2019].

[3] "The markets: Automotive (2019)." [Online]. Available: https://www.compositesworld.com/blog/post/the-markets-automotive. [Accessed: 26-May-2019].

[4] "Wind/Energy Composites : CompositesWorld." [Online]. Available: https://www.compositesworld.com/zones/wind-energy-composites. [Accessed: 26-May-2019].

[5] "Boeing 787: By Design Advanced Composite Use." [Online]. Available: https://www.boeing.com/commercial/787/by-design/#/advanced-composite-use. [Accessed: 26-May-2019].

[6] L. Mishnaevsky, K. Branner, H. N. Petersen, J. Beauson, M. McGugan, and B. F. Sørensen, "Materials for Wind Turbine Blades: An Overview," *Materials*, vol. 10, no. 11, Nov. 2017, doi: 10.3390/ma10111285.

[7] "FACT SHEET: President Obama Announces New Manufacturing Innovation Hub in Knoxville, Tennessee," *whitehouse.gov*, 09-Jan-2015. [Online]. Available: https://obamawhitehouse.archives.gov/the-press-office/2015/01/09/fact-sheet-president-obama-announces-new-manufacturing-innovation-hub-kn. [Accessed: 26-May-2019].

[8] Y. Swolfs, I. Verpoest, and L. Gorbatikh, "Recent advances in fibre-hybrid composites: materials selection, opportunities and applications," *Int. Mater. Rev.*, vol. 64, no. 4, pp. 181–215, May 2019, doi: 10.1080/09506608.2018.1467365.

[9] "Hybrid composite materials: tailoring for specific performance." [Online]. Available: https://www.compositesworld.com/blog/post/hybrid-composites-tailoring-for-specific-performance-. [Accessed: 26-May-2019].

[10] B. T. Lester, T. Baxevanis, Y. Chemisky, and D. C. Lagoudas, "Review and perspectives: shape memory alloy composite systems," *Acta Mech.*, vol. 226, no. 12, pp. 3907–3960, 2015.

[11] S. Rana, S. P, R. Fangueiro, A. Gomes Correia, and 1 Fibrous Materials Research Group, University of Minho, Campus de Azurém, 4800-058 Guimarães, Portugal, "A review on smart self-sensing composite materials for civil engineering applications," *AIMS Mater. Sci.*, vol. 3, no. 2, pp. 357–379, 2016, doi: 10.3934/matersci.2016.2.357.

[12] "Hybrid Fiber Optic Sensor System for Measuring the Strain, Temperature, and Thermal Strain of Composite Materials - IEEE Journals & Magazine." [Online]. Available: https://ieeexplore.ieee.org/abstract/document/6744626. [Accessed: 26-May-2019].

[13] F. Calkins, G. Butler, and J. Mabe, "Variable geometry chevrons for jet noise reduction," presented at the 12th AIAA/CEAS Aeroacoustics Conference (27th AIAA Aeroacoustics Conference), 2006, p. 2546.

[14] W. K. Wilkie and W. K. Belvin, "AEROELASTIC ANALYSIS OF HELICOPTER ROTOR BLADES INCORPORATING ANISOTROPIC PIEZOELECTRIC TWIST ACTUATION," p. 11.

[15] B. L. Giuntoli, "Design and validation of a non-linear passive-selective compliant hydrofoil using shape-memory alloys," masters, École de technologie supérieure, 2017.

[16] K. Ikuta, “Micro/miniature shape memory alloy actuator,” in , *IEEE International Conference on Robotics and Automation Proceedings*, 1990, pp. 2156–2161 vol.3, doi: 10.1109/ROBOT.1990.126323.
[17] R. L. Ellis, F. Lalande, H. Jia, and C. A. Rogers, “Ballistic Impact Resistance of SMA and Spectra Hybrid Graphite Composites,” *J. Reinf. Plast. Compos.*, vol. 17, no. 2, pp. 147–164, Jan. 1998, doi: 10.1177/073168449801700205.
[18] A. Cohades, N. Hostettler, M. Pauchard, C. J. G. Plummer, and V. Michaud, “Stitched shape memory alloy wires enhance damage recovery in self-healing fibre-reinforced polymer composites,” *Compos. Sci. Technol.*, vol. 161, pp. 22–31, Jun. 2018, doi: 10.1016/j.compscitech.2018.03.040.
[19] J. E. Huber, N. A. Fleck, and M. F. Ashby, “The selection of mechanical actuators based on performance indices,” presented at the Proceedings of the Royal Society of London A: Mathematical, Physical and Engineering Sciences, 1997, vol. 453, pp. 2185–2205.
[20] M. W. Hyer, “The room-temperature shapes of four-layer unsymmetric cross-ply laminates,” *J. Compos. Mater.*, vol. 16, pp. 318–340, 1982.
[21] F. Mattioni, P. M. Weaver, K. D. Potter, and M. I. Friswell, “The application of thermally induced multistable composites to morphing aircraft structures,” presented at the Proc. SPIE, 2008, vol. 6930, p. 693012.
[22] “NASA - NASA’s Twist-wing Jet Explores A Radical Future.” [Online]. Available: https://www.nasa.gov/missions/research/twist_wing.html. [Accessed: 06-Nov-2019].
[23] G. Daines, “Media Usage Guidelines,” *NASA*, 11-Mar-2015. [Online]. Available: http://www.nasa.gov/multimedia/guidelines/index.html. [Accessed: 06-Nov-2019].
[24] “Morph ED01-0348-1: An artist’s rendering of the 21st Century Aerospace Vehicle, sometimes nicknamed the Morphing Airplane, shows advanced concepts NASA envisions for an aircraft of the future.” [Online]. Available: https://www.dfrc.nasa.gov/Gallery/Photo/Morph/HTML/ED01-0348-1.html. [Accessed: 06-Nov-2019].
[25] M.-L. Dano, “SMA-Induced Deformations in General Unsymmetric Laminates,” Virginia Tech, 1997.
[26] J. Mohd Jani, M. Leary, A. Subic, and M. A. Gibson, “A review of shape memory alloy research, applications and opportunities,” *Mater. Des. 1980-2015*, vol. 56, pp. 1078–1113, Apr. 2014, doi: https://doi.org/10.1016/j.matdes.2013.11.084.
[27] V. Brailovski, S. Prokoshkin, P. Terriault, and F. Trochu, *Shape memory alloys: fundamentals, modeling and applications*. École de technologie supérieure, 2003.
[28] ASTM International, “ASTM F2633-13 Specification for Wrought Seamless Nickel-Titanium Shape Memory Alloy Tube for Medical Devices and Surgical Implants,” ASTM International, ASTM F2633-13.
[29] ASTM International, “ASTM F2063-18 Specification for Wrought Nickel-Titanium Shape Memory Alloys for Medical Devices and Surgical Implants,” ASTM International, ASTM F2063-18.
[30] K. Otsuka and X. Ren, “Physical metallurgy of Ti–Ni-based shape memory alloys,” *Prog. Mater. Sci.*, vol. 50, pp. 511–678, 2005.
[31] T. W. Duerig and K. Bhattacharya, “The influence of the R-phase on the superelastic behavior of NiTi,” *Shape Mem. Superelasticity*, vol. 1, pp. 153–161, 2015.
[32] “Finite Element Analysis of the Implantation of a Self-Expanding Stent: Impact of Lesion Calcification | Journal of Medical Devices | ASME DC.” [Online]. Available:

http://medicaldevices.asmedigitalcollection.asme.org/article.aspx?articleid=1451950. [Accessed: 01-Aug-2018].
[33] *Engineering Aspects of Shape Memory Alloys*. Elsevier, 1990.
[34] D. J. Hartl and D. C. Lagoudas, "Constitutive modeling and structural analysis considering simultaneous phase transformation and plastic yield in shape memory alloys," *Smart Mater. Struct.*, vol. 18, no. 10, p. 104017, Sep. 2009, doi: 10.1088/0964-1726/18/10/104017.
[35] L. C. Brinson, I. Schmidt, and R. Lammering, "Stress-induced transformation behavior of a polycrystalline NiTi shape memory alloy: micro and macromechanical investigations via in situ optical microscopy," *J. Mech. Phys. Solids*, vol. 52, pp. 1549–1571, 2004.
[36] A. L. McKelvey and R. O. Ritchie, "Fatigue-crack propagation in Nitinol, a shape-memory and superelastic endovascular stent material," *J. Biomed. Mater. Res.*, vol. 47, no. 3, pp. 301–308, Dec. 1999, doi: 10.1002/(SICI)1097-4636(19991205)47:3<301::AID-JBM3>3.0.CO;2-H.
[37] D. A. Hebda and S. R. White, "Effect of training conditions and extended thermal cycling on nitinol two-way shape memory behavior," *Smart Mater. Struct.*, vol. 4, no. 4, p. 298, 1995, doi: 10.1088/0964-1726/4/4/010.
[38] Z. Bo and D. C. Lagoudas, "Thermomechanical modeling of polycrystalline SMAs under cyclic loading, Part III: evolution of plastic strains and two-way shape memory effect," *Int. J. Eng. Sci.*, vol. 37, pp. 1175–1203, 1999.
[39] Y. Zhang, J. Zhu, Z. Moumni, A. V. Herpen, and W. Zhang, "Energy-based fatigue model for shape memory alloys including thermomechanical coupling," *Smart Mater. Struct.*, vol. 25, no. 3, p. 035042, Feb. 2016, doi: 10.1088/0964-1726/25/3/035042.
[40] D. C. Lagoudas and P. B. Entchev, "Modeling of transformation-induced plasticity and its effect on the behavior of porous shape memory alloys. Part I: constitutive model for fully dense SMAs," *Mech. Mater.*, vol. 36, no. 9, pp. 865–892, Sep. 2004, doi: 10.1016/j.mechmat.2003.08.006.
[41] G. Kang and D. Song, "Review on structural fatigue of NiTi shape memory alloys: Pure mechanical and thermo-mechanical ones," *Theor. Appl. Mech. Lett.*, vol. 5, no. 6, pp. 245–254, Nov. 2015, doi: 10.1016/j.taml.2015.11.004.
[42] F. Auricchio, S. Marfia, and E. Sacco, "Modelling of SMA materials: training and two way memory effects," *Comput. Struct.*, vol. 81, pp. 2301–2317, 2003.
[43] P. Filip and K. Mazanec, "The two way memory effect in TiNi alloys," *Scr. Mater.*, vol. 35, no. 3, 1996.
[44] D. J. Hartl and D. C. Lagoudas, "Aerospace applications of shape memory alloys," *Proc. Inst. Mech. Eng. Part G J. Aerosp. Eng.*, vol. 221, no. 4, pp. 535–552, Apr. 2007, doi: 10.1243/09544100JAERO211.
[45] G. Eggeler, E. Hornbogen, A. Yawny, A. Heckmann, and M. Wagner, "Structural and functional fatigue of NiTi shape memory alloys," *Mater. Sci. Eng. A*, vol. 378, no. 1, pp. 24–33, Jul. 2004, doi: 10.1016/j.msea.2003.10.327.
[46] L. Fumagalli, F. Butera, and A. Coda, "SmartFlex® NiTi Wires for Shape Memory Actuators," *J. Mater. Eng. Perform.*, vol. 18, no. 5, pp. 691–695, Aug. 2009, doi: 10.1007/s11665-009-9407-9.
[47] O. W. Bertacchini, D. C. Lagoudas, F. T. Calkins, and J. H. Mabe, "Thermomechanical cyclic loading and fatigue life characterization of nickel rich NiTi shape-memory alloy actuators," presented at the Behavior and Mechanics of Multifunctional and Composite Materials 2008, 2008, vol. 6929, p. 692916.

[48] E. Hornbogen, “Review Thermo-mechanical fatigue of shape memory alloys,” *J. Mater. Sci.*, vol. 39, no. 2, pp. 385–399, Jan. 2004, doi: 10.1023/B:JMSC.0000011492.88523.d3.
[49] D. C. Lagoudas, D. A. Miller, L. Rong, and P. K. Kumar, “Thermomechanical fatigue of shape memory alloys,” *Smart Mater. Struct.*, vol. 18, no. 8, p. 085021, 2009, doi: 10.1088/0964-1726/18/8/085021.
[50] G. S. Mammano and E. Dragoni, “Functional fatigue of NiTi Shape Memory wires for a range of end loadings and constraints,” *Frat. Ed Integrità Strutt.*, vol. 7, no. 23, pp. 14–33, 2013.
[51] F. Auricchio and R. L. Taylor, “Shape-memory alloys: modelling and numerical simulations of the finite-strain superelastic behavior,” *Comput. Methods Appl. Mech. Eng.*, vol. 143, no. 1–2, pp. 175–194, 1997.
[52] J. G. Boyd and D. C. Lagoudas, “A thermodynamical constitutive model for shape memory materials. Part I. The monolithic shape memory alloy,” *Int. J. Plast.*, vol. 12, pp. 805–842, 1996.
[53] ASTM International, “ASTM F2005-05 Standard Terminology for Nickel-Titanium Shape Memory Alloys,” ASTM International, Standard ASTM F2005-05.
[54] Z. Moumni, A. V. Herpen, and P. Riberty, “Fatigue analysis of shape memory alloys: energy approach,” *Smart Mater. Struct.*, vol. 14, no. 5, p. S287, 2005, doi: 10.1088/0964-1726/14/5/017.
[55] G. R. Halford, “The energy required for fatigue(Plastic strain hystersis energy required for fatigue in ferrous and nonferrous metals),” *J. Mater.*, vol. 1, pp. 3–18, 1966.
[56] C. Morin, “A comprehensive approach for fatigue analysis of shape memory alloys,” p. 150, Jul. 2011.
[57] F. R. Fickett, “Electrical properties of materials and their measurement at low temperatures,” p. 80.
[58] J. Uchil, K. P. Mohanchandra, K. G. Kumara, and K. K. Mahesh, “Study of critical dependence of stable phases in Nitinol on heat treatment using electrical resistivity probe,” *Mater. Sci. Eng. A*, vol. 251, no. 1, pp. 58–63, Aug. 1998, doi: 10.1016/S0921-5093(98)00636-4.
[59] V. Antonucci, G. Faiella, M. Giordano, F. Mennella, and L. Nicolais, “Electrical resistivity study and characterization during NiTi phase transformations,” *Thermochim. Acta*, vol. 462, no. 1, pp. 64–69, Oct. 2007, doi: 10.1016/j.tca.2007.05.024.
[60] P. Terriault, F. Viens, and V. Brailovski, “Non-isothermal finite element modeling of a shape memory alloy actuator using ANSYS,” *COMMAT Comput. Mater. Sci.*, vol. 36, pp. 397–410, 2006.
[61] L. C. Brinson and R. Lammering, “Finite element analysis of the behavior of shape memory alloys and their applications,” *Int. J. Solids Struct.*, vol. 30, pp. 3261–3280, 1993.
[62] D. C. Lagoudas, *Shape memory alloys: modeling and engineering applications*. Springer Science & Business Media, 2008.
[63] V. Evangelista, S. Marfia, and E. Sacco, “A 3D SMA constitutive model in the framework of finite strain,” *Int. J. Numer. Methods Eng.*, vol. 81, pp. 761–785, 2010.
[64] Dassault Systemes, “Superelasticity,” *SIMULIA User Assistance*, 2018. [Online]. Available: https://help.3ds.com/2018x/english/dsdoc/SIMA3DXMATRefMap/simamat-c-superelasticity.htm.
[65] MSC Software, “Marc Volume A: Theory and User Information.” MSC Software, 2017.

[66] D. J. Hartl *et al.*, “Standardization of shape memory alloy test methods toward certification of aerospace applications,” *Smart Mater. Struct.*, vol. 24, no. 8, p. 082001, 2015, doi: 10.1088/0964-1726/24/8/082001.
[67] M. L. Sahli and B. Necib, “Characterisation and modelling of behaviour of a shape memory alloys,” *Int. J. Adv. Manuf. Technol.*, vol. 70, no. 9, pp. 1847–1857, Feb. 2014, doi: 10.1007/s00170-013-5416-9.
[68] J. H. Mabe, R. T. Ruggeri, E. Rosenzweig, and C.-J. M. Yu, “NiTinol performance characterization and rotary actuator design,” in *Smart Structures and Materials 2004: Industrial and Commercial Applications of Smart Structures Technologies*, 2004, vol. 5388, pp. 95–110, doi: 10.1117/12.539008.
[69] D. Roy, V. Buravalla, P. Mangalgiri, S. Allegavi, and U. Ramamurty, “Mechanical characterization of NiTi SMA wires using a dynamic mechanical analyzer,” *Mater. Sci. Eng. A*, vol. 494, no. 1–2, pp. 429–435, 2008.
[70] M. Ho and J. P. Desai, “Characterization of SMA actuator for applications in robotic neurosurgery,” in *2009 Annual International Conference of the IEEE Engineering in Medicine and Biology Society*, 2009, pp. 6856–6859, doi: 10.1109/IEMBS.2009.5333118.
[71] ASTM International, “ASTM F2004-17 Standard Test Method for Transformation Temperature of Nickel-Titanium Alloys by Thermal Analysis,” ASTM International, Standard ASTM F2004-17, 2017.
[72] ASTM International, “ASTM F2516-18 Standard Test Method for Tension Testing of Nickel-Titanium Superelastic Materials,” ASTM International, Standard F2516-18, 2018.
[73] ASTM International, “ASTM E3098-17 Standard Test Method for Mechanical Uniaxial Pre-strain and Thermal Free Recovery of Shape Memory Alloys,” ASTM International, 2017.
[74] ASTM International, “ASTM E3097-17 Standard Test Method for Mechanical Uniaxial Constant Force Thermal Cycling of Shape Memory Alloys,” ASTM International, 2017.
[75] Furukawa Electric Europe LTD., “Quote for NiTiCu1.” Furukawa Electric Europe LTD., 11-Aug-2017.
[76] T. Kakeshita, K. Shimizu, S. Nakamichi, R. Tanaka, S. Endo, and F. Ono, “Effect of Hydrostatic Pressures on Thermoelastic Martensitic Transformations in Aged Ti–Ni and Ausaged Fe–Ni–Co–Ti Shape Memory Alloys,” *Mater. Trans. JIM*, vol. 33, no. 1, pp. 1–6, 1992, doi: 10.2320/matertrans1989.33.1.
[77] C. Tatar and Z. Yildirim, “Phase transformation kinetics and microstructure of NiTi shape memory alloy: effect of hydrostatic pressure,” *Bull. Mater. Sci.*, vol. 40, no. 4, pp. 799–803, Aug. 2017, doi: 10.1007/s12034-017-1413-1.
[78] J.-L. Wan, Z.-B. Chen, S.-J. Qin, and J.-X. Shang, “Effect of hydrostatic pressure on thermally induced phase transformation in NiTi alloy: A molecular dynamics study,” *Comput. Mater. Sci.*, vol. 153, pp. 119–125, Oct. 2018, doi: 10.1016/j.commatsci.2018.06.035.
[79] S. R. Bakhtiari, J. Z. Liu, B. S. Shariat, H. Yang, and Y. Liu, “Role of hydrostatic pressure on the phase stability, the ground state, and the transformation pathways of NiTi alloy,” *Scr. Mater.*, vol. 151, pp. 57–60, Jul. 2018, doi: 10.1016/j.scriptamat.2018.04.001.
[80] W.-S. Ko, S. B. Maisel, B. Grabowski, J. B. Jeon, and J. Neugebauer, “Atomic scale processes of phase transformations in nanocrystalline NiTi shape-memory alloys,” *Acta Mater.*, vol. 123, pp. 90–101, Jan. 2017, doi: 10.1016/j.actamat.2016.10.019.

[81] P. Chowdhury, L. Patriarca, G. Ren, and H. Sehitoglu, “Molecular dynamics modeling of NiTi superelasticity in presence of nanoprecipitates,” *Int. J. Plast.*, vol. 81, pp. 152–167, Jun. 2016, doi: 10.1016/j.ijplas.2016.01.011.
[82] B. Guyon, “Coupled Stress-Strain-Resistivity Characterization of Shape Memory Alloys for Control System,” Ecole Polytechnique Federale de Lausanne (EPFL).
[83] J. Janesch, “Two-wire vs. four-wire resistance measurements,” *EDN*. [Online]. Available: https://www.edn.com/design/test-and-measurement/4411117/Two-wire-vs--four-wire-resistance-measurements. [Accessed: 26-Aug-2019].
[84] W. D. Callister and D. G. Rethwisch, *Materials Science and Engineering: An Introduction, 9th Edition: Ninth Edition*. John Wiley and Sons, Incorporated, 2013.
[85] Muttulingam, Mayuran S., “Composites modeling with ANSYS,” 12-Oct-2011.
[86] “Analysis of Composite Materials with Abaqus.”
[87] “SIMULIA User Assistance 2018 - Linear elastic behavior.” [Online]. Available: https://help.3ds.com/2018/english/DSSIMULIA_Established/SIMACAEMATRefMap/simamat-c-linearelastic.htm. [Accessed: 19-Jul-2018].
[88] V. Birman, D. A. Saravanis, and D. A. Hopkins, “Micromechanics of composites with shape memory alloy fibers in uniform thermal fields,” *AIAA J.*, vol. 34, pp. 1905–1912, 1996.
[89] J.-H. Roh, I.-K. Oh, S.-M. Yang, J.-H. Han, and I. Lee, “Thermal post-buckling analysis of shape memory alloy hybrid composite shell panels,” *Smart Mater. Struct.*, vol. 13, no. 6, p. 1337, 2004.
[90] H. K. Cho and J. Rhee, “Nonlinear finite element analysis of shape memory alloy (SMA) wire reinforced hybrid laminate composite shells,” *Int. J. Non-Linear Mech.*, vol. 47, no. 6, pp. 672–678, Jul. 2012, doi: 10.1016/j.ijnonlinmec.2011.11.002.
[91] J.-H. Roh, K.-S. Kim, and I. Lee, “Shape adaptive airfoil actuated by a shape memory alloy and its aerodynamic characteristics,” *Mech. Adv. Mater. Struct.*, vol. 16, no. 3, pp. 260–274, 2009.
[92] H. J. Lee and J. J. Lee, “A numerical analysis of the buckling and postbuckling behavior of laminated composite shells with embedded shape memory alloy wire actuators,” *Smart Mater. Struct.*, vol. 9, no. 6, p. 780, 2000.
[93] M. W. Hyer, “Some observations on the cured shape of thin unsymmetric laminates,” *J. Compos. Mater.*, vol. 15, pp. 175–194, 1981.
[94] M. W. Hyer, “Calculations of the Room-Temperature Shapes of Unsymmetric Laminates,” *J. Compos. Mater.*, vol. 15, pp. 296–310, 1981.
[95] M. Schlecht, K. Schulte, and M. W. Hyer, “Advanced calculation of the room-temperature shapes of thin unsymmetric composite laminates,” *Compos. Struct.*, vol. 32, pp. 627–633, 1995.
[96] M.-L. Dano and M. W. Hyer, “Thermally-induced deformation behavior of unsymmetric laminates,” *Int. J. Solids Struct.*, vol. 35, pp. 2101–2120, 1998.
[97] M.-L. Dano and M. W. Hyer, “Snap-through of unsymmetric fiber-reinforced composite laminates,” *Int. J. Solids Struct.*, vol. 39, pp. 175–198, 2002.
[98] Samer Anwar Tawfik, “Stability and Morphing Characteristics of Bistable Composite Laminates,” Georgia Institute of Technology, 2008.
[99] Pedro Miguel dos Santos Carvalho Portela, “Analysis of morphing, multi-stable structures actuated by piezoelectric patches,” Universidade do Porto, 2005.
[100] Inn B Kim, “Development and Analysis of Elastically Tailored Composite Stare Shaped Beam Sections,” Georgia Institute of Technologiy, 2003.

[101] "SIMULIA User Assistance 2018 - Finite-sliding interaction between a deformable and a rigid body." [Online]. Available: https://help.3ds.com/2018/english/dssimulia_established/simacaetherefmap/simathe-c-defbodyrigidsurf.htm?contextscope=cloud. [Accessed: 25-Jul-2018].
[102] "Beam Preload | Simulation Mechanical | Autodesk Knowledge Network." [Online]. Available: https://knowledge.autodesk.com/support/simulation-mechanical/learn-explore/caas/CloudHelp/cloudhelp/2018/ENU/SimMech-UsersGuide/files/GUID-F8787ABF-3156-41A6-B9E7-EFD8AA393C5F-htm.html. [Accessed: 25-Jul-2018].
[103] "How to apply a preload to a solid bolt in Simulation Mechanical | Simulation Mechanical | Autodesk Knowledge Network." [Online]. Available: https://knowledge.autodesk.com/support/simulation-mechanical/learn-explore/caas/sfdcarticles/sfdcarticles/How-to-apply-a-preload-to-a-solid-bolt-in-Simulation-Mechanical.html. [Accessed: 25-Jul-2018].
[104] H. D. Hibbitt and J. C. Nagtegaal, "Computer process for prescribing an assembly load to provide pre-tensioning simulation in the design analysis of load-bearing structures," US5920491A, 06-Jul-1999.
[105] "37.3. Modeling." [Online]. Available: https://www.sharcnet.ca/Software/Ansys/17.0/en-us/help/ans_tec/tecboltthreadmodel.html. [Accessed: 25-Jul-2018].
[106] "PRETS179." [Online]. Available: https://www.sharcnet.ca/Software/Ansys/17.0/en-us/help/ans_elem/Hlp_E_PRETS179.html. [Accessed: 25-Jul-2018].
[107] "SIMULIA User Assistance 2018 - Prescribed Assembly Loads." [Online]. Available: https://help.3ds.com/2018/english/dssimulia_established/SIMACAEPRCRefMap/simaprc-c-pretension.htm. [Accessed: 26-Jul-2018].
[108] M. L. Blosser, "Thermal Stress in High Temperature Cylindrical Fasteners," NASA, NASA Technical Memorandum 100611, May 1988.
[109] *HexPly 8551-7 Epoxy Matrix*. Hexcel, 2016.
[110] Kirkby, Eva, "Active Sensing and Repair Composites," Docteur Es Sciences, Ecole Polytechnique Federale de Lausanne, Lausanne, Switzerland.
[111] "SIMULIA User Assistance 2018 - Choosing a beam element." [Online]. Available: https://help.3ds.com/2018/english/DSSIMULIA_Established/SIMACAEELMRefMap/simaelm-c-beamelem.htm?ContextScope=all&id=34d974cbca8b4a808953b8344f750b91#Pg0. [Accessed: 01-Aug-2018].
[112] Balta Neumann, Jose Antonio, "Adaptive Composites with Embedded Shape Memory Alloy Wires," Docteur es Sciences Techniques, Ecole Polytechnique Federale de Lausanne, Lausanne, Switzerland, 2003.
[113] M. C. Arokiaraj, G. D. Santis, M. D. Beule, and I. F. Palacios, "Finite Element Modeling of A Novel Self-Expanding Endovascular Stent Method in Treatment of Aortic Aneurysms," *Sci. Rep.*, vol. 4, p. 3630, Jan. 2014, doi: 10.1038/srep03630.
[114] G. R. Cowper, "The Shear Coefficient in Timoshenko's Beam Theory," *J. Appl. Mech.*, vol. 33, no. 2, pp. 335–340, Jun. 1966, doi: 10.1115/1.3625046.
[115] R C Hibbeler, *Mechanics of Materials*, 8th ed. Pearson, 2011.
[116] "Composite Materials for Aircraft Structures (2nd Edition) - Knovel." [Online]. Available: https://app.knovel.com/web/toc.v/cid:kpCMASE001/viewerType:toc//root_slug:composite-materials-for?kpromoter=marc&toc-within=cte%20fm300. [Accessed: 18-Mar-2019].

[117] R. Ganesan and A. Zabihollah, “Vibration analysis of tapered composite beams using a higher-order finite element. Part II: parametric study,” *Compos. Struct.*, vol. 77, no. 3, pp. 319–330, Feb. 2007, doi: 10.1016/j.compstruct.2005.07.017.

[118] K. S. C. Kuang and W. J. Cantwell, “The use of plastic optical fibres and shape memory alloys for damage assessment and damping control in composite materials,” *Meas. Sci. Technol.*, vol. 14, no. 8, pp. 1305–1313, Jul. 2003, doi: 10.1088/0957-0233/14/8/316.

[119] M.-S. Kim, W.-S. Chu, J.-H. Lee, Y.-M. Kim, and S.-H. Ahn, “Manufacturing of inchworm robot using shape memory alloy (SMA) embedded composite structure,” *Int. J. Precis. Eng. Manuf.*, vol. 12, no. 3, pp. 565–568, Jun. 2011, doi: 10.1007/s12541-011-0071-2.

[120] S. R. White and J. B. Berman, “Thermomechanical response of SMA composite beams with embedded nitinol wires in an epoxy matrix,” *J. Intell. Mater. Syst. Struct.*, vol. 9, pp. 391–400, 1998.

[121] H. Rodrigue, W. Wang, B. Bhandari, M.-W. Han, and S.-H. Ahn, “Cross-shaped twisting structure using SMA-based smart soft composite,” *Int. J. Precis. Eng. Manuf.-Green Technol.*, vol. 1, no. 2, pp. 153–156, Apr. 2014, doi: 10.1007/s40684-014-0020-5.

[122] Zafar Adeel and Andrawes Bassem, “Fabrication and Cyclic Behavior of Highly Ductile Superelastic Shape Memory Composites,” *J. Mater. Civ. Eng.*, vol. 26, no. 4, pp. 622–632, Apr. 2014, doi: 10.1061/(ASCE)MT.1943-5533.0000797.

[123] H. Rodrigue, W. Wei, B. Bhandari, and S.-H. Ahn, “Fabrication of wrist-like SMA-based actuator by double smart soft composite casting,” *Smart Mater. Struct.*, vol. 24, no. 12, p. 125003, Oct. 2015, doi: 10.1088/0964-1726/24/12/125003.

[124] “(1) (PDF) Progress on Composites with Embedded Shape Memory Alloy Wires,” *ResearchGate*. [Online]. Available: https://www.researchgate.net/publication/37436627_Progress_on_Composites_with_Embedded_Shape_Memory_Alloy_Wires. [Accessed: 12-Jun-2019].

[125] K.-T. Lau, A. W.-L. Chan, S.-Q. Shi, and L.-M. Zhou, “Debond induced by strain recovery of an embedded NiTi wire at a NiTi/epoxy interface: micro-scale observation,” *Mater. Des.*, vol. 23, no. 3, pp. 265–270, May 2002, doi: 10.1016/S0261-3069(01)00087-5.

[126] C. Poon, K. Lau, and L. Zhou, “Design of pull-out stresses for prestrained SMA wire/polymer hybrid composites,” *Compos. Part B Eng.*, vol. 36, pp. 25–31, 2005.

[127] Y. J. Zheng, L. S. Cui, and J. Schrooten, “Basic design guidelines for SMA/epoxy smart composites,” *Mater. Sci. Eng. A*, vol. 390, no. 1, pp. 139–143, Jan. 2005, doi: 10.1016/j.msea.2004.07.063.

[128] P. Bettini, M. Riva, G. Sala, L. Di Landro, A. Airoldi, and J. Cucco, “Carbon Fiber Reinforced Smart Laminates with Embedded SMA Actuators—Part I: Embedding Techniques and Interface Analysis,” *J. Mater. Eng. Perform.*, vol. 18, pp. 664–671, 2009.

[129] J. PAINE, W. JONES, and C. ROGERS, “Nitinol actuator to host composite interfacial adhesion in adaptive hybrid composites,” in *33rd Structures, Structural Dynamics and Materials Conference*, American Institute of Aeronautics and Astronautics.

[130] N. A. Smith, G. G. Antoun, A. B. Ellis, and W. C. Crone, “Improved adhesion between nickel–titanium shape memory alloy and a polymer matrix via silane coupling agents,” *Compos. Part Appl. Sci. Manuf.*, vol. 35, no. 11, pp. 1307–1312, Nov. 2004, doi: 10.1016/j.compositesa.2004.03.025.

[131] K. Jonnalagadda, G. E. Kline, and N. R. Sottos, “Local displacements and load transfer in shape memory alloy composites,” *Exp. Mech.*, vol. 37, no. 1, pp. 78–86, Mar. 1997, doi: 10.1007/BF02328753.

[132] C. N. Owston, “Electrical properties of single carbon fibres,” *J. Phys. Appl. Phys.*, vol. 3, no. 11, pp. 1615–1626, Nov. 1970, doi: 10.1088/0022-3727/3/11/309.
[133] K. J. Lodge, “The electrical properties of joints in carbon fibre composites,” *Composites*, vol. 13, no. 3, pp. 305–310, Jul. 1982, doi: 10.1016/0010-4361(82)90014-3.
[134] K. Schulte and Ch. Baron, “Load and failure analyses of CFRP laminates by means of electrical resistivity measurements,” *Compos. Sci. Technol.*, vol. 36, no. 1, pp. 63–76, Jan. 1989, doi: 10.1016/0266-3538(89)90016-X.
[135] X. Ya, K. Otsuka, N. Toyama, H. Yoshida, H. Nagai, and T. Kishi, “A novel technique for fabricating SMA/CFRP adaptive composites using ultrathin TiNi wires,” *Smart Mater. Struct.*, vol. 13, p. 196, 2004.
[136] B. K. Jang and T. Kishi, “Adhesive strength between TiNi fibers embedded in CFRP composites,” *Mater. Lett.*, vol. 59, no. 11, pp. 1338–1341, May 2005, doi: 10.1016/j.matlet.2005.01.006.
[137] K. I. Inc, “Model 2701 Ethernet-Based DMM/Data Acquisition System User’s Manual,” p. 506.
[138] T. L. Turner, C. L. Lach, and R. J. Cano, “Fabrication and characterization of SMA hybrid composites,” in *Smart Structures and Materials 2001: Active Materials: Behavior and Mechanics*, 2001, vol. 4333, pp. 343–354, doi: 10.1117/12.432774.
[139] V. Michaud, “Can shape memory alloy composites be smart?,” *Scr. Mater.*, vol. 50, pp. 249–253, 2004.
[140] G. Zhou and P. Lloyd, “Design, manufacture and evaluation of bending behaviour of composite beams embedded with SMA wires,” *Compos. Sci. Technol.*, vol. 69, no. 13, pp. 2034–2041, Oct. 2009, doi: 10.1016/j.compscitech.2009.01.017.
[141] D. A. Hebda, M. E. Whitlock, J. B. Ditman, and S. R. White, “Manufacturing of Adaptive Graphite/Epoxy Structures with Embedded Nitinol Wires,” *J. Intell. Mater. Syst. Struct.*, vol. 6, no. 2, pp. 220–228, Mar. 1995, doi: 10.1177/1045389X9500600209.
[142] “Product Information M524-C64 Surfacing Tissue for GRP Laminates.” Owens Corning\.
[143] “TECHNICAL DATA SHEET FM 300-2 ADHESIVE FILM.” Solvay.
[144] “FIBASIL.” Vivian Regina.
[145] “TECHNICAL DATA SHEET FM 300 ADHESIVE FILM.” Solvay.
[146] “Newport 301 Product Data Sheet.” Mitsubishi Rayon Carbon Fiber and Composites, Inc, 2012.

A. Appendices

A-1 Table of Contents (Appendix)

A-2 List of Figures (Appendix)

A-3 List of Tables (Appendix)

A-4 SMAHC Panel Manufacturing Process

The panels are manufactured using an adaptation of a standard out-of-autoclave manufacturing process, following the general steps in Table A.1.

Table A.1 Manufacturing Steps Outline

Step	Diagram
1) Wires are threaded through the SMA Combs and prestrained by the desired amount by turning the lead screw.	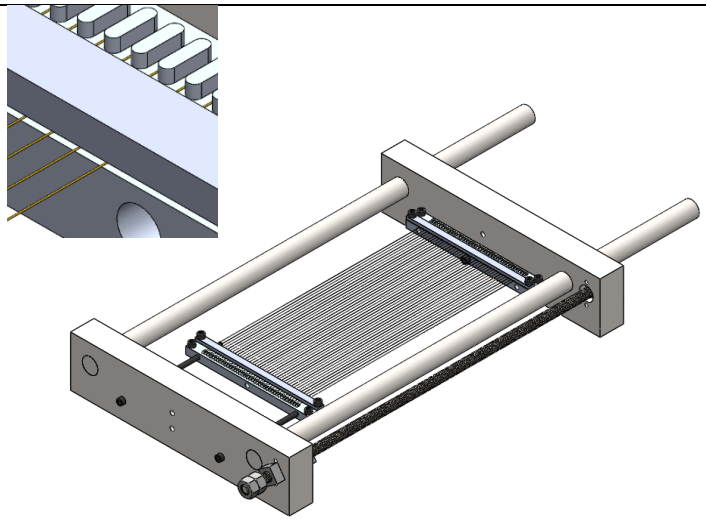
2) The laminate, including the FRP layers and glass veil, is laid up	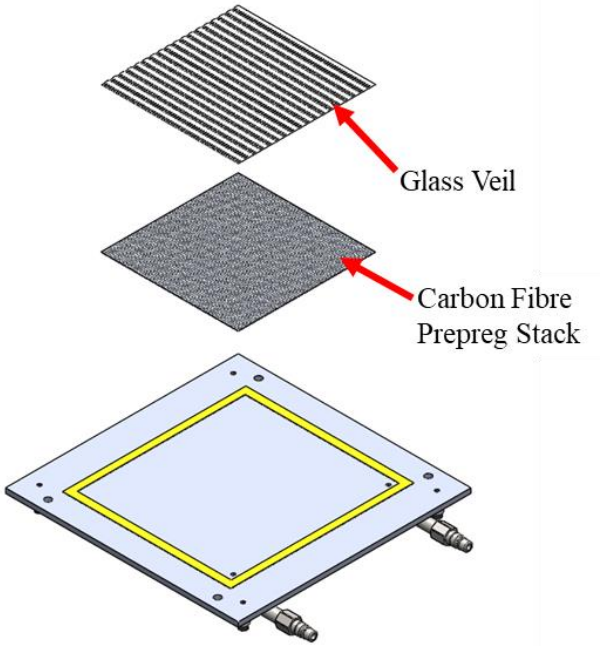

3) The SMA frame is placed over the tool plate

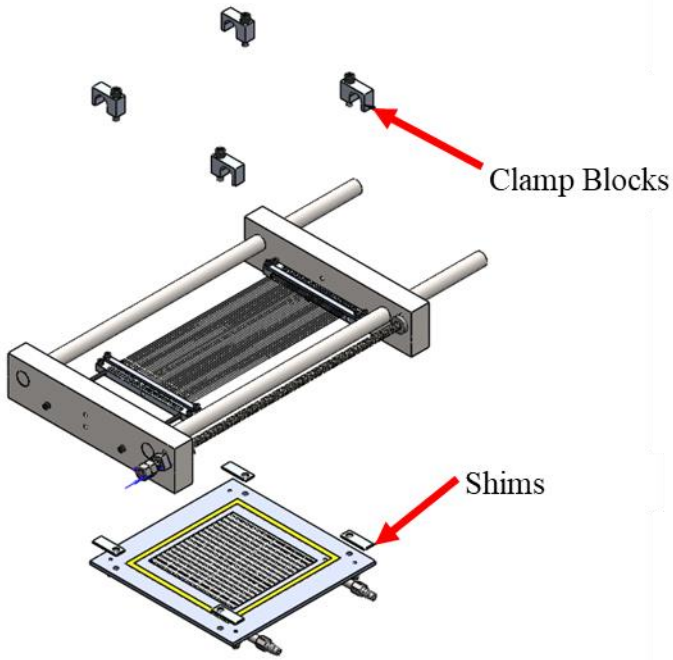

4) The adhesive layer is placed over the SMA wires and rolled on

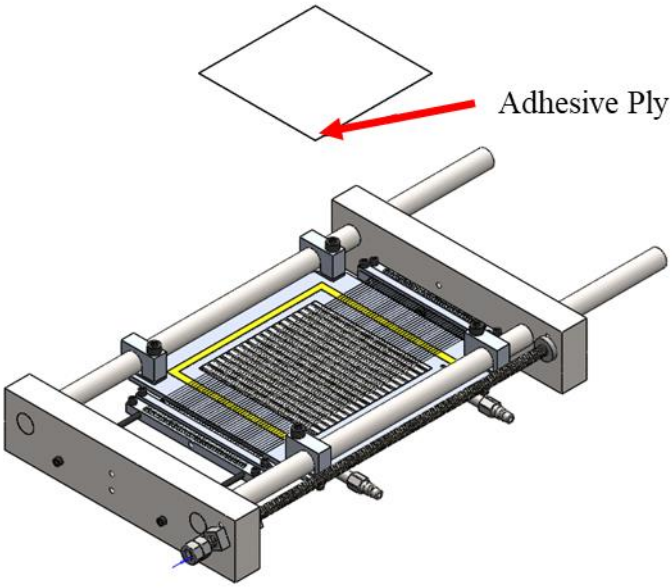

5) Heated blankets[9], peel ply, breather, and vacuum bag are installed according to the stack sequence and checked for leaks.

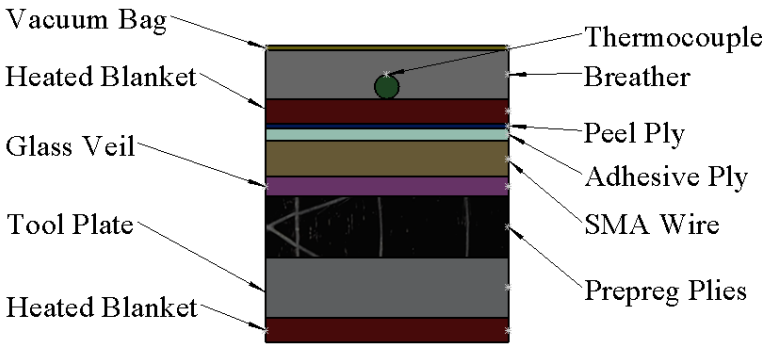

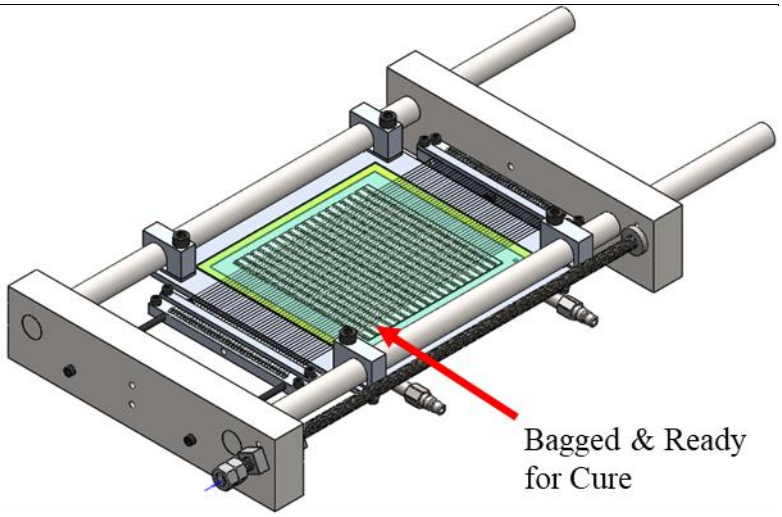

6) The laminate is processed according to the desired debulking and cure cycle.[10]

7) Laminate is cooled on the tool and the tool is cleaned after demolding

[9] Heated blankets are optionally used to allow faster and more uniform heating of the laminate to minimize thermal and cure gradients in the part.

[10] The cure cycle used for this laminate is the recommended one from Newport, in [146]

A-5 Code Flow Charts

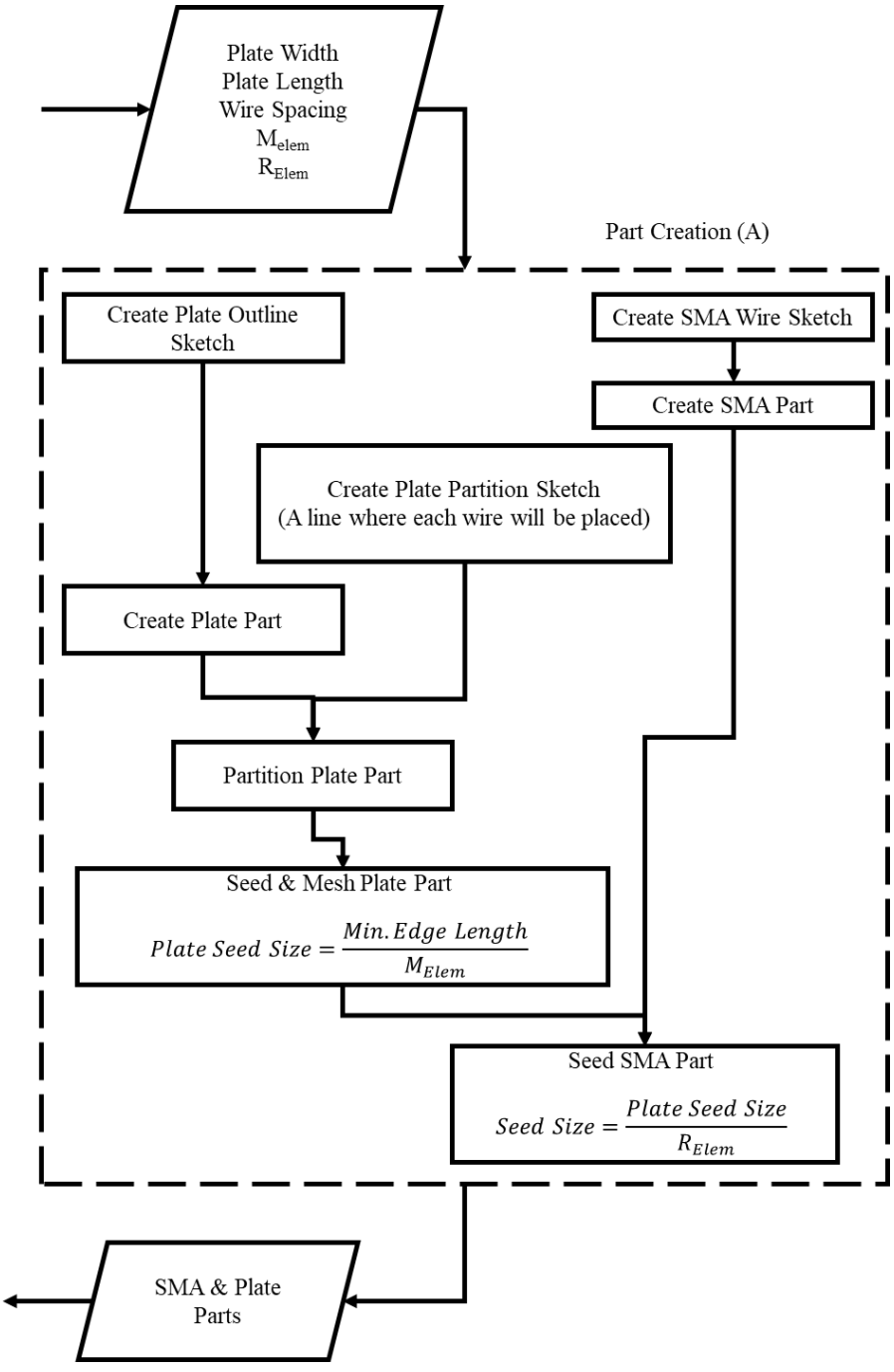

Figure A.2 Part Creation Sub-Flow Chart

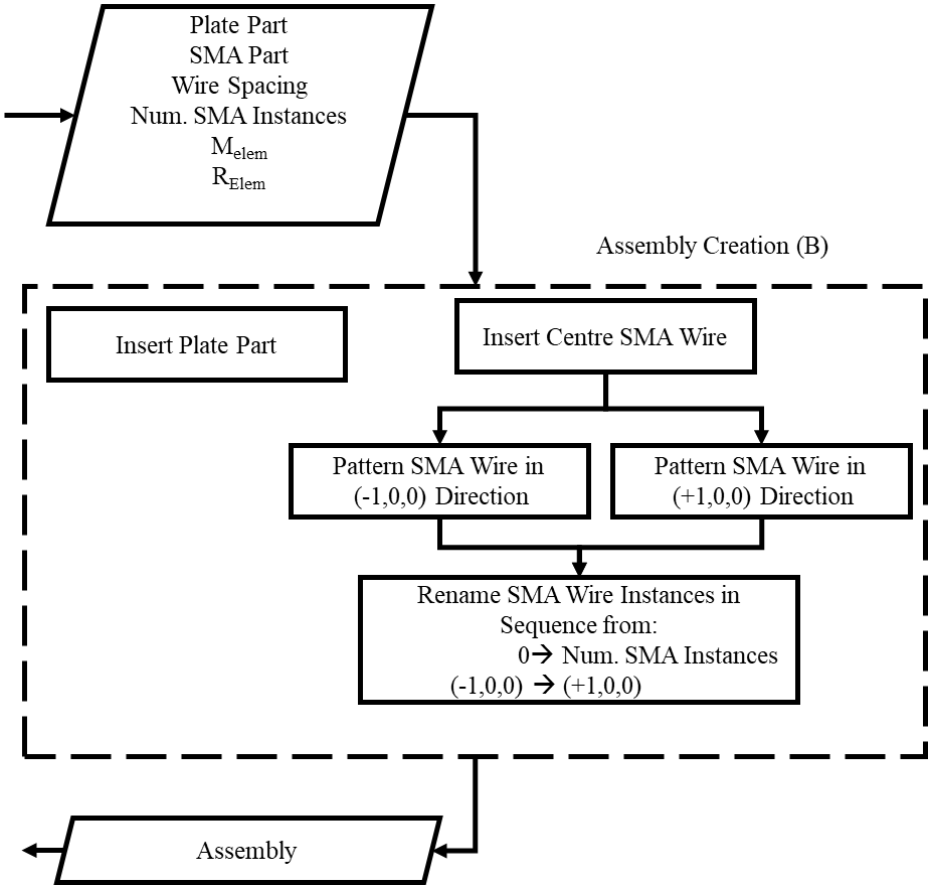

Figure A.3 Assembly Creation Sub-Flow Chart

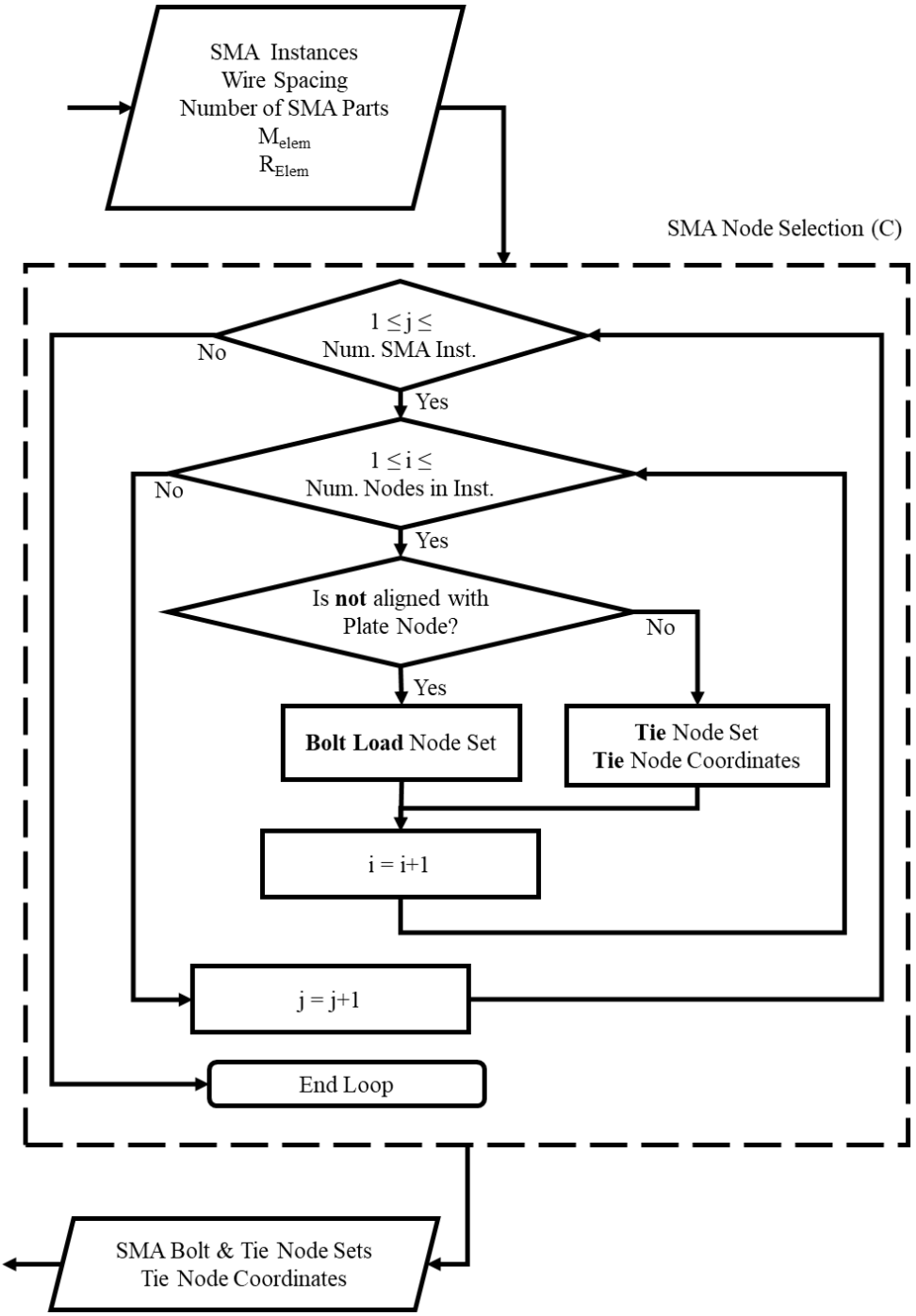

Figure A.4 SMA Node Selection Sub-Flow Chart

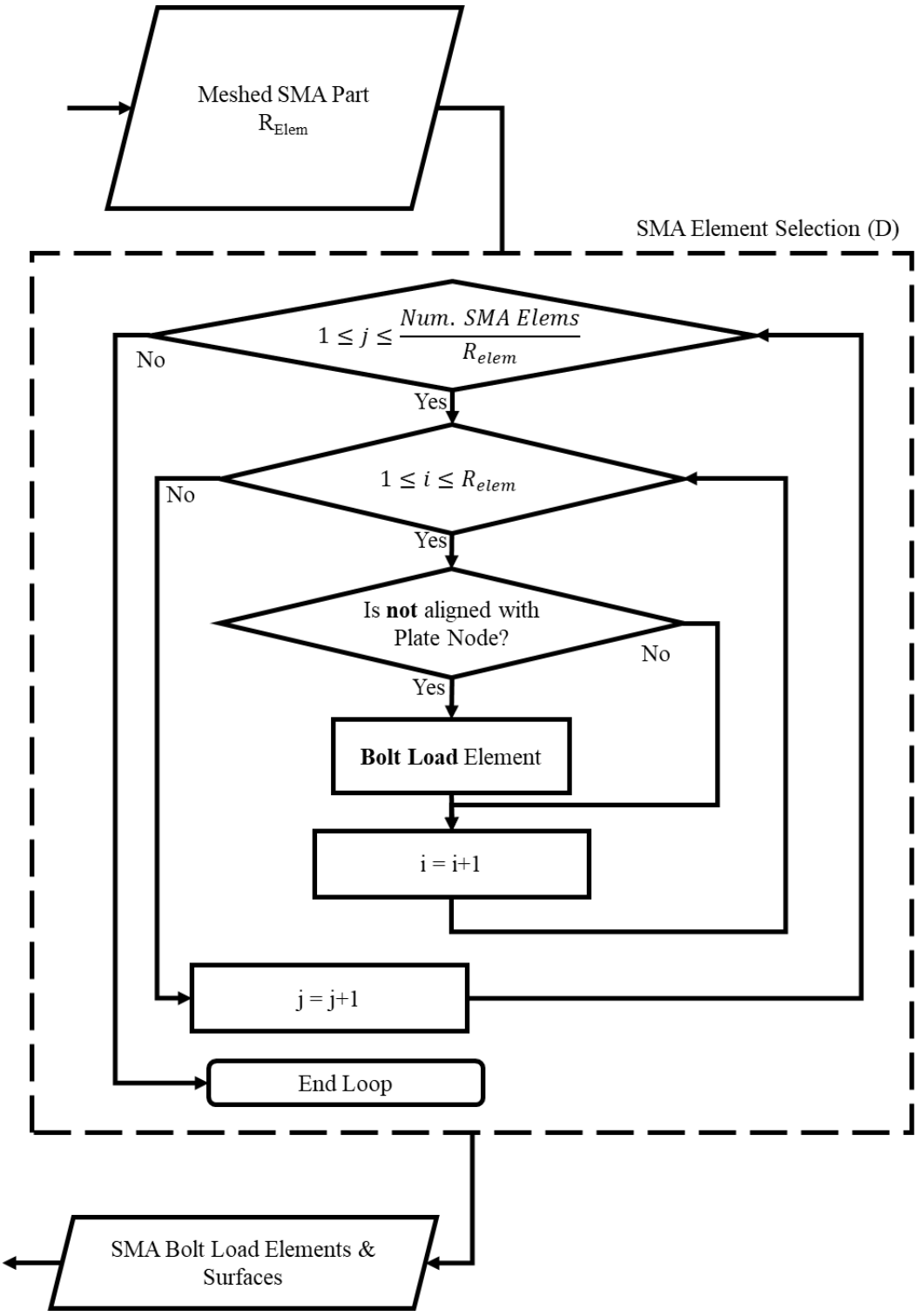

Figure A.5 SMA Element Selection Sub-Flow Chart

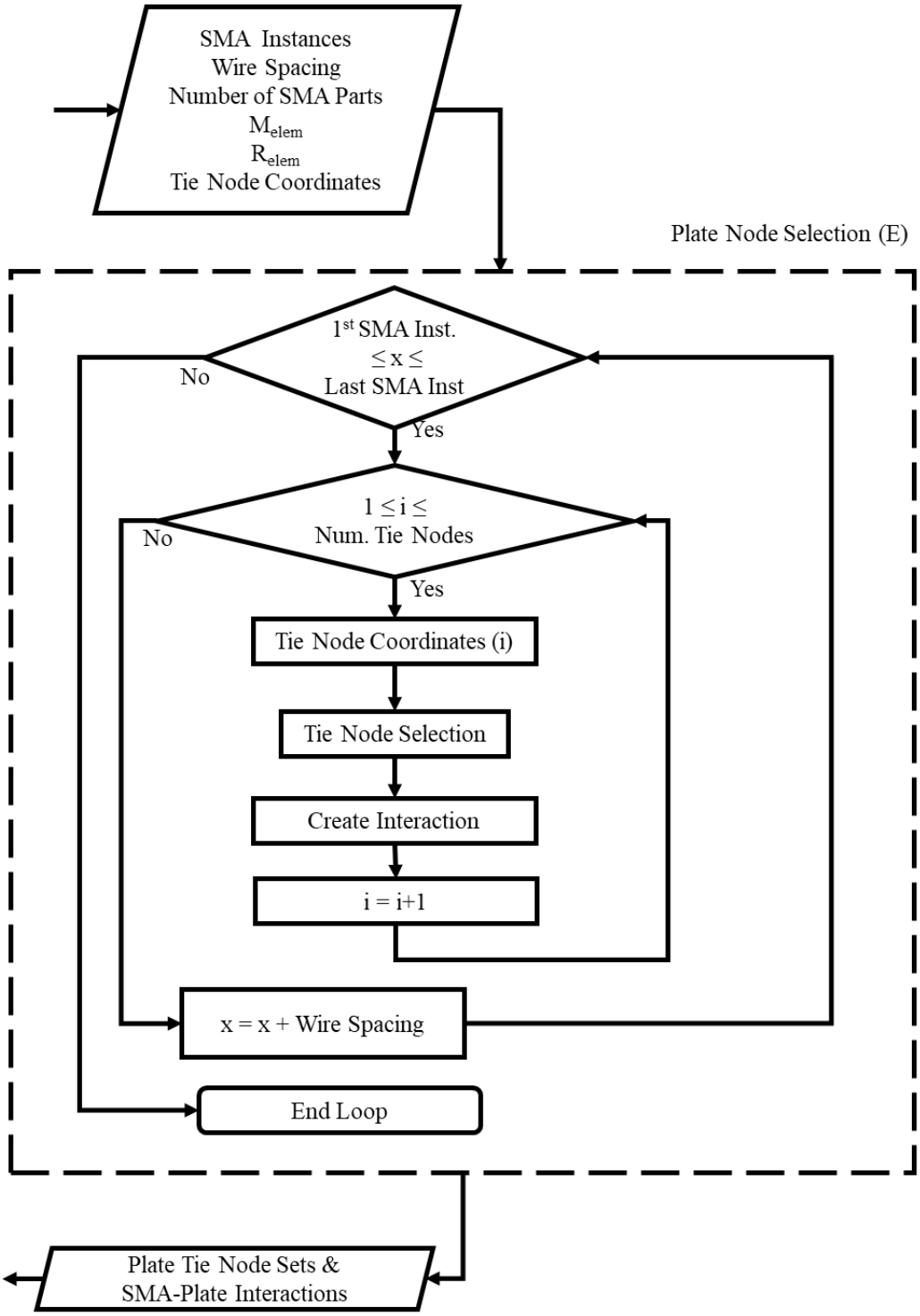

Figure A.6 Plate Node Selection Sub-Flow Chart

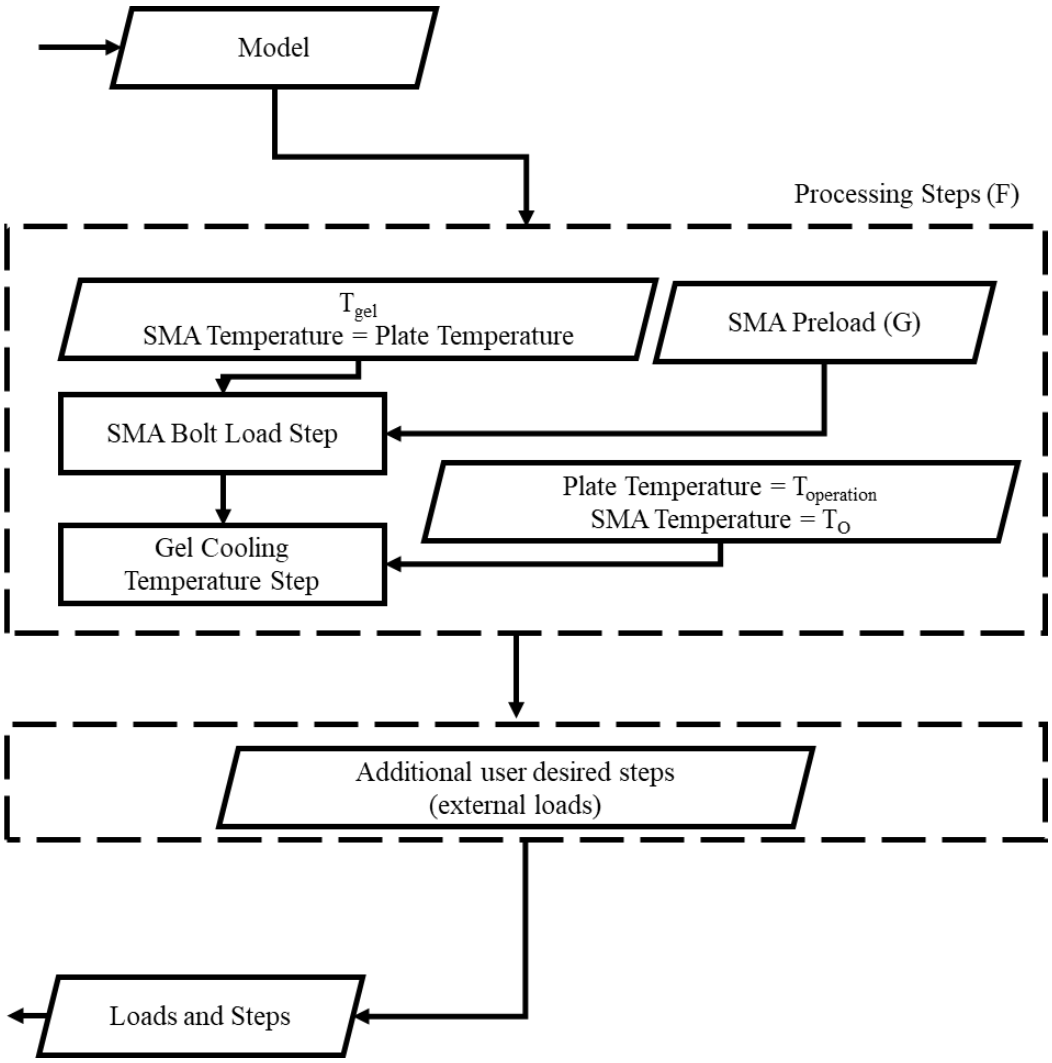

Figure A.7 Processing Steps Sub-Flow Chart

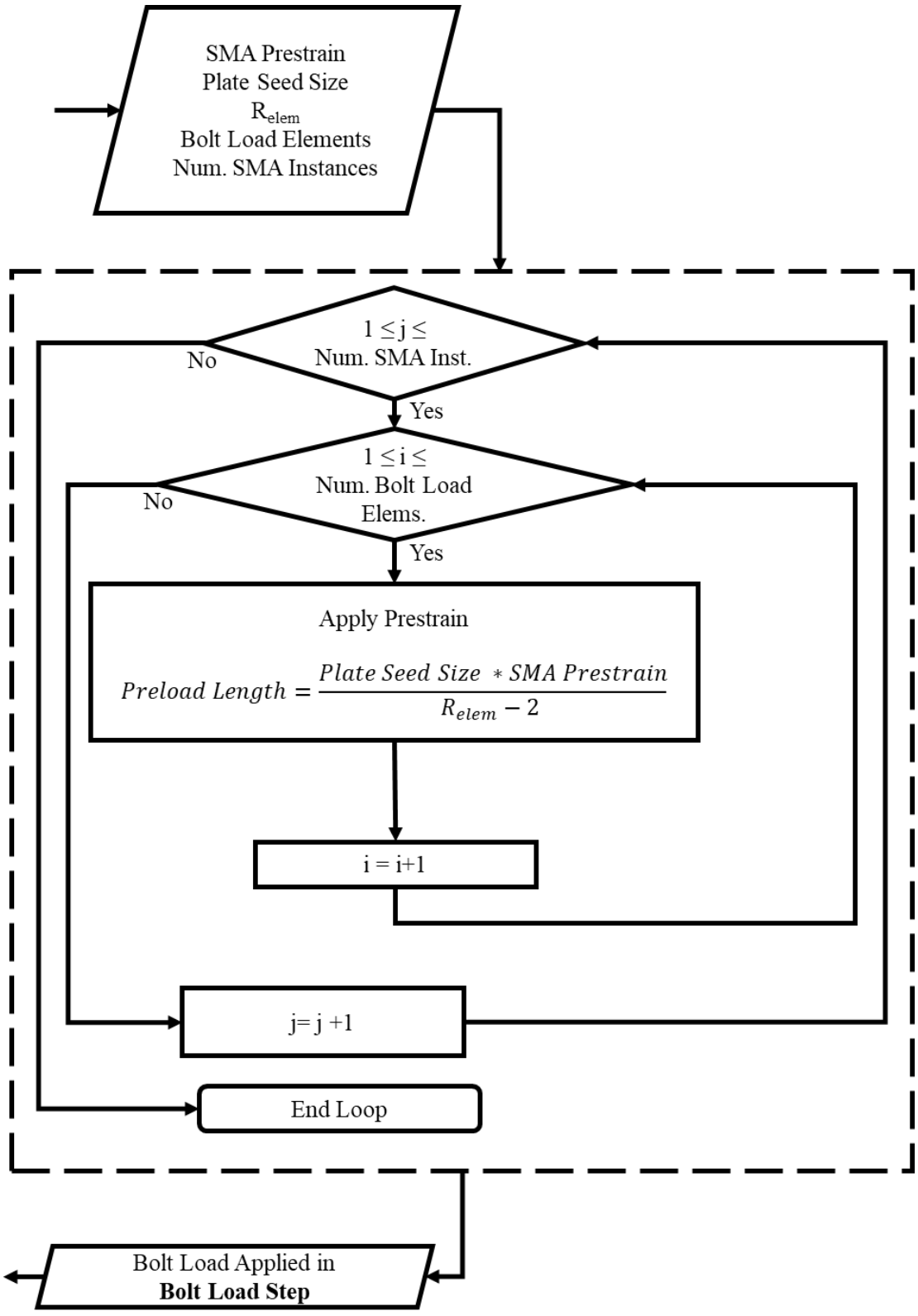

Figure A.8 SMA Prestrain Sub-Flow Chart